

DEFORMATION MECHANISMS IN HIGH PERFORMANCE TRANSPARENT
CERAMICS DUE TO INDENTATION AND IMPACT EVENTS

By

EDWARD J. HANEY

A DISSERTATION PRESENTED TO THE GRADUATE SCHOOL
OF THE UNIVERSITY OF FLORIDA IN PARTIAL FULFILLMENT
OF THE REQUIREMENTS FOR THE DEGREE OF
DOCTOR OF PHILOSOPHY

UNIVERSITY OF FLORIDA

2011

© 2011 Edward J. Haney

To my loving family. Without the support, encouragement and immeasurable sacrifice of my wife Jill, this endeavor could have never been completed. It is impossible to overstate the sacrifices my son Caleb and daughter Marissa have made due to my many hours away from them during the earliest years of their lives. Every time I reflect on this experience I will always remember the people closest to me who provided undying support. Thank you!

ACKNOWLEDGMENTS

I am indebted to many people who have contributed their support, knowledge and encouragement throughout the completion of this degree. First I would like to thank my wife, Jill, for her unwavering support. Her ability to listen, offer suggestions and provide a calming atmosphere was critical to success. I would also like to thank my children, Caleb and Marissa, for their understanding of my time demands and inability to be with them as much as I would have liked to during the last few years.

I would also like to thank my Aunt Joanne for providing support by picking me up and dropping me off at the airport in Tampa as well as providing transportation to and from school in Gainesville. This undoubtedly saved me thousands of dollars. I would also like to thank her keeping my laundry clean and providing me a place to stay.

I would like to thank my graduate committee; Dr. Ghatu Subhash, Dr. Nagaraj Arekere, Dr. Peter Ifju and Dr. John J Mecholsky Jr.. I would especially like to express my gratitude for the support that Dr. Subhash has always provided. I have known professor Subhash for 14 years going all the way back to my undergraduate work with him at Michigan Tech. University. I remember him urging me to complete my PhD directly after my undergrad but like so many graduates at that time I chose to pursue a career in industry instead. It was ten years after I first met him that I expressed my interest in completing this degree. There was never an unwavering moment in his belief in me. Throughout the 4 years of completing this degree in Florida while living in Michigan, he provided unwavering support and encouragement.

I would also like to acknowledge the support of fellow "Techies" and graduate students Mike Klecka and Tim Walter. I really feel that half of this degree is theirs for all of the guidance, knowledge and support they both provided me. They often helped me

set up and execute tests (especially the ball impact and high speed photography) relevant to my research with no value to them, often compromising their own work. They also helped me tremendously with knowledge of procedures and department protocol. I cannot thank them enough.

Lastly I would like to express my deep gratitude to Mr. Bindon and the entire management team at Trijicon Inc. Without the financial support to help me with tuition costs this would have been nearly impossible to complete. I would especially like to thank Paul Koesler for his help in formulating and presenting my tuition support proposal to management and also Don Houghton for supporting me as an employee and presenting the proposal to the board of directors. I cannot overstate what it means to me to be valued and have this level of support from people who have only known me for a couple years. I hope to have many years to come working with Trijicon, allowing me the opportunity to repay the offer of support.

TABLE OF CONTENTS

	<u>page</u>
ACKNOWLEDGMENTS.....	4
LIST OF TABLES.....	8
LIST OF FIGURES.....	9
LIST OF ABBREVIATIONS.....	12
ABSTRACT.....	13
CHAPTER	
1 INTRODUCTION AND MOTIVATION.....	17
Background.....	17
Motivation for Research.....	20
2 MATERIALS	24
Sapphire (Single Crystal Al_2O_3)	24
Magnesium Aluminate Spinel (MgAl_2O_4)	27
3 STATIC AND DYNAMIC INDENTATION RESPONSE.....	35
Introductory Remarks.....	35
Experimental Methods	37
Material Preparation	37
Dynamic Indentation Hardness Tester	38
Results.....	40
Static and Dynamic Hardness	40
Static and Dynamic Brittleness.....	43
Static and Dynamic Indentation Fracture	46
Closing Remarks	56
4 CRACK INTERACTION RESPONSE DUE TO SEQUENTIAL INDENTATIONS ...	71
Introductory Remarks.....	71
Experimental Methods	75
Results.....	76
Fracture Plane Geometry	76
Crack Interaction Sensitivity	79
Crack Interaction in Spinel.....	82
Closing Remarks	83

5	BALL IMPACT RESPONSE.....	91
	Introductory Remarks.....	91
	Experimental Methods	92
	Results.....	94
	Impact Damage Evolution	94
	Impact Energy Balance	102
	Closing Remarks	112
6	SUMMARY	125
	Research Conclusions.....	125
	Future Research Plans	129
	LIST OF REFERENCES	133
	BIOGRAPHICAL SKETCH.....	148

LIST OF TABLES

<u>Table</u>		<u>page</u>
2-1	List of mechanical and optical properties for sapphire and spinel.....	30
2-2	Critical shear stresses required for slip and twinning systems to activate (proposed by Tymiak and Gerberich [49])	30
3-1	Calculated brittleness parameters and material properties used for calculations.....	58
5-1	Material properties used for energy calculations	114
6-1	Various static and dynamic material Properties for a-plane sapphire and Mg- spinel	130
6-2	Comparison of static and dynamic hardness and brittleness for spinel and sapphire.....	130
6-3	Comparison of energy dissipation mechanisms for sapphire and spinel	131

LIST OF FIGURES

<u>Figure</u>	<u>page</u>
1-1 Schematic of Transparent Armor Design.....	22
1-2 Comparison of V_{50} effectiveness for various transparent armor materials (recreated from Swab et al. 2000 [36])	23
2-1 Sapphire unit cell depicting the orientation of different crystallographic axes.....	31
2-2 Crystal growth process schematics.	32
2-3 Depiction of slip and twinning systems in Sapphire	33
2-4 Graphical depiction of the relation of Schmid factor angles	33
2-5 Schematic of the spinel unit cell. For clarity the octahedral and tetrahedral interstices are shown only in the front half of the unit cell.....	34
2-6 Optical images of example spinel microstructures. Included are A) fine grained [79], B) bi-modal [79] and C) course grained structures	34
3-1 Schematic of the orientation of <i>a</i> -plane sapphire crystal tile supplied by Saint- Gobain crystals.....	58
3-2 Optical image of the grain structure of the spinel supplied by Technology Assessment & Transfer	59
3-3 Schematic of the dynamic indentation hardness testing apparatus.....	59
3-4 Static and dynamic hardness trends as a function of indentation load..	61
3-5 Graph of static and dynamic indentation hardness of spinel..	61
3-6 Graph of static and dynamic indentation hardness showing critical hardness....	63
3-7 Static and dynamic indentation fracture patterns.....	63
3-8 Schematic of sapphire crystal axes projected angles and the relevant preferential crack systems.....	64
3-9 Enlarged view of jagged appearance of B cracks during static indentation on <i>a</i> -plane sapphire.....	65
3-10 Enlarged view of dynamic indentation on <i>a</i> -plane sapphire showing increased spalling during dynamic indentation.	65

3-11	Half-crack length 'c' as a function of indentation load 'P' of a-plane and c-plane sapphire under static and dynamic indentations.....	66
3-12	Optical images of induced crack patterns due to static indentations on spinel... ..	67
3-13	Plot of half crack length 'c' versus load 'P' for static indentations revealing a relationship of the type $c \propto P^{2/3}$ for both inter and intragranular cracks	68
3-14	Optical images of induced indentation crack patterns after successive polishing steps revealing radial cracks	68
3-15	Optical images of induced crack patterns due to dynamic indentations on spinel.....	69
3-16	Plot of half crack length 'c' versus load 'P' for dynamic indentations revealing a relationship of the type $c \propto P^{2/3}$ for both crack types	70
3-17	Optical images of 3Kg A) static and B) dynamic indentations	70
4-1	Schematics depicting sapphire crack plane geometry.....	84
4-2	A) Optical image and B) schematic of cracks induced by the sequential indentations along the 0° orientation.	85
4-3	Optical images and schematic of the cracks induced by the sequential indentations along the 45° orientation.....	86
4-4	A) Optical images and B) schematic of the cracks induced by the sequential indentations along the 90° orientation.....	87
4-5	Optical image and schematic of cracks induced by the sequential indentations along the 135° orientation.....	88
4-6	Experimental data revealing damage sensitivity of a-plane sapphire due to sequential indentations at various orientations and radial separations.....	89
4-7	Optical image of cracks induced by the sequential indentations on spinel at various orientations.	90
5-1	Schematic of the Edge-On-Impact test setup.	114
5-2	Sequence of high speed photographs revealing damage evolution in spinel due to a steel ball impact at 280 m/s.	115
5-3	Images of recovered ball fragments from the spinel impact tests.....	116
5-4	Images of fracture within recovered spinel after impact test.....	117

5-5	A) High magnification image of the spinel bar upon impact showing ejecta and zone 1 dilation and B) schematic depicting various damage zones.....	118
5-6	A) Plot of damage front depth vs. time for spinel and B) schematics of assumed grain shape showing fracture paths.	119
5-7	Sequence of high speed photographs revealing damage evolution in sapphire due to a steel ball impact at 268 m/s.	120
5-8	Images of recovered ball fragments from the sapphire impact tests showing a fractured surface and a smoothly deformed contact surface	120
5-9	A) Magnified image of sapphire rod during impact showing <i>c</i> -axis oriented damage bands and B) a schematic of the criss-crossing B, R1 and R2 cracks	121
5-10	Photograph of recovered sapphire rod showing large fragments and triangular shaped zones of dilation and fragmentation.	121
5-11	Plot of damage front depth vs. time for sapphire.	122
5-12	Summary of the fractional amount of impact energy dissipated by various deformation and fracture mechanisms in spinel.	123
5-13	Summary of the fractional amount of impact energy dissipated by various deformation and fracture mechanisms in <i>m</i> -axis sapphire.	124
6-1	Comparison of half crack lengths for spinel and sapphire due to dynamic indentation.....	131
6-2	Examples of other uses for spinel and sapphire.....	132

LIST OF ABBREVIATIONS

ALON	Aluminum Oxynitride
CRSS	Critical Resolved Shear Stress
DIHT	Dynamic Indentation Hardness Tester
DOP	Depth of Penetration
EFG	Edge-Defined Film-Fed Growth
EOI	Edge On Impact
ERSS	Effective Resolved Shear Stress
FCC	Face Centered Cubic
FEA	Finite Element Analysis
GSM	Gradient Solidification Method
HEL	Hugoniot Elastic Limit
HEM	Heat Exchanger Method
HIP	Hot Isostatically Pressed
HP	Hot Pressed
IR	Infrared
ISE	Indentation Size Effect
RSS	Resolved Shear Stress
SENB	Single Edge Notched Beam
SHPB	Split Hopkinson Pressure Bar
TEM	Transmission Electron Microscopy
WOD	Work of Deformation
WOF	Work of Fracture
YAG	Yttrium-Aluminum Garnett

Abstract of Dissertation Presented to the Graduate School
of the University of Florida in Partial Fulfillment of the
Requirements for the Degree of Doctor of Philosophy

DEFORMATION MECHANISMS IN HIGH PERFORMANCE TRANSPARENT
CERAMICS DUE TO INDENTATION AND IMPACT EVENTS

By

Edward J. Haney

August 2011

Chair: Ghatu Subhash
Major: Mechanical Engineering

Static and dynamic indentation as well as edge-on-impact (EOI) testing of sapphire and magnesium spinel is presented in this work. The sapphire samples were provided by Saint Gobain Crystals, Milford, NH while the spinel materials were provided by Technology Assessment and Transfer, Annapolis, MD. The overall intent of the research effort was to develop a general understanding of the fundamental mechanics that dictate variances of ballistic performance between the two materials. Specifically, it is of interest to develop a rationale for the observation of superior ballistic performance of magnesium spinel compared to sapphire (especially multiple-hit resistance), while sapphire is superior to spinel when comparing nearly every measurable static and dynamic material property. Since a comparison of measureable material properties (e.g. hardness, fracture toughness, etc.) is obviously insufficient in complete characterization of a materials ballistic potential, it is proposed that a comprehensive analysis of the fundamental fracture behaviors of these materials during dynamic events such as dynamic indentation and ball impact tests is needed to provide better insight into the governing parameters of ballistic strength. The type of cracks as well as the

load and rate dependence of evolved fracture patterns is of interest. As such it is clear that different techniques to characterize the materials are needed. Dynamic indentation, sequential indentation and ball impact tests are small scale tests suited to provide this type of material characterization.

A dynamic indentation test apparatus was utilized in order to observe the strain rate sensitivity to hardness, indentation fracture response and brittleness. Utilizing this technique it was found that sapphire resulted in a 10-12% increase in hardness during dynamic indentation while spinel hardness only increased 5%. Additionally, it was found that spinel indentation cracks did not exhibit the same length reductions as that of sapphire during dynamic indentations. Spinel did however demonstrate less brittleness under dynamic conditions than sapphire resulting in less spall. Additionally a change in fracture mode from intergranular to transgranular was noted during dynamic indentation conditions. The results of this testing confirms that simply comparing measurable properties, even if dynamic (e.g. dynamic hardness) is insufficient in the prediction of ballistic performance. The increase in brittleness seen in sapphire as compared to spinel, however, is of relevance in the prediction of the propensity for spall fracture. This combined with the fact that spinel radial cracking does not reduce under dynamic loads presents the notion that energy is dissipated in spinel over a larger area than that of sapphire. This is important as spreading the energy over a larger area will reduce the amount of material pulverization and loss of structural cohesion.

A technique of analyzing the crack response of patterns of closely spaced static indentations was developed. The aim was to highlight the interactivity of cracks due to multiple indentations which is germane to multi-hit capability predictions as well as

failure prediction. The results of this test indicated a high sensitivity of crack interactivity to crystallographic plane orientation. Additionally, a material failure mechanism only present along the *c*-axis highlights a mode of failure relevant to multiple impact events on sapphire. This failure mechanism facilitated bulk material separation in sapphire along the *c*-axis. Spinel, however did not exhibit any of these behaviors, reinforcing the idea that spinel better retains structural cohesion when damaged. This again offers some explanation to the improved behavior during multiple hit pattern testing.

Edge-On-Impact tests utilizing a high speed camera were conducted in order to observe damage morphology in the two materials during ball impact events. Spinel and sapphire damage evolution were in stark contrast with each other. It was found that spinel fractures were initially transgranular but transitioned to purely intergranular as the damage front moved away from the impact site. This transition also marked the demarcation line where structural cohesion was maintained. Sapphire however was found to fracture along specified crystal planes resulting in a criss cross pattern of fracture planes. This criss cross pattern resulted in the creation of large fragments and a lack of structural cohesion for larger portion of the target than that of spinel. Finally based on the observed behaviors, the impact energy that is dissipated through all known mechanisms was accounted for using known energy calculation equations. It was found that energy dissipation was spread more evenly among mechanisms resulting in a higher capacity to dissipate energy.

An overall research hypothesis is presented as follows: It is proposed that the comparison of measureable material properties, even dynamic properties, is insufficient in complete prediction of a materials ballistic performance. The ability to dissipate

energy over large areas exploiting several dissipation mechanisms is paramount for improving ballistic protection. Additionally, the propensity for a material to remain structurally cohesive during and after damage accumulation is vital for ballistic performance (especially multi-hit capability).

Other scientifically significant highlights of the presented research are as follows; This research details the first report of dynamic hardness for sapphire and magnesium-spinel. Additionally, this is the most comprehensive to date explanation of sapphire crack plane geometry as related to crystal geometry. This research also presents the discovery of a new material separation mode that exists in sapphire due to sequential closely spaced indentations. Damage evolution comparisons between the two materials have lead to the understanding of a more efficient mode of damage in spinel allowing the continuance of structural cohesion for a larger portion of the material. Finally, a summarization of energy dissipation mechanisms for both materials describes a more evenly distributed dissipation of impact energy between available mechanisms.

CHAPTER 1 INTRODUCTION AND MOTIVATION

Background

The investigation of ceramics (e.g. Aluminum Oxide- Al_2O_3) as light weight alternatives to conventional heavy armor began with Wilkin's pioneering efforts in the 1960s [1-7]. Since Wilkin's work, many efforts have been made to link ceramics material performance during impact events to typical material properties such as hardness, fracture toughness and strength [7-17].

Most research on the governing mechanics determining ballistic resistance has centered on static material properties such as hardness and fracture toughness. Woodward [8] was one of the first to note importance of hardness in the blunting of a projectile yet realized the limiting effect that fracture has. Den Reijer [14] reinforced this observation and added that increased hardness above that of the projectile did little to improve ballistic strength. LaSalvia [15] later proposed the notion that hardness can estimate the performance potential of a ceramic while fracture toughness is a limiting measure that determines the ability to meet that potential.

Concurrently, a realization of the need to understand material behavior due to high strain rate events surfaced. One common dynamic measure is the Hugoniot Elastic Limit or HEL. The HEL is effectively interpreted as the limit of elasticity and the onset of failure under uniaxial dynamic loading. The HEL is important to understand since it has been shown that dramatic shear strength reductions are shown to occur in materials shocked above its HEL [10, 11]. It is therefore accepted that a higher HEL could result in a higher shock threshold before severe damage ensues during impact events. The wave velocities are also important to understand since they control the rate of damage

evolution during a dynamic event and the rate at which energy is removed from an impact site. Two wave velocities are often reported for materials. The first and fastest wave is the longitudinal compressive wave and the second trailing wave is the shear wave. The pressure required to cause damage in the presence of the first wave is typically referred to as the HEL however Grady [12] recognized that often damage occurred at pressures lower than HEL following the trailing shear wave. This outlines the importance of the shear wave in damage creation during shock events.

Klopp and Shockey [17] summarized the importance of understanding dynamic material properties such as dynamic hardness. More recently Krell and Straßburger [16] presented a hierarchy of key influences governing ballistic strength of transparent ceramics. They postulated that the initial phase during ballistic impact, termed dwell phase [18, 19] was governed by dynamic stiffness and that the latter phase or penetration phase [7] is governed by the inertial impedance which is based on the mode of fragmentation and hardness. Moreover, in this study it was suggested that static hardness should be replaced by a dynamic measure like Hugoniot Elastic Limit (HEL).

Parallel to the efforts on the understanding of ceramics during ballistic impact, other researchers focused on developing knowledge of erosion mechanics and the controlling material properties. Evans and Wilshaw [20] developed relations for the effect of various material properties on the erosion resistance of ceramics by solid particles and found that the same material properties thought to govern ballistic performance also determined erosion resistance. Later work by various researchers have expounded upon this early work contributing knowledge in the area of liquid particle and combined liquid/solid particle erosion mechanisms [21-26].

A series of opaque ceramic materials such as aluminum nitride (AlN), boron carbide (B_4C), silicon carbide (SiC), silicon nitride (Si_3N_4) and titanium diboride (TiB_2) have emerged as potential light weight ceramic replacements for heavy armor. Although these materials are promising alternatives to heavy steel plates for ballistic protection, they are limited to applications where visibility and light transmission is not a requirement. The importance of pursuing materials able to replace traditional transparent armor has therefore become evident [27].

The investigation of transparent ceramics to replace traditional transparent armor has therefore emerged as an important subset of ceramic armor research. Traditional transparent armor (commonly referred to as bulletproof glass) usually consists of several layers of glass (usually soda-lime plate glass) and transparent polymers (typically polycarbonate). The glass layers dissipate energy through crack formation and particle ejection mechanisms; the adhesive/polymer interlayers act as bonding layers and accommodates for thermal expansion effects and the polymer backing acts as a spall shield. A schematic of a generic transparent laminate system is shown in Figure 1-1. The problems presented with this solution include poor optical performance, excessive weight and design packaging challenges due to the extreme thickness required to provide adequate ballistic protection. In addition excessive damage and loss of transparency due to rock strikes and sand/rain erosion has become a significant concern [27, 28].

Materials including aluminum oxynitride (ALON), sapphire, magnesium spinel, Yttrium-Aluminum Garnet (YAG), strengthened glass, and lithium disilicate/lithium aluminosilicate glass ceramics have been investigated for applications including

ruggedized optical lenses, visors, ground and air vehicle windows, missile domes and IR windows [27, 29]. In addition civilian applications, such as security building windows and other structural applications as well as security vehicle windows could also employ these technologies [30].

Many of the same challenges involved with traditional ceramic armors exist with the added challenges of providing adequate optical transmission. Transmission throughout the visible and Infrared (IR) wavelengths as well as improved performance during events such as high-velocity impact (e.g. ballistic impact), low to mid velocity impact (e.g. rock or bird strikes), scratch and particle impact erosion (e.g. sand blast, rain erosion) are all requirements for new high performance transparent ceramics [30-33].

Motivation for Research

Although many efforts have been made to advance the understanding of transparent ceramic materials, more work is needed. In particular, qualitative and quantitative assessments of transparent ceramic behaviors exposed to high strain rate events is paramount. Development and utilization of novel techniques to qualitatively and quantitatively capture the change in materials behaviors during small scale dynamic events is therefore a point of research interest.

Sapphire and Mg-spinel are two materials that are actively researched for use in transparent armor applications. Although sapphire is superior to spinel when comparing nearly all measureable static and dynamic material properties, spinel consistently outperforms sapphire in ballistic testing and in particular multiple impact testing [34-36]. Figure 1-2 is a recreation of the results of V_{50} testing conducted by the Army Research Lab comparing the ballistic performance of glass and various transparent ceramics

including sapphire and magnesium spinel [36]. The intent of this research is to develop an understanding as to the source of the superior ballistic performance known to exist in Mg-spinel. Rate sensitivity to hardness, brittleness and indentation fracture is studied using dynamic indentation methods. Qualitative and quantitative assessments of the static and dynamic mechanical response are discussed based on the experimental results. In addition, a novel indentation technique is developed in order to assess the interactive behavior between the resultant cracks from closely spaced indentation in an attempt to assess multi-hit capacity. Ball impact testing is conducted as well to provide a look into the actual material response characteristic of an impact event. The intent is to unlock the damage mechanics that occur during small scale impact events. Finally, an energy balance model based on observations during impact tests is presented for each material describing the contribution of each known mechanisms to the defeat of a projectile. This model attempts to explain observed behavior where comparison of static parameters is insufficient.

The rest of the dissertation is organized as follows. A summary of the two materials that are the subject of this research is presented in Chapter 2. In Chapter 3, the mechanical response of each material due to static and dynamic indentation tests is discussed. Separate discussions of hardness, brittleness and fracture behavior are presented. Chapter 4 summarizes the observations of crack interactivity in sapphire due to closely spaced indentations. A quantitative and qualitative account of damage morphology during edge-on-impact (EOI) tests is discussed in Chapter 5. This includes an energy based model attempting to apportion the dissipated energy between all

considered mechanisms. Finally in Chapter 6, conclusions and future research directions are outlined.

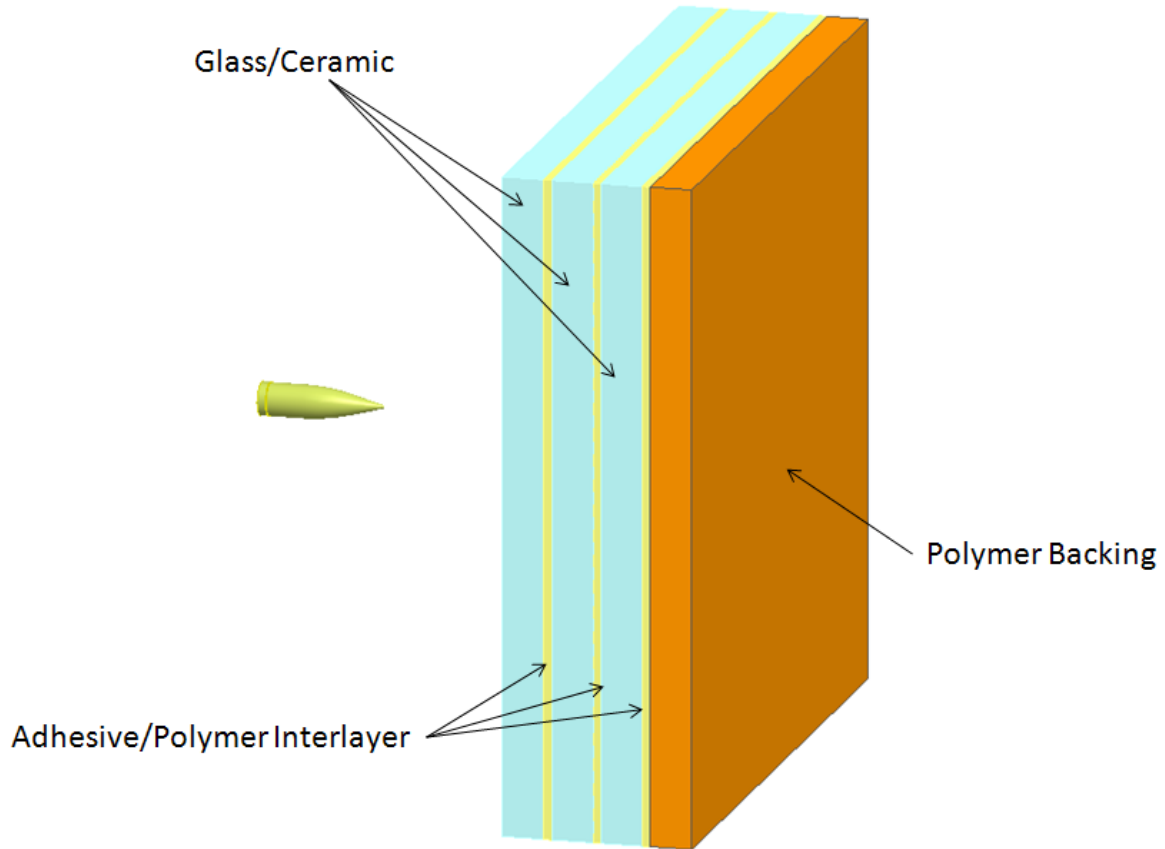


Figure 1-1. Schematic of Transparent Armor Design

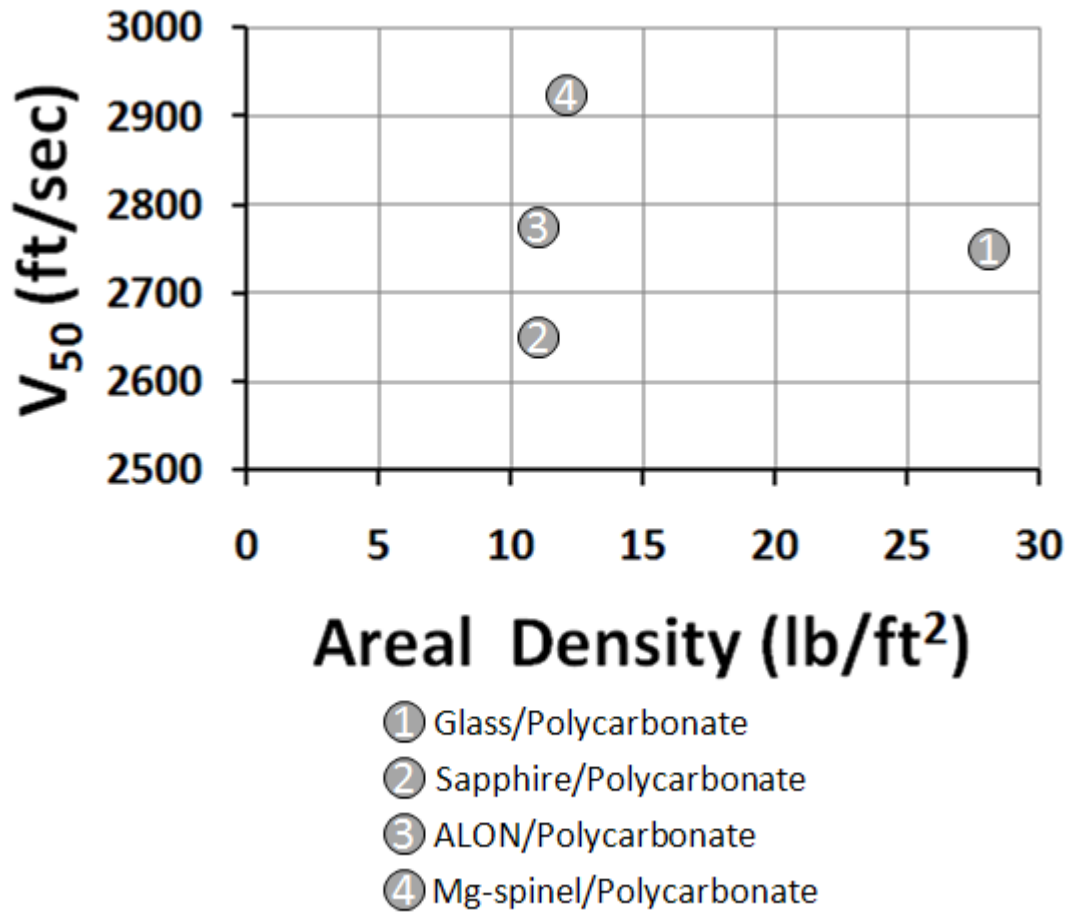


Figure 1-2. Comparison of V₅₀ effectiveness for various transparent armor materials (recreated from Swab et al. 2000 [36])

CHAPTER 2 MATERIALS

Sapphire (Single Crystal Al_2O_3)

Sapphire is a single crystal form of pure aluminum oxide (Al_2O_3). Other common names for sapphire include corundum, single crystal alumina and alpha alumina. Although the unit cell of sapphire is sometimes referred to and modeled as purely hexagonal or rhombohedral, the actual crystallographic classification of sapphire is a member of the Hexagonal-scalenohedral class of the Trigonal crystal system with a rhombohedral lattice system. Figure 2-1 depicts the sapphire crystal unit cell. Sapphire is most commonly manufactured in *c*- (0001), *m*- (1010), *a*- (1120) and *r*- (1102) plane configurations. Common industrial techniques used to grow sapphire crystals include Vernouil, Czochralski, Horizontal Directional Solidification Method (HDSM), heat exchanger method (HEM) and edge defined film fed growth (EFG) shown schematically in Figures 2-2A – E respectively. Each method is able to produce crystals of different orientations, sizes and qualities. A comprehensive review of the history of sapphire crystal growth and a comparison of methods is presented by Harris [37].

Sapphire has very good mechanical and optical qualities making it an ideal candidate for many extreme environment optical applications including protective shields, ground and air vehicle windows, optical lenses exposed to harsh environments and transparent armor [30, 38, 39] due to its excellent mechanical properties, optical transparency, IR transmission and commercial availability. Sapphire, however, has a hexagonal–scaleno-hedral crystal structure resulting in anisotropic material behavior that is highly dependent on crystal orientation. Mechanical, thermal, electrical and optical properties are widely reported to vary depending on axis orientation. For example,

hardness, Young's modulus, shear modulus and thermal conductivity are highest perpendicular to the *c*-axis while tensile strength, flexural strength and dielectric constant are highest parallel to the *c*-axis [40, 41]. In addition, optical birefringence or double refraction occurs along all axes except for the *c*-axis [41]. Therefore, the *c*-axis is optically unique and is often referred to as the optical axis [41, 42]. Table 2-1 provides relevant mechanical and optical properties for sapphire [41].

Sapphire deformation primarily occurs through a combination of slip (e.g. basal, prismatic, pyramidal) and twinning (Basal, rhombohedral) mechanisms [43]. Each deformation mechanism has several equivalent slip and twinning systems. Figure 2-3 depicts each deformation mechanism in a hexagon representation of sapphire [43]. The stress required to activate each system varies. Under compressive or tensile stresses a resolved shear stress values for each deformation plane can be calculated using Schmid factors [44]. Schmid factor (*m*) is defined as the cosine of the angle between the normal axis to the slip or twinning plane and the loading axis (θ) multiplied by the cosine of the angle between the slip or twinning direction and the loading axis (λ).

$$m = \cos \theta \cos \lambda \quad (1)$$

The calculated resolved shear stress is then if found by the following equation.

$$RSS = \frac{P}{A} m \quad (2)$$

where *P* is the load and *A* is the loading area, illustrated in Figure 2-4.

Nowak and coworkers [45-48] were the first to develop a critical resolved shear stress model for the indentation of sapphire aimed at predicting the shear stress needed to activate slip and twinning systems in sapphire. Tymiak and Gerberich [49] later offered improvements to the model by factoring in twinning shear, slip and twinning

multiplicity and a transition from elastic to elastic-plastic. Table 2-2 provides the critical resolved shear stress (CRSS) values for each deformation mechanism proposed by Tymiak and Gerberich [49].

Under increasing indentation loads sapphire demonstrates defined discontinuities in the load displacement curves. At these points the material suddenly shifts from an elastic to elastic-plastic behavior. These yield point discontinuities are commonly referred to as “pop-in” [50, 51], “step-in” [46, 47], “excursion” [52, 53] or “burst” [54, 55]. The exact nature of the discontinuities is uncertain although theories tie their existence to either the first nucleation of dislocations or instability due to already nucleated dislocations [56]. The severity and point of occurrence during indentation varies depending on crystal orientation, indenter geometry and loading rate.

It is also interesting to note that a significant loss in compressive strength occurs at elevated temperatures, most notably when the compressive stress is parallel to the *c*-axis [44]. This is found to be a result of a reduced resolved shear stress required to activate rhombohedral twinning mechanisms [57, 58]. Above 500°C rapid strength reductions perpendicular to the *c* axis begin leading to about a 98% loss in strength at 800°C. Several methods have been investigated to improve high temperature strength of sapphire including compressive coatings [59], Mg and Ti doping [60,61,62], B, Si, N, Fe, Cr ion implantation[63], heat treatments [60,64], neutron irradiation [65,66] and superpolishing techniques [60, 67]. These techniques have shown improvements in fracture toughness and compressive strength by stunting twinning motion with only slight to moderate degradations in optical properties [68].

When considering sapphire in many applications the dynamic material properties must be understood. Many studies have employed planar impact experimental techniques to determine the Hugoniot elastic limit (HEL), spall strength and the compression and shear wave velocities of sapphire [11, 69-73]. The HEL is important to understand since it has been shown that dramatic shear strength reductions occur in sapphire when shocked above the HEL [70]. The sonic velocities are important in order to understand the rate of damage evolution during a dynamic event and the rate at which energy is removed from an impact site. Rate variant indentation methods have also been employed to understand both the strain rate sensitivity of hardness and plasticity [48, 56].

Magnesium Aluminate Spinel (MgAl_2O_4)

Magnesium Aluminate Spinel (MgAl_2O_4) is a transparent polycrystalline ceramic sometimes simply referred to simply by its mineral name 'spinel'. Spinel is formed by sintering a mixture of magnesium oxide (MgO) and aluminum oxide (Al_2O_3) powders. The crystal structure of spinel is based on a face centered cubic (FCC) close-packed oxide anion sub-lattice in which Mg^{2+} cations occupy 8 of the 64 tetrahedral interstices and Al^{3+} cations occupy 16 of the 32 octahedral interstices [74]. Figure 2-5 provides a schematic of the spinel unit cell. For clarity, the octahedral and tetrahedral interstices are graphically depicted in only the front half of the unit cell.

Spinel is typically formed by sintering or hot press methods often utilizing Lithium Fluoride (LiF) as a sintering aid. A secondary hot isostatic press (HIP) process is often utilized to improve densification and optical quality. Spinel materials displaying both bimodal and unimodal grain structures with average grain sizes ranging from under $5\mu\text{m}$

to over 300 μ m have been reported [75 - 79]. Figure 2-6 depicts the varied grain structures known to exist with spinel [79].

The study of spinel has been sporadic since the 1950s with the first transparent spinel being created by General Electric in 1961 [80, 81]. Most failures in commercial production of spinel have been a result of a lack of understanding of the densification dynamics. Without an adequate densification approach, spinel tends to be translucent due to high amount of light scatter at pores and voids within the material. Through the use of LiF sintering aids and hot isostatic pressing (HIP) operations the porosity levels of spinel have been significantly reduced leading to optical and mechanical material properties that approach and even surpass single crystal sapphire [34, 35, 81]. A detailed history of optical spinel development is given by Harris [80].

Static mechanical properties (i.e. hardness, elastic modulus, fracture toughness and bending strength) [82-87] and optical properties (transmissivity, reflectivity, absorptivity and index of refraction) [86-89] have been well investigated since the 1960's. Table 2-2 provides relevant mechanical and optical properties of spinel. Additionally, plasticity [90, 91] and fracture character [36, 78, 92-102] of spinel have been intensely studied. Crystallographic studies have revealed that three slip systems along the (111), (110) and (100) slip planes exist within spinel. Of these planes, slip along the (111) and (110) planes are most commonly observed with slip directions parallel to the $\langle 110 \rangle$ direction [91]. Fracture character of polycrystalline spinel is generally described as mixed mode with the presence of intergranular and transgranular cracks [93]. Although transgranular cracks exist, strength limitations of polycrystalline spinel are largely attributed to the presence of intergranular fracture of large grains [36,

78]. The fracture response for spinel is also highly non-linear with rising R-curves (a measure of the materials resistance to crack propagation with crack extension) [95]. This behavior has generally been attributed to grain bridging effects at lower temps and secondary grain boundary microcracking in the crack wake [94]. Strength and fracture toughness is also known to reduce with increasing temperature up to 800°C with a stabilization occurring at further elevated temperatures [94-96]. It has been proposed that the melting point of the LiF sintering aid could lead to this behavior [95]. Increased strength spinel has been achieved by refining the sintering powders to produce a unimodal grain size distribution of less than 5 μm [76].

The strain rate sensitivity of spinel has been studied to some extent. Bending and flexural testing using variable loading rates have been conducted with varied results [97, 99, 102]. Additionally, planar impact experiments on polycrystalline spinel have been performed in an effort to determine the Hugoniot elastic limit (HEL), dynamic yield strength and spall strengths [103-105]. Perhaps the most interesting result from this type of testing on spinel has been the indication of a loss of spall strength to nearly zero at elevated loading rates [103].

Table 2-1. List of mechanical and optical properties for sapphire and spinel

	// to C-Axis	⊥ to C-Axis	Mg-Spinel
Density (g/cm ³)	3.97	3.97	3.58
Young's Modulus (GPa)	435	386	277
Shear Modulus (GPa)	175	145	110
Poisson's Ratio	.25-.30 (orientation dependant)		.26
Biaxial Flexural Strength (MPa)	1035	760	172
Compressive Strength (GPa)	1.97	2	2.69
Tensile Strength (GPa)	0.432	0.302	0.11
Vickers Hardness – 1Kgf (GPa)	17.4	15.6	14
KIC (MPa-m ^{1/2})	2.1	2.43	2.0
Hugoniot Elastic Limit (GPa)		23	11.3
Longitudinal Wave Speed (m/s)		11390	9820
Shear Wave Speed (m/s)		6900	5620
Visible Transmittance (%)		85	85
NIR Transmittance (%)		86.5	86
SWIR Transmittance (%)		88	86
Birefringence	0	0.008	0
Abbe Number		72.24	60.67

Table 2-2. Critical shear stresses required for slip and twinning systems to activate (proposed by Tymiak and Gerberich [49])

	Prism Slip	Basal Slip	Pyramidal Slip	Basal Twinning	Rhombohedral Twinning
τ^{CR} (GPa)	$2.5 < \tau^{CR} < 4.1$	$4.8 < \tau^{CR} < 23.7$	$\tau^{CR} \approx 7$	$0.48 < \tau^{CR} < 3$	$1 < \tau^{CR} << 7.3$

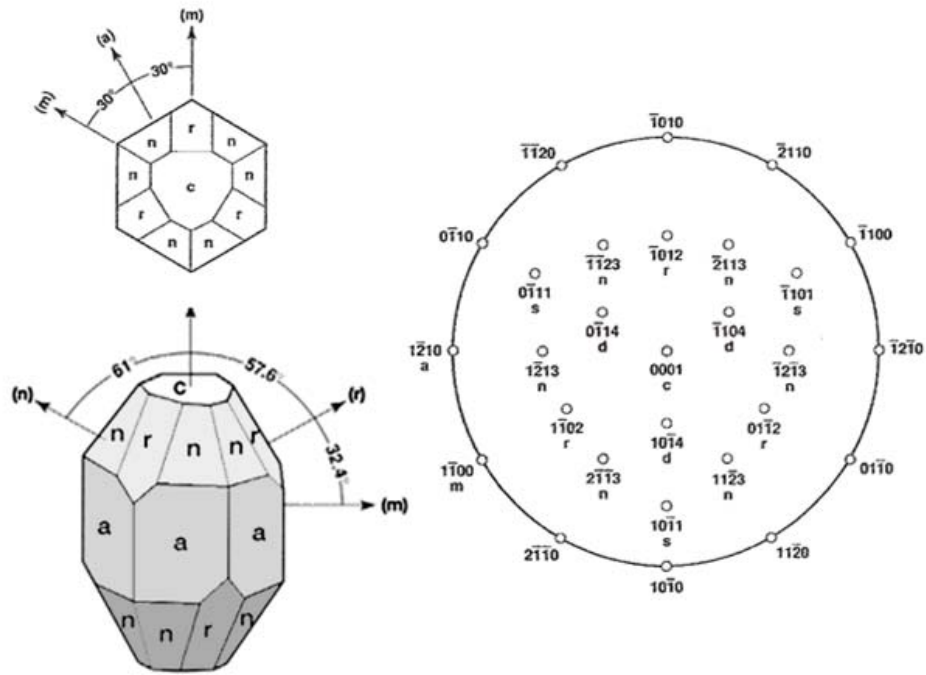


Figure 2-1. Sapphire unit cell depicting the orientation of different crystallographic axes

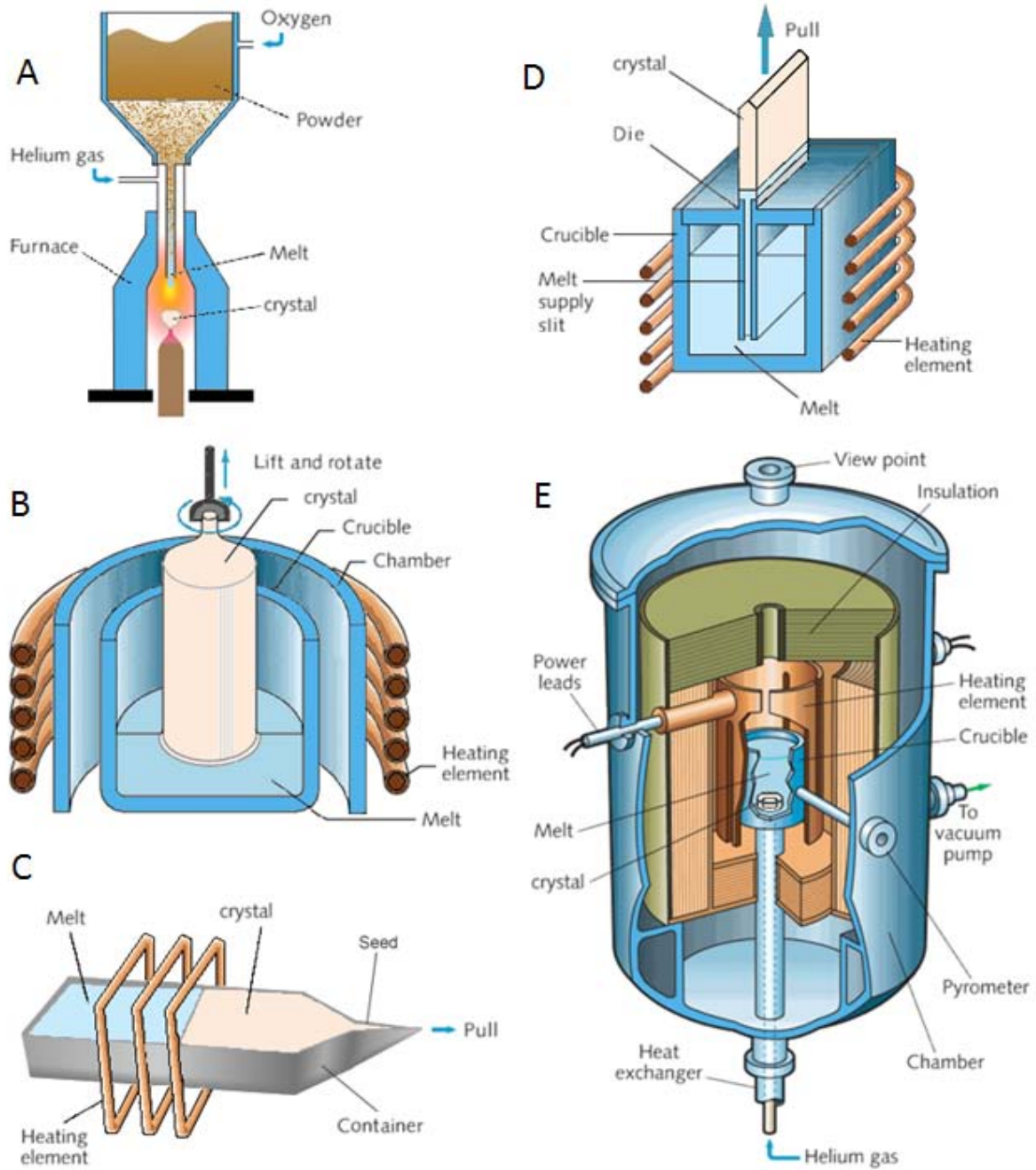


Figure 2-2. Crystal growth process schematics, A) Verneuil, B) Czochralski, C) Horizontal Directional Solidification Method (HDSM), D) Edge-Defined Film-Fed Growth (EFG) and E) Heat Exchanger Method (HEM)

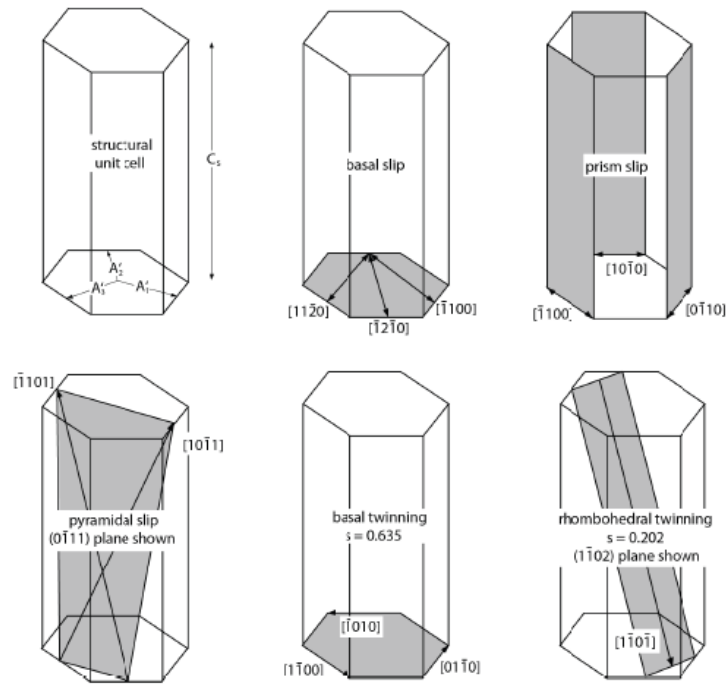


Figure 2-3. Depiction of slip and twinning systems in Sapphire

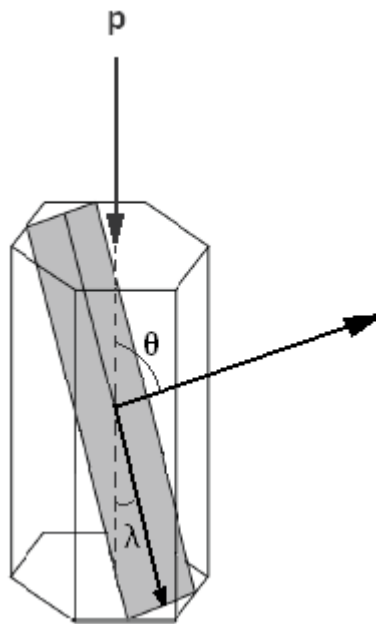


Figure 2-4. Graphical depiction of the relation of Schmid factor angles

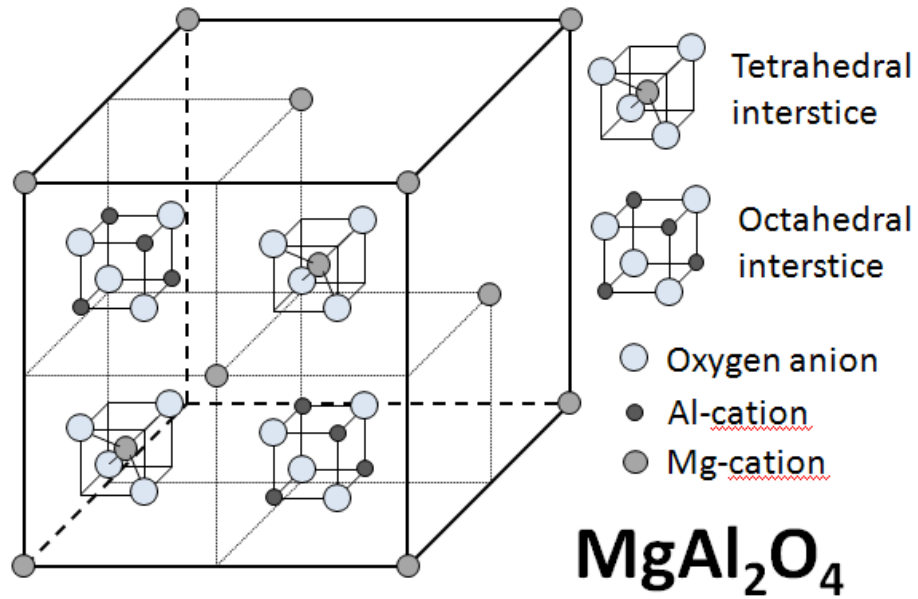


Figure 2-5. Schematic of the spinel unit cell. For clarity the octahedral and tetrahedral interstices are shown only in the front half of the unit cell.

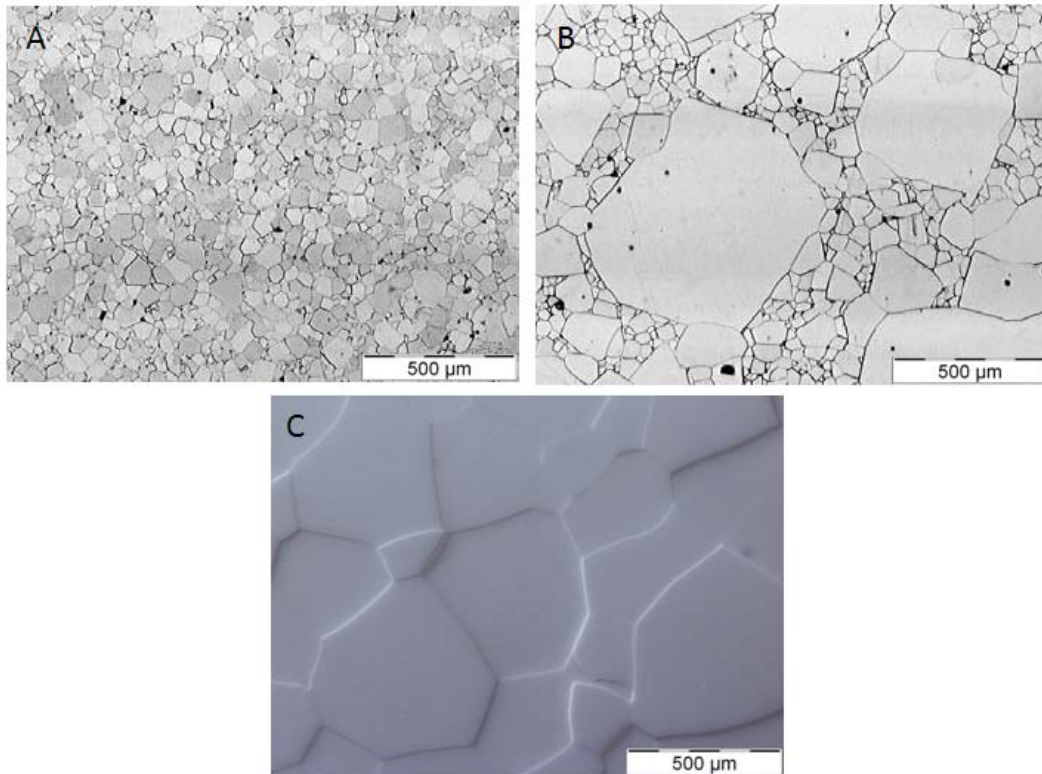


Figure 2-6. Optical images of example spinel microstructures. Included are A) fine grained [79], B) bi-modal [79] and C) course grained structures

CHAPTER 3 STATIC AND DYNAMIC INDENTATION RESPONSE

Introductory Remarks

An important application for spinel and sapphire is as a strike face material in transparent armor. Since the pioneering work of Wilkins et al., [1-7] it has been known that dynamic material characterization is paramount for ceramic armor design. Moreover, the hardness and fracture response of ceramic materials has been asserted as highly influential material properties affecting ballistic performance [15]. It is sensible that an understanding the strain-rate sensitivity of hardness and fracture behavior is then significant to the assessment of the ballistic performance of ceramics.

Several researchers have studied the shock behavior of sapphire [11, 69-73] and spinel [103-105]. Using flyer plate experiments, Kanel et al. [69, 70] conducted extensive research on shock loading of sapphire along various crystal axes using planar impact experiments in an effort to determine the Hugoniot elastic limit (HEL), defined as the dynamic compressive strength under uniaxial strain loading. Paris et al. [103] conducted similar experiments on polycrystalline (30 μ m grain size) spinel in an effort to determine the Hugoniot elastic limit (HEL), dynamic yield strength and spall strengths. Rozenberg et al. [9, 11] focused on the spall strength and loss of shear strengths following shocks above the HEL of these two materials. It was found that sapphire underwent a significant loss of shear strength when shocked above the HEL while spinel exhibited a loss of spall strength to nearly zero at elevated loading rates.

While significant advances in the understanding of fracture toughness of various sapphire orientations have been made [106], little progress has been published regarding the strain rate sensitivity of sapphire fracture behavior. The strain-rate

sensitivity of spinel fracture toughness has been investigated to a larger degree, yet the information reported does not explain rate sensitivity of indentation fracture. Baudín et al. [96] conducted single edge notched beam (SENB) experiments on a 35-100 μm grain size spinel at loading rates ranging from 0.005 mm/min to 2.5mm/min. They reported a roughly 20% drop in fracture toughness accompanied with a shift from intergranular to transgranular fracture with increased loading rates. A similar behavior was found to exist during controlled surface micro flaw fracture experiments on single crystal spinel by Stewart and Bradt [97]. Baudín and Pena [99] later repeated their earlier SENB experiments with spinels of varied alumina content this time reporting an elevated fracture toughness with increased loading rate.

While these testing efforts have revealed the rate dependant behavior of spinel and sapphire strength, they were insufficient in providing insight into the strain rate effect on hardness and the mode of indentation fracture under dynamic loads. Dynamic indentation experiments on the other hand can provide such information. Variants of these experiments have been successfully employed to provide insight into the strain rate dependence of several crystalline materials [48, 56, 107-112].

Chapter 3 details a comparative analysis of hardness as well as fracture initiation and propagation characteristics of *a*- and *c*-plane sapphire as well as a coarse grained polycrystalline magnesium spinel due to static and dynamic indentations. Additional calculations of brittleness parameters were made in order to describe the rate sensitivity of the propensity for brittle fracture for each material. Lastly an analysis of fracture modes during static and dynamic conditions is presented.

Experimental Methods

Material Preparation

Square tiles of dimensions 76mm×76mm×7.6mm of *a*-plane sapphire were obtained from Saint Gobain Crystals, Milford, NH. These tiles were grown using the edge defined film-fed growth (EFG) process [113]. Figure 3-1 is an illustration of the sample tiles indicating the dimensions and crystallographic orientation. Several 6mm cube samples were then cut from the tile exposing both *a*- and *c*-plane surfaces. Both *a*- and *c*-plane surface samples were then ground and polished to remove all visually distracting surface scratches created by the manufacturing or cutting process using progressively finer silicon carbide grinding media (320, 400, 600, 800 1040 and 1200 grit) followed by diamond paste polishing medium (6, 1 and 0.5 μm). The quality of the resulting polished surface was evaluated visually under an optical microscope at 100X magnification.

Additionally, samples of a high optical grade magnesium spinel were supplied by Technology Assessment and Transfer, Annapolis, MD. The material was supplied with two opposing faces in a polished condition requiring no further surface preparation. The materials were supplied as small square tiles (25mm x 25mm x 5mm). All samples were produced by a hot press (HP) process utilizing a lithium fluoride sintering aid followed by hot isostatic pressing (HIP). The average grain size of the material was determined to be ~ 250 μm using the lineal intercept procedure detailed in section 10 of the ASTM E112 standard [114]. A micrograph of the grain structure of the material tested is shown in Figure 3-2.

Several static indentations were made on both the *a*- and *c*-planes of the prepared sapphire samples as well as the polished surface of the spinel samples using

a Vickers indenter (Wilson®109 Instruments Tukon® 2100B) with indentation loads in the range of 0.5–19.6N (0.05–2 kg). While the supplied tile dimensions were sufficient for static indentation tests, smaller samples were cut to approximately 5mm x 5mm x 5mm cubes to facilitate dynamic indentation tests. Dynamic indentation testing was conducted using a dynamic indentation hardness tester (DIHT) [115]. The function of the DIHT will be explained in detail in the following section.

Crack lengths and crack orientations were measured for both static and dynamic indentations using an optical microscope. The measurements were then compared to assess the strain rate effect on hardness and crack lengths for both *a*- and *c*-plane sapphire and spinel. It should be noted that the convention used to measure and annotate crack lengths differs slightly for sapphire due to the nature of crystallographically aligned crack systems. Traditionally, radial crack length “ $2c$ ” is defined as the distance between the two opposing crack tips originating from the opposing Vickers indentation corners [116]. In the case of indentation on sapphire, corner cracks do not appear, instead cracks initiate preferentially along specific crystallographic planes irrespective of indentation corner location. Therefore, for the purposes of this study the crack length “ $2c$ ” is simply defined as the distance between two opposing crack tips oriented along the same crystallographic plane. These cracks may or may not emanate from the corners of the indentation but will always propagate along predetermined crystallographically oriented directions.

Dynamic Indentation Hardness Tester

The dynamic indentation testing technique utilized here is based on a modified split Hopkinson pressure bar (SHPB) setup which is able to generate a single Vickers indentation with a loading duration of approximately 50–200 μ s [117]. The average strain

rate of deformation during dynamic indentation can be determined from the size of indentation and velocity of indenter. Typical strain rates are on the order of 1000/s. In this technique a striker bar is accelerated towards a flanged incident bar by a pneumatic pressure gun. A schematic of the DIHT apparatus is shown in Figure 3-3. The incident bar has a Vickers indenter press fit to one end and a momentum trap on the impact end. The test specimen was positioned between the Vickers indenter and a load cell which is anchored to a rigid support. No gap was allowed between the Vickers tip and the specimen test surface. The striker bar impact onto the incident bar creates an elastic compressive pulse followed by a tensile wave (from the momentum trap) both of which travel the length of the incident bar towards the indenter end. The compressive pulse causes a single indentation on the test sample and the tensile pulse retracts the Vickers tip away from the test specimen.

Both of these pulses reverse in sign and travel back towards the impact end where the reflected tensile pulse is captured by the momentum trap and the reflected compressive wave reflects back again as a tensile wave traveling towards the indenter tip. This wave travels back and forth in the bar as a tensile wave towards the indenter tip and as a compressive wave traveling towards the impact end. Thus, all of the tensile waves traveling towards the indenter cause the indenter tip to retract away from the specimen preventing subsequent indentations [115, 117]. The time-based indentation load signal is captured using a high frequency load cell and a digital oscilloscope. Unlike the static indentation, the load of the dynamic indenter cannot be precisely set due to the slight variations in the velocity of the striker bar as it travels through the gas gun (i.e. frictional effects). Therefore, a minimum of 50 indentations was conducted at room

temperature on each test specimen to insure a varied load range. Hardness values were calculated based on the measured indentation diagonal lengths (not half crack length) and the measured load.

Results

Static and Dynamic Hardness

Indentation hardness has been identified as an important material property associated with particle erosion resistance [23] and ballistic performance [15, 16]. Since these damage events are characterized as dynamic, it follows that a measure of the strain rate sensitivity of indentation hardness is relevant. Assessment of a material's hardness during dynamic indentations allows for more predictive models and better correlations with observed phenomena during impact tests.

The static and dynamic hardness values for *a*- and *c*-plane sapphire as a function of indentation load are provided in Figure 3-4A and Figure 3-4B. The static hardness values are reported as the average of at least 10 indentations at each load while the dynamic hardness values are shown as individual data points. The data that was generated for both surfaces was curve fit in Figure 3-4C as per Meyer's law [118]:

$$P = Ad^n \quad (3)$$

where P is the indentation load, d is the indentation diagonal, A is the Meyer's prefactor and n is the Meyer exponent. Both sapphire orientations demonstrated a noticeable indentation size effect (ISE) with the *c*-plane being more pronounced than the *a*-plane. When the data is plotted in the Meyer's law format this difference in ISE between the planes can be numerically established. The Meyer exponent, a measure of the ISE, was

found to be approximately 1.8 for both configurations. These values were consistent with previous ISE studies of single crystal oxides [119, 120].

Both *a*- and *c*-plane sapphire demonstrated an increase in hardness under dynamic indentation. The *c*-plane sapphire yielded a slightly higher increase (12% versus a 10%) than for *a*-plane sapphire. These results are similar to earlier reports of dynamic indentation on polycrystalline alumina [107]. These results are also consistent with Tymiak et al. [52] and who reported an increase in yield point of *a*- and *c*-plane orientations with increased loading rates. It is also interesting to compare the greater strain rate sensitivity of the *c*-plane sapphire to the findings of Kanel, [69, 70] who reported the largest increase (51%) in the HEL response with increased impact velocity for sapphire along the *c*-axis as compared to only 47% along the *m*-axis. The results demonstrate a correlation of the rate sensitivity of hardness with published HEL values and could be considered when utilizing sapphire for ballistic applications.

The measured indentation hardness did not seem to be dependent on the orientation of the Vickers indenter tip with respect to sapphire crystal orientation. This result was inconsistent with earlier findings of anisotropy in Knoop hardness on sapphire basal plane [121]. It is, however, acknowledged that anisotropy exists on sapphire basal plane. The discrepancy is believed to be due to the fact that Vickers hardness is calculated based on an average of two equal length indenter diagonals while Knoop hardness is calculated purely by the length of the long diagonal. It is, therefore, expected that the anisotropic response is averaged out during Vickers hardness calculations while it is captured during Knoop calculations.

Static and dynamic Vickers hardness as a function of indentation load for spinel was also measured and is given in Figure 3-5A. The data is also presented in Meyer's format in Figure 3-5B. Consistent with the sapphire hardness results the spinel static hardness values are reported as the average of at least 10 indentations at each load while the dynamic hardness values are shown as individual data points. As stated earlier, the average grain size of the spinel was approximately 250 μm . Since the largest indentation diagonals recorded were on the order of 60 μm , many indentations fell within the boundaries of a single grain. Using a Nomarski optical filter, verification of the location of each indentation with respect to the grain boundaries was made. In this manner only hardness values from indentations that were placed inside the grain boundaries were reported. Therefore, the hardness data presented can effectively be thought of as that of randomly oriented single crystal spinel hardness. Although spinel is largely presented as a cubic and therefore isotropic material, the anisotropy of hardness as a function of crystal orientation has been well established [84, 120]. Due to the random nature of the crystal orientation in individual grains a significant scatter, likely due to anisotropy in hardness of the material, was evidenced by the large error bar at each indentation load in Figure 3-5A. Each error bar represents +/- one standard deviation.

A strain rate hardening effect is witnessed with spinel as the dynamic indentation hardness tests yielded approximately a 5% increase over the static hardness across all loads. Both static and dynamic indentation tests yielded a large indentation size effect (ISE) with a Meyer exponent of 1.95 shown in Figure 3-5B. The Meyer exponent, an indication of a material's ISE, is substantially higher than that of single crystal sapphire.

It was also observed that the ISE for spinel was consistent between static and dynamic indentations.

Static and Dynamic Brittleness

A brittleness parameter is a measure of the susceptibility of a material to undergo brittle cracking when subjected to a load. Knowledge of the brittleness parameter can assist in ranking of materials in terms of their ability to absorb energy as well as remain structurally intact. Various measures of brittleness have been proposed in literature [122, 123, 124]. The brittleness parameter can also be viewed as an inverse of the ductility parameter reported by Horii & Nemat-Nasser [125]. Lasalvia [15] utilized the ductility parameter to determine the characteristics of the impact induced zone in a ceramic target where it was found that an increasing ductility parameter (i.e. decreasing brittleness) reduces the damage zone. It is therefore of interest to calculate brittleness using static and dynamic material properties.

Various brittleness parameters have been proposed in literature. One brittleness parameter was proposed by Quinn and Quinn [122] as,

$$B = \left(\frac{H_C E}{K_{IC}^2} \right), \quad (4)$$

where E is Young's modulus, K_{IC} is the fracture toughness and H_C is the critical hardness described above.

A revised brittleness parameter (similar to the ductility parameter) was later proposed by Zhang and Subhash [123]:

$$B = \left(\frac{EY}{\sigma_f} \right)^{1/3}, \quad (5)$$

In this expression Y is the yield strength and σ_f is the fracture strength of the material. Notice that the brittleness parameter proposed by Zhang and Subhash [123] is unit-less where the parameter defined by Quinn and Quinn [122] has units of inverse length.

The static yield stress of a brittle material is estimated by the relation to static hardness proposed by Zhang and Subhash [123]

$$Y = \left(\frac{H^4}{E} \right)^{1/3} \quad (6)$$

The dynamic yield stress however, is estimated from its relation to dynamic property HEL proposed by Rosenberg [126],

$$Y = \frac{(1 - 2\nu)^2}{1 - \nu} HEL \quad (7)$$

where ν is Poisson's ratio and HEL is the Hugoniot Elastic Limit.

Using the static and dynamic hardness data discussed in the previous section as well as published static and dynamic material properties static and dynamic brittleness parameters are calculated for both sapphire and spinel. Because of the lack of rate sensitive fracture toughness data needed to calculate brittleness using the Zhang and Subhash [123] approach, the Quinn and Quinn approach will be used to draw comparisons between the two materials. In order to utilize the Quinn and Quinn [122] approach, a value for critical hardness for each material must be found. This is determined by locating the transition point, corresponding to an abrupt change in load dependence of hardness. The concept of a transition point and critical hardness in a load hardness plot is described in detail by Quinn and Quinn [122]. The critical hardness for sapphire and spinel was determined and is graphically depicted with

dashed lines in Figure 3-6A for a-plane sapphire, Figure 3-6B for c-plane sapphire and Figure 3-6C for spinel. The transition point essentially identifies the point at which a sharp change in the slope of load dependence on hardness occurs. It is recognized that the exact location of this point is somewhat subjective and can vary depending on which data points are selected to determine each slope. As such a method of choosing data sets for each slope line that resulted in the highest R^2 fit for each slope line was used to graphically determine the transition point. The hardness at this transition point is defined by Quinn and Quinn [122] is defined as the critical hardness (H_C). H_C has been proposed as an indication of a switch to a more fracture dominated energy absorption mode during the indentation process. As such this value is used to predict the onset of brittle fracture. For a-plane sapphire, the static and dynamic critical hardness were found to be ~18GPa and ~20.6GPa respectively while c-planes sapphire yielded critical hardness values of ~16.7GPa for static indentations and ~18.8GPa for dynamic indentations. The critical hardness for spinel was found to be ~14.1GPa for static indentations and ~14.7GPa for dynamic indentations. Using the Quinn and Quinn [122] approach, the static brittleness of spinel was found to be $1027 \mu\text{m}^{-1}$ which is in reasonable agreement with earlier studies of spinel brittleness [127]. Under dynamic loading conditions the calculated brittleness values increase to $1071 \mu\text{m}^{-1}$. It can be seen that the dynamic brittleness value is approximately 4% greater than that of the static brittleness.

In comparison, the static brittleness of a-plane sapphire was found to be ~1177 μm^{-1} while c-plane sapphire static brittleness was calculated to be ~1647 μm^{-1} . This illustrates a significantly greater level of static brittleness in sapphire than spinel. A 15%

increase in brittleness for *a*-plane sapphire and a 60% increase in brittleness for *c*-plane sapphire can be seen when compared to spinel. Under dynamic loading conditions the margin increases. The dynamic brittleness of *a*-plane sapphire was found to be $\sim 1177 \mu\text{m}^{-1}$ ($\sim 25\%$ increase over spinel) while the dynamic brittleness of *c*-plane sapphire was calculated to be $\sim 1177 \mu\text{m}^{-1}$ ($\sim 73\%$ increase over spinel). Also it is noteworthy to see that the brittleness of sapphire is more strain-rate sensitive than spinel. While spinel brittleness increased by 4% when subjected to dynamic loading, sapphire increased by 14% (*a*-plane) and 12% (*c*-plane). Table 3-1 summarizes the calculated brittleness parameters as well as a list of the static and dynamic properties used in these calculations.

Recall for spinel that the indentation hardness is effectively that of randomly oriented single crystal spinel and the brittleness parameter by definition is effectively a ratio of plastic deformation energy to fracture energy. Subsequently, an increase in brittleness of spinel can be thought of as an indication of increased tendency for brittle grain fracture during dynamic impact conditions. An increase in brittleness in sapphire however would be thought of as a reduced capacity for maintaining structural integrity since the material is more prone to fragmentation. This is due to the fact that sapphire is a single crystal material with no grain boundaries able to modify crack propagation. In physical terms for both materials, an increase in brittleness has been linked to decreasing fragment size during dynamic impacts [128].

Static and Dynamic Indentation Fracture

An understanding of the fracture behavior of a material is also critical in the assessment of erosion and impact resistance. LaSalvia [15] presented fracture toughness as a limiting measure of a materials ability to resist penetration while Krell

and Straßburger [16] listed mode of fracture as a key influence during the penetration process. Although concerns regarding the validity of assessing fracture toughness by the indentation method exist [129], the mode of fracture can easily be determined by indentation tests. Furthermore, a comparison of fracture modes during static and dynamic indentation is possible.

In the case of sapphire, indentation creates surface features and fracture patterns that are quite different in appearance than other transparent glasses and ceramics due to its preferential crystallographic fracture planes (Figure 3-7). The origin, the evolution and the strain rate sensitivity of these surface feature patterns have been studied extensively over the past 6 decades. The appearance of these unique fracture patterns surrounding an indentation impression in sapphire was first reported by Attinger [130] who described the appearance of oriented fissure-like cracks. Hockey [131] first identified the existence of basal and rhombohedral micro-twins surrounding the indentation impressions on single crystal sapphire but was reluctant to fully attribute twinning mechanisms as the source of crack formations. Several subsequent indentation studies [132-135] performed on various sapphire orientations reported observations of basal and rhombohedral twinning as well as basal, rhombohedral, prism and pyramidal slip. Nowak et al. [45] first developed an effective resolved shear stress (ERSS) model that estimated the peak shear stress acting on slip and twinning systems and consequently proposed a “T-parameter” which predicted the activation of each slip and twinning systems during indentation of a -(1210), m -(1010) and c -(0001) planes of sapphire. For example the peak probability for rhombohedral twinning on the c -plane was predicted at relative angles of 0° , 120° and 240° with no experimental correlation

presented. The peak probability of basal twinning on the *a*-plane was predicted to occur at relative angles of 90° and 270° (axisymmetric with respect to the [0001] direction) while the peak probability of rhombohedral twinning on the *a*-plane to be at relative angles of 90°, 225° and 315°. Comparisons of predictions of slip and twinning system activation probability were found to poorly correlate to the experimental observations of cracks and linear surface features on *m*-plane sapphire [46, 47]. In fact their experimental observations indicated basal twinning rather than rhombohedral twinning to occur at 90°, 225° and 315°. Additionally, Nowak et al. [45] described the appearance of surface traces on both *a* and *m*-prism planes to be essentially the same with only a trivial 90° shift in angular positions. Subsequent experimental findings have demonstrated that the patterns of plastic deformation are distinctly different between *a*- and *m*-plane sapphire [51, 56]. These findings were later reinforced by Tymiak and Gerberich [49] and Tymiak et al. [136] through analytical RSS modeling and FEA analysis. While the modeling efforts of Nowak et al. [45] did not precisely capture all of the observed trends, their pioneering work provided a first look at surface orientation effects on patterns of contact-induced plasticity in sapphire. Additionally, the significance of the role of basal and rhombohedral twinning on contact induced plasticity in sapphire was predicted.

More recent experimental findings from Kim and Kim [51] attempted to correlate experimentally observed surface traces to the intersection of sapphire crystal planes. Based on observations of fracture sequence of (1120) sapphire with a physical vapor deposited TiN coating they reported a relative angle of 122.4° between what they asserted as rhombohedral and basal twinning traces (Figure 3-8). This angle

corresponded with the crystallographic intersection of the *r*-plane (1102) with the *a*-plane (1120) yet did not provide a rationale for the appearance of this twinning trace over other possible rhombohedral twinning systems.

Modeling efforts by Tymiak and Gerberich [49] yielded a resolved shear stress (RSS) distribution map for all of the known slip and twinning systems. The model produced an upper and lower bounds for the critical resolved shear stress (CRSS) required to activate a given deformation system at room temperature due to indentation. Their modeling provided a good correlation with previous experimental observations. In particular, the earlier findings of Kim and Kim [51] were rationalized due to indications of a higher RSS for the observed rhombohedral twinning system over other possible rhombohedral twinning systems. Although the results of Tymiak and Gerberich [49] correlated well with the observations of Kim and Kim [51] they expressed a reluctance to attribute the surface features to twinings without TEM analysis to confirm.

Static and dynamic indentations on basal (*c*-plane) and prism (*a*-plane) plane sapphire, shown in Figure 3-7, reveal three distinct surface features. Static indentations on *a*-plane (1120) sapphire at loads as low as 1N (0.1 kg) produced a series of wavy traces oriented perpendicular to the *c*-axis [0001] (images not shown here for brevity). The orientations of these traces are consistent with earlier findings from Chan and Lawn, [133] Nowak and Sakai [45] as well as Kim and Kim [51] who all identified these features as basal twins. With increased load evidence of some crack nucleation along these traces becomes evident although not all traces result in fracture formation (Figure 3-7A and Figure 3-7B). Consequently features identified as cracks following this orientation are depicted in all subsequent figures as B-cracks. At 2N (0.2 kg) loads, a

second set of cracks oriented at approximately 51.8° relative to the *c*-axis or 141.8° relative to the B-crack orientation appeared. This crack orientation is consistent with the intersection of the (0112) *r*- and (1120) *a*-planes and is referred to as R1-crack. With further increase in load a third crack system (referred to as R2-crack) oriented at approximately 38.2° relative to the *c*-axis or 122.4° relative to the B-cracks also appeared. This orientation is consistent with the intersection of the (1102) *r*- and (1120) *a*-planes. In order to better describe the idea of axis projection, a three-dimensional schematic illustrating the projection of basal and rhombohedral twinning cracks onto the *a*-plane is shown in Figure 3-8. The measured surface orientation of the B-cracks and the R2-cracks (122.4° relative to B-cracks) were consistent with the prediction of surface traces of well defined twins presented by Tymiak and Gerberich [49] as well as Kim and Kim [51] but the R1 feature (141.8° relative to the B feature) was not presented by either studies although Tymiak and Gerberich did mention that if other rhombohedral twinning systems were activated they would appear at 141.8° relative to the B features. Although TEM analysis would be needed to provide unambiguous conclusions as to the origin of the observed features, the measured angles of each feature suggest basal and rhombohedral twinning or slip as the source of fracture. It is also noted from the crack orientations that these cracks do not necessarily initiate from the corners of the Vickers indentation. This would indicate that the energy required to propagate cracks along these preferential directions is lower than what is required to produce radial cracks even with stress concentrations at the indenter corners.

Upon closer inspection the B-cracks tended to have a jagged appearance shown in the enlarged views of the micrographs as seen in Figure 3-9. The crack front seems

to repeatedly switch between B-crack and R2-crack directions in a periodic manner. Eventually, the R2 direction dominates and a permanent change in direction is witnessed. This behavior indicates a competition between B and the R2 systems possibly due to a combined effect of the critical stress differences between crystallographic planes and the applied stress field.

It is also interesting to note that both the R1 and R2 rhombohedral cracks would bridge between the zones along the *c*-axis [0001] direction while they would not bridge in zones oriented along the *m*-axis. These zones are identified as “weakened zones” in Figures 3-7A and 3-9. This tendency to bridge is believed to be encouraged by prism slip mechanisms which have the highest shear stress concentrations in the area oriented along the *m*-axes per Tymiak and Gerberich’s model [49]. With increasing macro indentation load, this region tends to laterally crack in a more severe manner than other regions surrounding the indentation site. This phenomenon creates an inherently weak zone surrounding the indentation site. In the next section, a demonstration of the importance of these weakened zones during multiple interacting Vickers indentation will be discussed in relation to multi-hit performance of a sapphire target.

Indentations on *c*-plane sapphire produced cracks propagating at angles of 120° relative to each other with additional “corner cracks” propagating from the corners of the indenter. These crack orientations seem to be consistent with the angular separation of peak probability for activation of rhombohedral twinning on basal plane sapphire as proposed by Nowak et al. [45-48]. Again without TEM analysis it is presumptuous to state the exact origins of these cracks.

For both surface orientations, cracks due to dynamic indentation appear in a similar orientation as the those due to static indentation but are generally shorter and are accompanied with an increase in localized spalling underneath the indentation (Figure 3-10). The half crack length as a function of indentation load is shown in Figure 3-11. The crack length measurements indicate a reduced crack length as a function of load for both orientations under dynamic loading as compared to static loading. Additionally, the slopes of half crack length vs. load for the dynamic indentation cracks were less steep than that for static indentations indicating that the cracks were less sensitive to load at higher loading rates. Due to the varied slopes between static and dynamic indentation a constant reduction in crack length was not evident. Rather the crack length reductions rose to 26-35% at 1Kg loads for various orientations. This again reinforces the idea that the behavior of sapphire tends to shift from long crack propagation to a more localized micro-cracking during high strain rate indentations.

It is also interesting to note that while the B-cracks seemed to initiate at a lower load (Figure 3-11B), R1 cracks had a higher rate of growth under increasing loads than the basal cracks (Figure 3-11A). Although this difference is minor it again illustrates the idea of a crossover of preferential crack systems from basal to rhombohedral under increasing loads.

The indentation fracture behavior of spinel was quite different. Instead of fractures preferentially following crystallographic planes as in sapphire, spinel indentations created cracks emanating from the indentation corners. In addition, the presence of grain boundaries in the area of an indentation significantly altered the indentation fracture behavior.

Examples of static Vickers indentations and associated crack patterns at comparable loads for spinel are shown in Figure 3-12. Figure 3-12A depicts a static indentation placed within a large grain and away from any grain boundaries. Cracks emanating from each of the indentation corners are clearly witnessed accompanied by distortion of the surrounding area (as evidenced by the diffused light around the indentation). Figure 3-12B shows a static indentation placed in close proximity to a grain boundary. The corner cracks propagating toward a grain boundary at a relatively shallow approach angle easily deflect from their original trajectory and follow the grain boundary. Even at a much steeper approach angle as shown in Figure 3-12C, most of the crack energy is dissipated through grain boundary cracking. Lastly, Figure 3-12D depicts an indentation placed directly on the grain boundary. It is clearly evident that in addition to indentation intragranular corner cracks, additional grain boundary (intergranular) cracks emerge from the sides of the indentation. Due to the low contrast present in these materials, the grain boundaries are difficult to distinguish and are therefore marked by dashed lines.

In Figure 3-12D, despite the fact that the stress intensity is significantly lower at the indentation sides (where the grain boundaries are located) as compared to the indentation corners (where the highest stress intensity exists) the intergranular grain boundary cracks are longer than the intragranular corner cracks. Measurements of these crack lengths on several indentations placed in the interior of the grains and along the grain boundaries revealed an 18% increase in intergranular crack lengths compared to intragranular crack lengths as shown in Figure 3-13. Both type of cracks follow a relationship between half crack length 'c' and applied load 'P' of the form $c \propto P^{2/3}$. This

relationship has been proposed as an indication of the crack type as median/half-penny rather than radial [109, 137]. However, progressively polishing of an indentation reveals the corner cracks to be radial as shown in Figure 3-14. Additional evidence from Figure 3-14 suggests the lateral cracking that is witnessed does not originate from the indentation tip as commonly described in literature [135]. Polishing to the depth of complete indentation removal (Figure 3-14D) has not revealed the lateral cracks. Lateral cracks are still evident from the diffused light that is clearly visible surrounding the indentation site. It is therefore evident that the lateral crack must be deeper into the material.

A series of images of cracking due to dynamic indentations on spinel are shown in Figure 3-15. A typical dynamic indentation placed within a grain is shown in Figure 3-15A. When compared to an equivalent static indentation (Figure 3-12B) at comparable load levels it can be seen that under dynamic loading several secondary radial cracks appear in addition to the onset of lateral cracking which is seen under an optical microscope as diffused light reflecting from internal crack planes. Additionally, some evidence of spall directly under the indentation can be seen confirming an increase in brittleness. Figures 3-15B and 3-15C depict dynamic indentations in close proximity to a grain boundary. It is noticed that cracks following a transgranular mode of fracture occur, as evidenced by several cracks crossing grain boundaries. This behavior is in contrast to crack deflection along the grain boundary in static indentations at similar loads and is further confirmation of an increase in brittleness under dynamic loads as reflected in the calculations shown in Table 3-1. Dynamic indentations, however, when placed directly on grain boundaries as shown in Figure 3-15D, resulted in mixed mode

cracking similar to the static loading case shown in Figure 3-12D. Additionally, an increase in lateral cracking was clearly evident as intense diffused light surrounding the indentation.

Figure 3-16 illustrates the half crack length ' c ' developed at various loads ' P ' due to dynamic indentations. A superimposed trend line confirms that the intragranular and intergranular half crack length due to dynamic indentations generally follow the same relationship with indentation load as in the static case (Figure 3-13). Due to the random nature of dynamic indentation placement and its orientation with respect to the grain boundary, positioning a dynamic indentation precisely on a grain boundary was difficult. This resulted in few successful indentations placed directly on grain boundaries yet enabling comparative measurement of intergranular and intragranular cracks. The lengths of grain boundary cracks resulting from the indentations that were successfully placed on grain boundaries seemed to exhibit the same 18% length increase over intragranular cracks as that of static indentations.

Both static and dynamic loading resulted in an increase in lateral cracking as the indentation load was increased. However dynamic loading also resulted in higher levels of spall with elevated loads. In contrast spall was never witness during static indentations up to 3 Kg. Figure 3-17 highlights the difference between static and dynamic indentation at elevated loads. Figure 3-17A shows a static indentation due to a 3Kg load where no evidence of spall is present, but strong evidence of transgranular fracture is evident. This could indicate a shift to transgranular fracture with increasing loads. In contrast Figure 3-17B shows a dynamic indentation of comparable load with significant increase in spall and fragmentation. The results indicate that brittle fracture

and spall can play an important role in deformation during highly dynamic events such as impact. In particular the observation of spalling directly beneath the indenter can be rationalized as a propensity for the creation of a comminuted zone of pulverized fragments directly beneath an impact site [138].

The hardness and crack length results provided in this section may have some relevance to sapphire behavior under projectile impact. It appears that projectile defeat is more likely with *a*-plane configuration rather than *c*-plane due to the combination of superior hardness and a reduced crack propagation behavior. In addition, although hardness increases under dynamic conditions for both orientations, the crack length reductions were accompanied with increased spalling and material comminution. This shift in fracture behavior demonstrates the idea that under dynamic conditions, energy is dissipated in a smaller region surrounding the indentation site with a greater reduction in local material structural adhesion but with a higher overall structural integrity as cracks are less prone to propagate large distances. This behavior could provide insight into the mechanisms that control the transition from interface defeat to penetration in sapphire materials as impact velocity increases.

Closing Remarks

Static and dynamic indentations were conducted on a coarse grain spinel. Hardness was found to increase by 5% while calculated brittleness was found to increase slightly (4%) during dynamic indentations. The Meyer's exponent describing the ISE was found to be approximately 2. The observed corner cracks from indentations within individual grains were confirmed as radial type by progressive polishing techniques. Dynamic indentation however produced significantly more radial cracks as well as spalling and lateral cracking. Intergranular cracking preferentially

occurred when static indentations were placed in close proximity to a grain boundary, while a shift to transgranular fracture mode was noticed during dynamic indentations as cracks more easily cross grain boundaries rather than deflecting along them.

Intergranular cracks were found to be on average 18% longer than intragranular cracks at similar indentation loads for both dynamic and static loading. As indentation load increased static indentations exhibited a tendency for transgranular fracture yet without any sign of spall however spall was present during high load dynamic indentations.

Static and dynamic indentations were also conducted on *c*- (basal) and *a*- (prism) plane sapphire. Both orientations exhibited a heightened increase in hardness under dynamic indentation accompanied with a less noticeable indentation size effect than spinel. Basal plane sapphire was also more sensitive to strain rate hardening effects with a 12% increase in hardness over static versus a 10% increase for prism plane sapphire. Basal plane sapphire was slightly more sensitive to ISE with a Meyer's exponent of 1.85 versus 1.81 for prism plane. Brittleness due to dynamic indentations was shown to increase by 14% and 12% for *a*- and *c*-plane sapphire respectively. This is a marked increase in brittleness due to dynamic indentations as compared to spinel. The resultant surface patterns on both sapphire orientations correlate well with previous experimental and analytical studies reported elsewhere. Wavy features (B) oriented along the basal plane are likely due to basal twinning and initiated at lower loads than other cracks oriented along the rhombohedral planes. The cracks (R1 and R2) oriented along the rhombohedral planes are possibly due to rhombohedral twinning or slip and with increased loads emerge as the preferential fracture modes. It was observed that cracks propagating along the basal plane would alternate between B and R2 crack

directions demonstrating a competing mode of crack propagation and differing reactions to applied stress fields. Weakened zones surrounding a-plane indentation sites are located along the c-axis. Crack behavior seemed to shift from long crack propagation to micro cracking and spalling under dynamic indentations. A 20–30% reduction in crack length was noted under dynamic conditions. Finally, the fracture mode observed under dynamic indentation has been related to the behavior of sapphire under impact conditions.

Table 3-1. Calculated brittleness parameters and material properties used for calculations

Loading Condition	E (GPa)	K_{IC} (MPa-m ^{1/2})	H_C (GPa)	B (μm ⁻¹)
Mg-Spinel				
Static	277	2.0 ^[85]	14.1	1027
Dynamic	277	2.0 ^[85]	14.7	1071
Sapphire (0001)				
Static	386	2.1 ^[106]	18	1177
Dynamic	386	2.1 ^[106]	20.6	1347
Sapphire (1120)				
Static	485	2.4 ^[106]	16.7	1647
Dynamic	485	2.4 ^[106]	18.8	1854

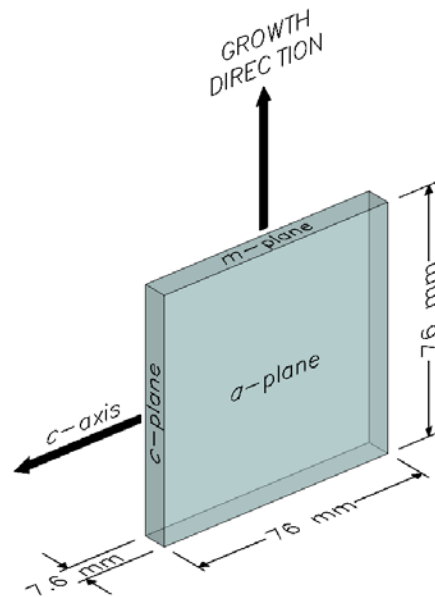


Figure 3-1. Schematic of the orientation of a-plane sapphire crystal tile supplied by Saint-Gobain crystals.

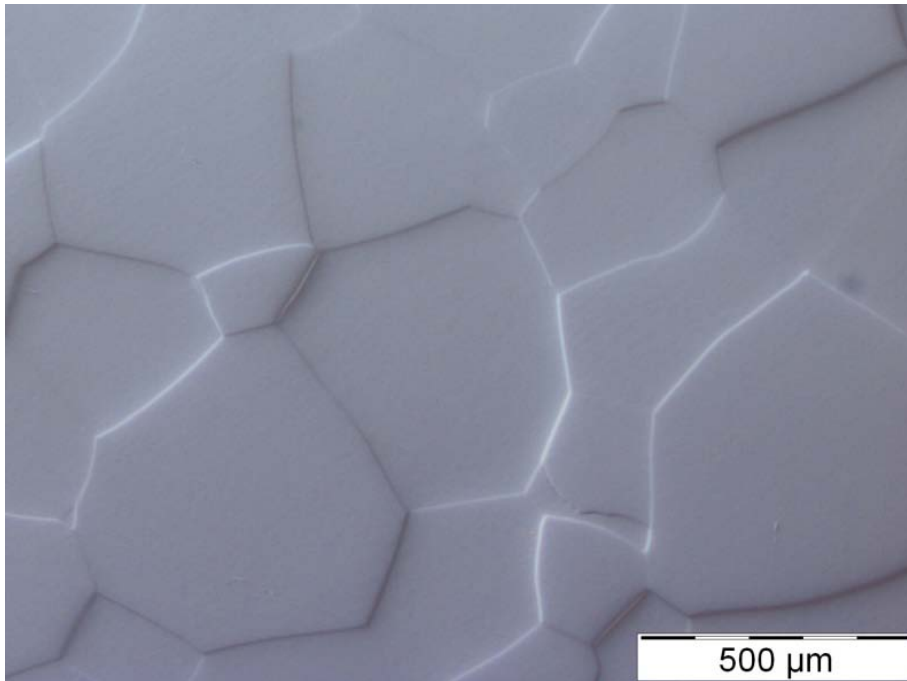


Figure 3-2. Optical image of the grain structure of the spinel supplied by Technology Assessment & Transfer

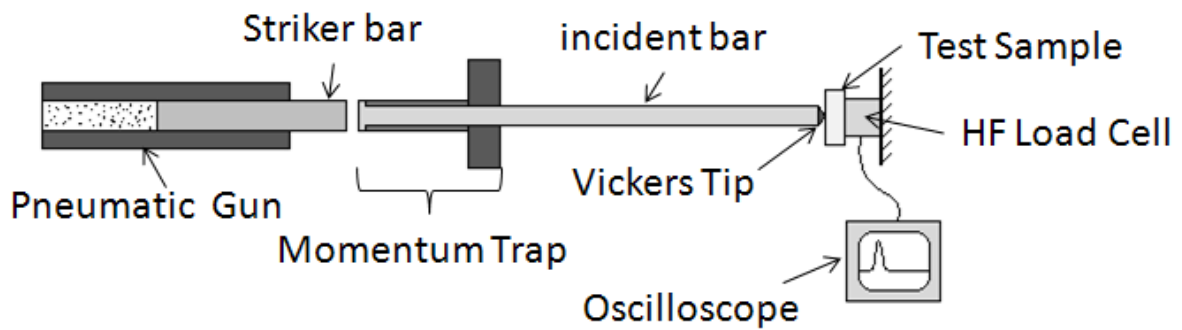


Figure 3-3. Schematic of the dynamic indentation hardness testing apparatus

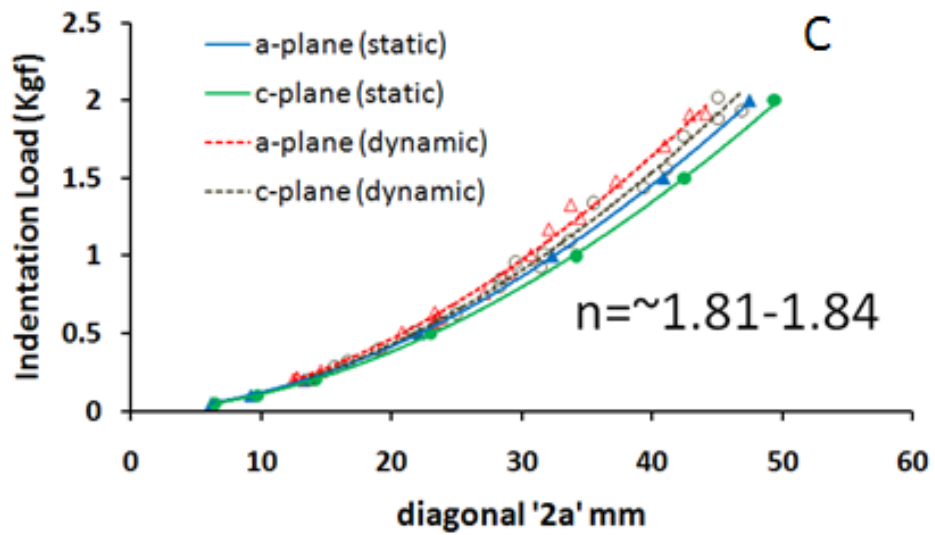
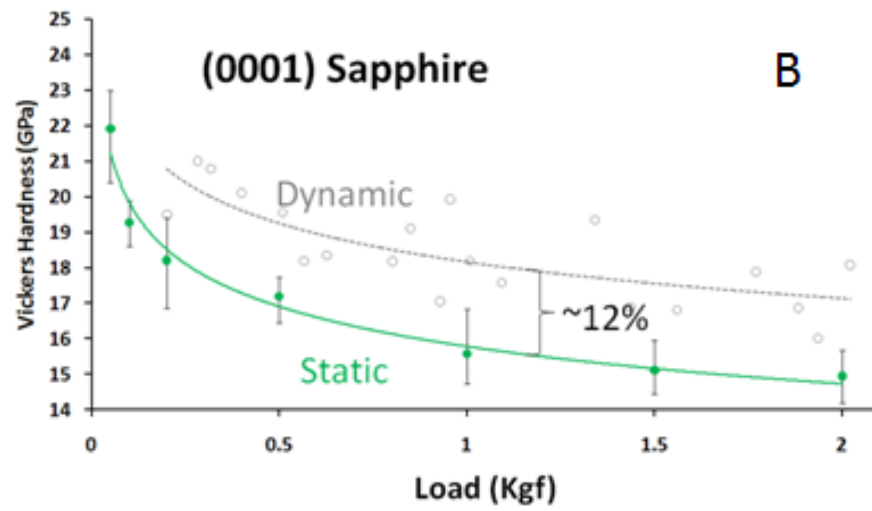
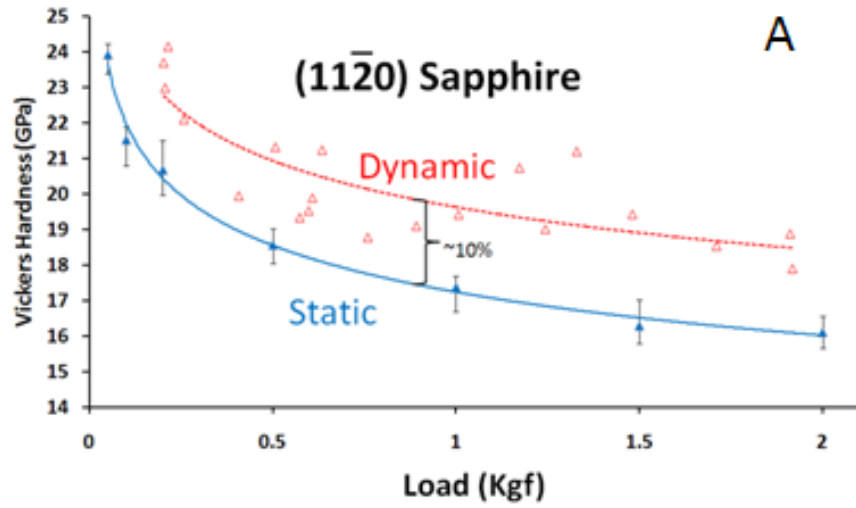


Figure 3-4. Static and dynamic hardness trends as a function of indentation load. Data for A) (1120) sapphire, B) (0001) sapphire and C) Meyer's law fit for the above data.

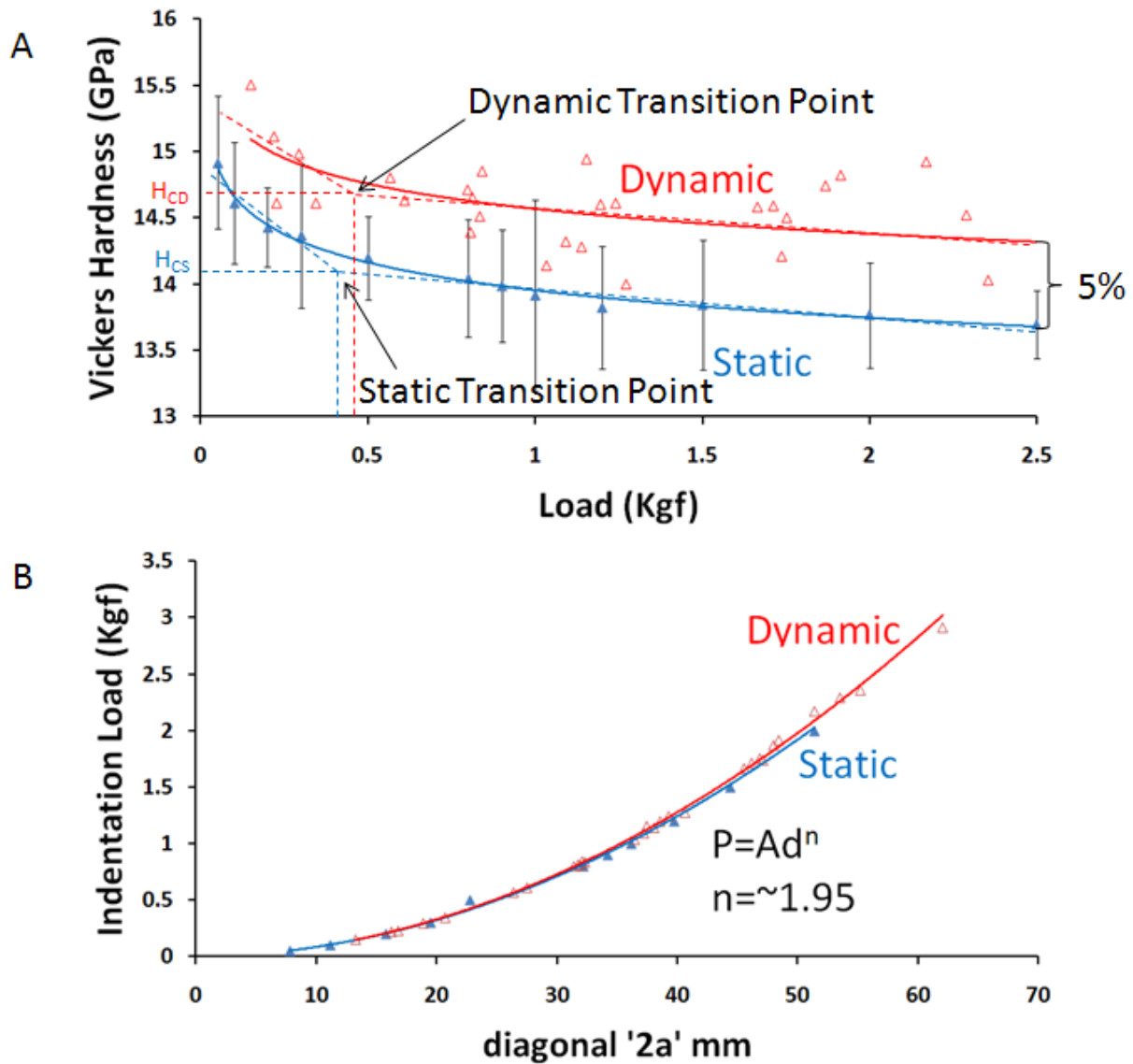


Figure 3-5. Graph of static and dynamic indentation hardness of spinel. A) Hardness vs. load and B) Meyer's law plot format.

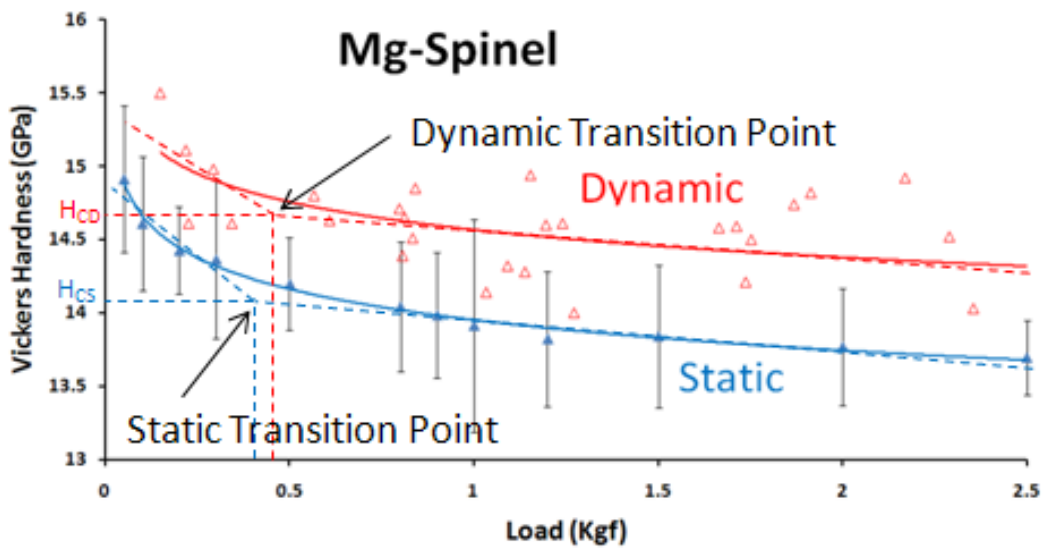
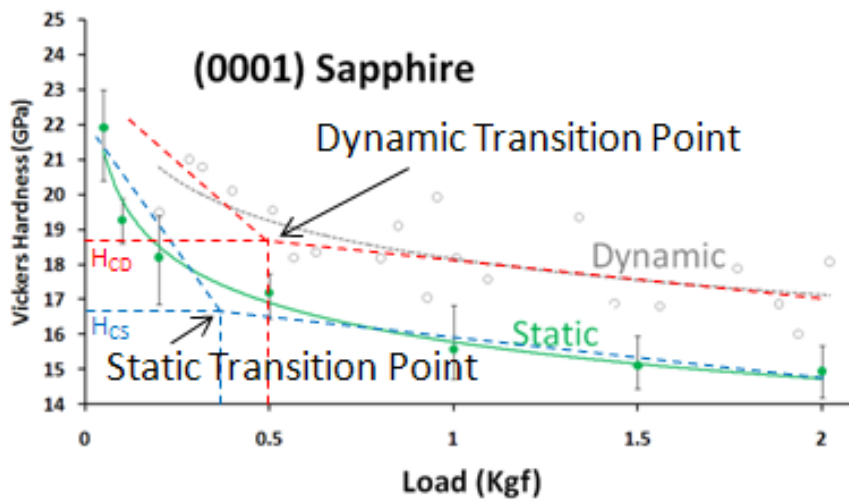
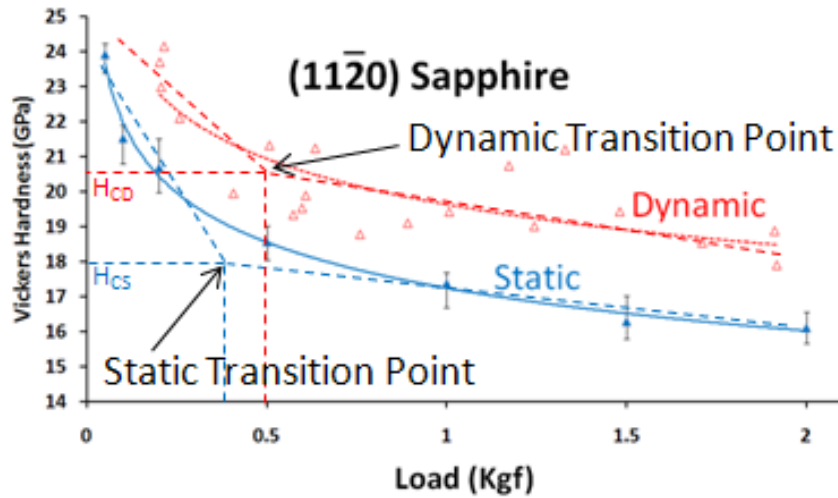


Figure 3-6. Graph of static and dynamic indentation hardness showing critical hardness. Shown for A) (0001) Sapphire B) (1120) Sapphire and C) Mg-Spinel

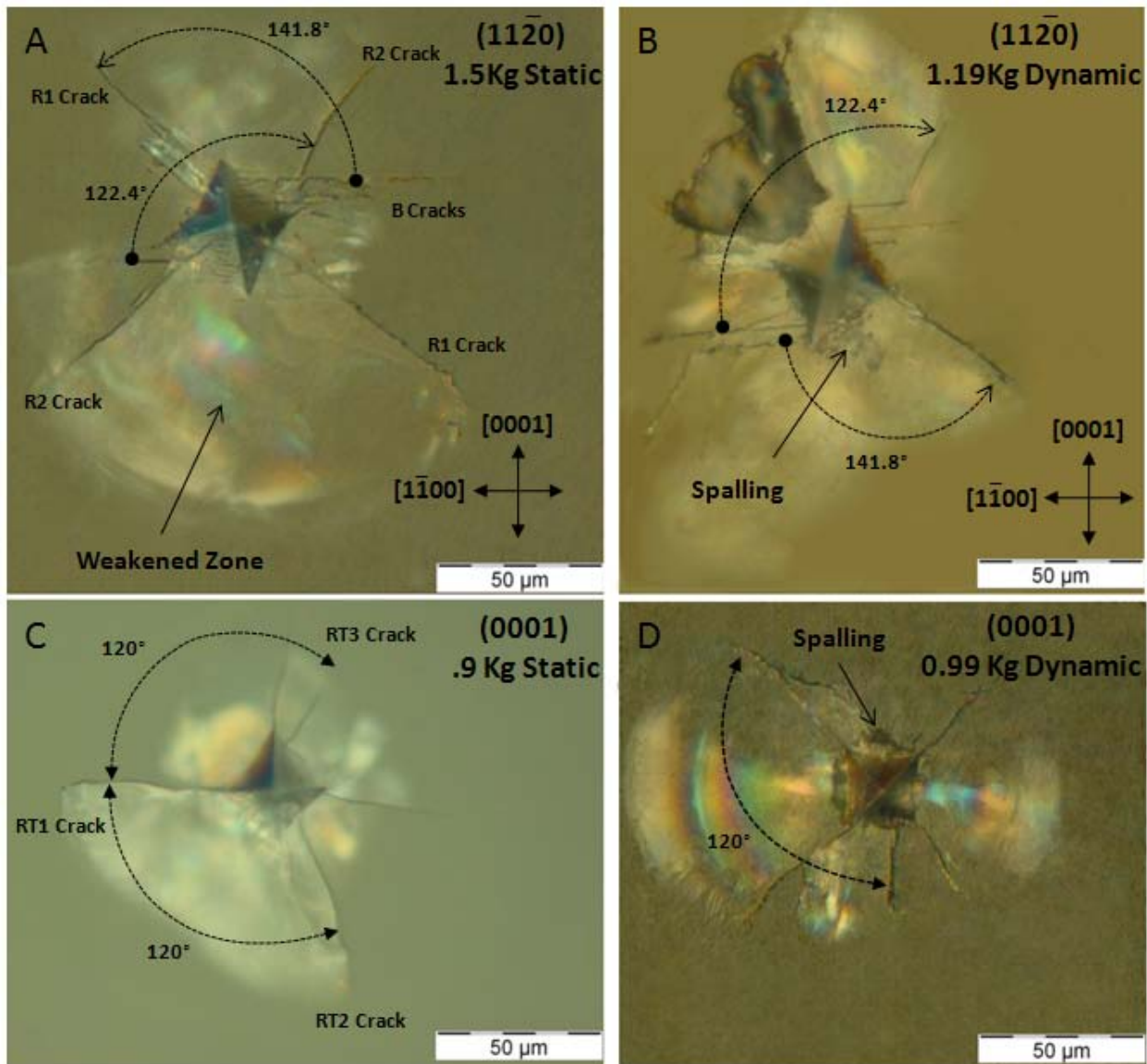


Figure 3-7. Static and dynamic indentation fracture patterns. Examples of A) static and B) dynamic indentations on *a*-plane sapphire as well as C) static and D) dynamic indentations on *c*-plane sapphire are shown.

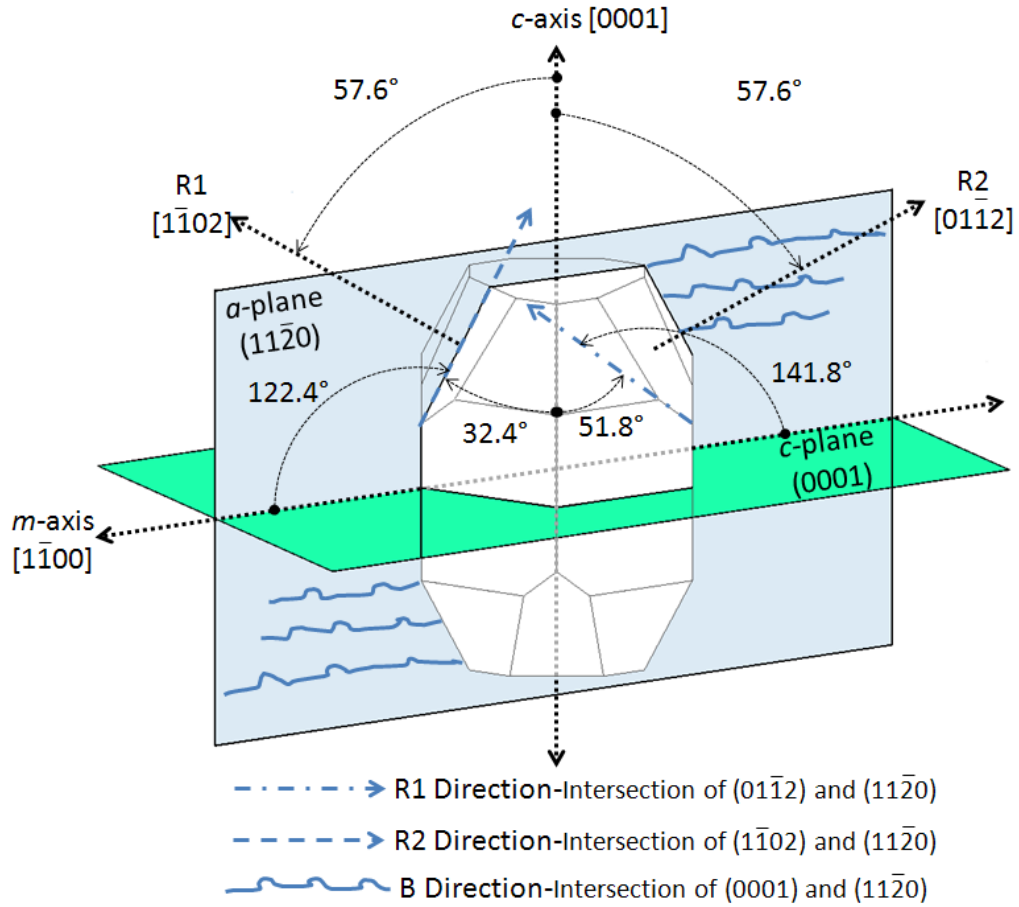


Figure 3-8. Schematic of sapphire crystal axes projected angles and the relevant preferential crack systems.

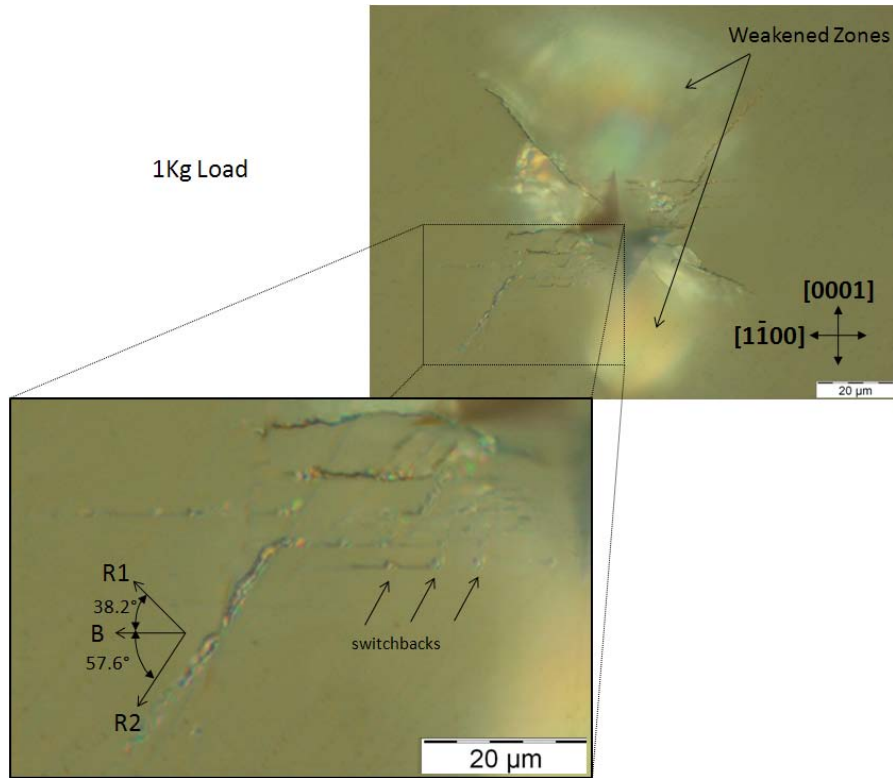


Figure 3-9. Enlarged view of jagged appearance of B cracks during static indentation on *a*-plane sapphire.

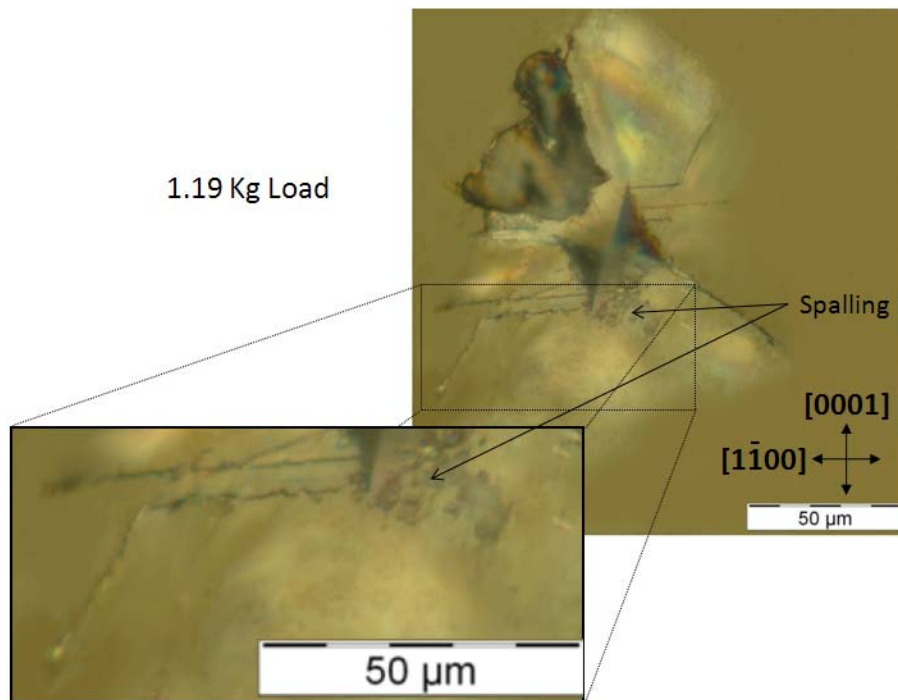


Figure 3-10. Enlarged view of dynamic indentation on *a*-plane sapphire showing increased spalling during dynamic indentation.

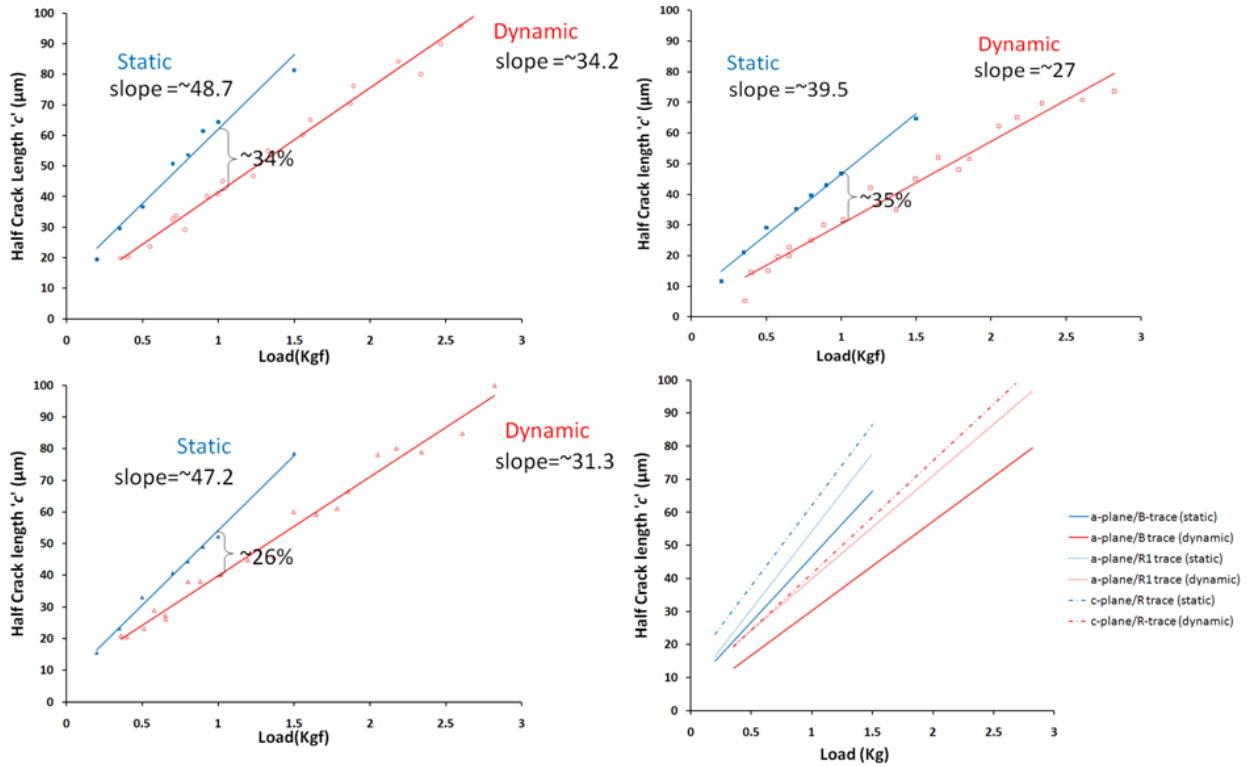


Figure 3-11. Half-crack length 'c' as a function of indentation load 'P' of a-plane and c-plane sapphire under static and dynamic indentations. Data shown for A) R1-cracks on a-plane sapphire, B) B-cracks on a-plane sapphire, C) R1-cracks on c-plane sapphire and D) trend lines for all the data combined.

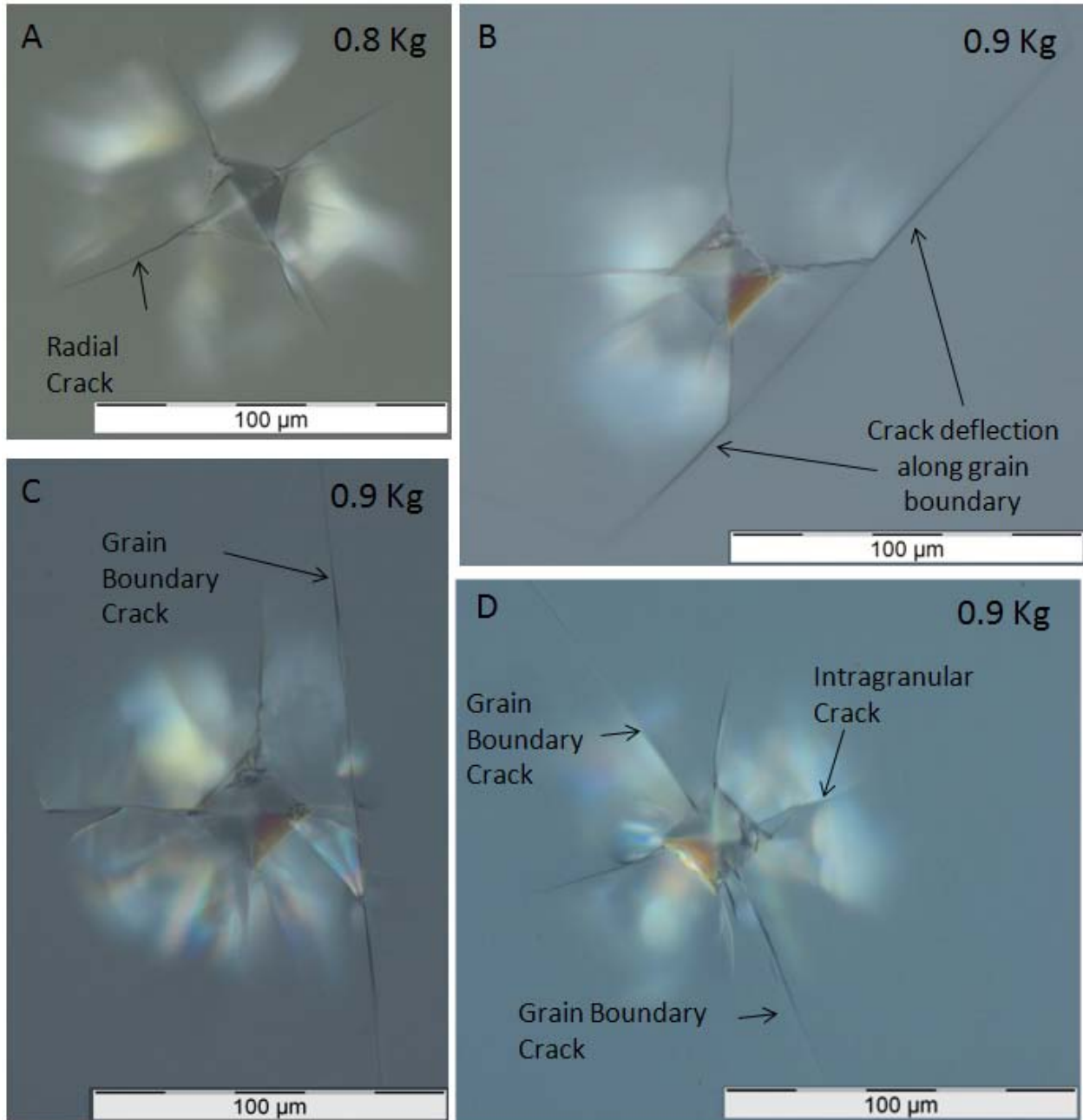


Figure 3-12. Optical images of induced crack patterns due to static indentations on spinel. Images shown include indentations located A) in the interior of the grain, B) and C) in the vicinity of a grain boundary and D) along the grain boundary

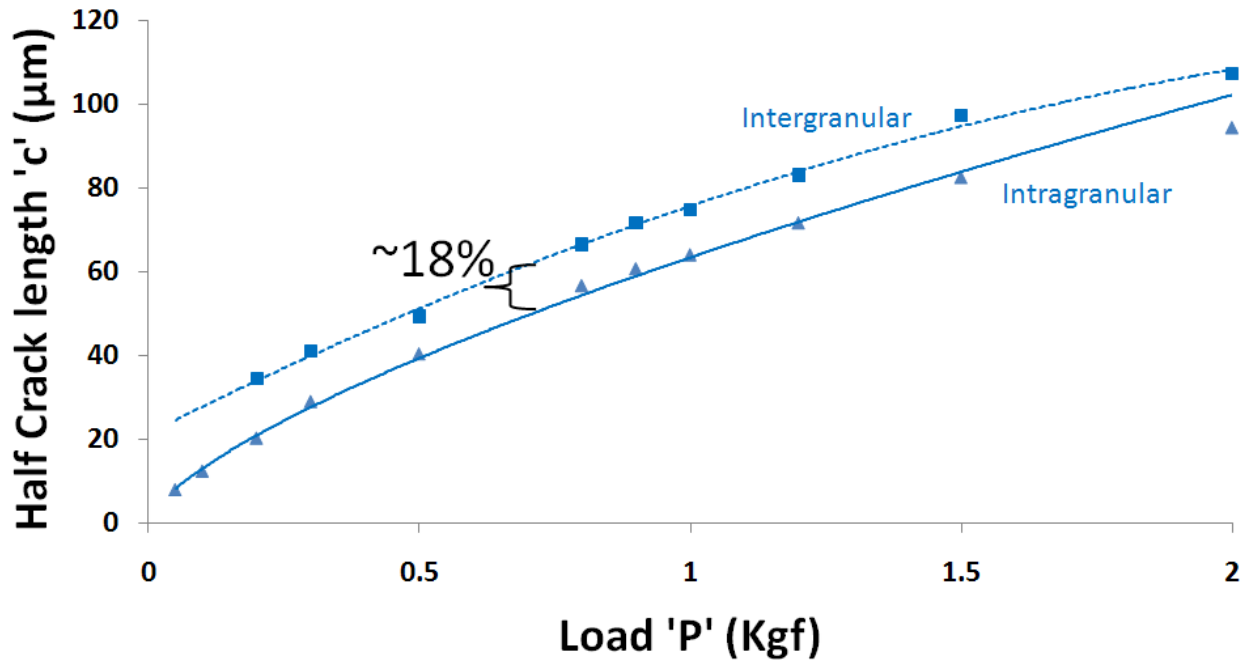


Figure 3-13. Plot of half crack length 'c' versus load 'P' for static indentations revealing a relationship of the type $c \propto P^{2/3}$ for both inter and intragranular cracks

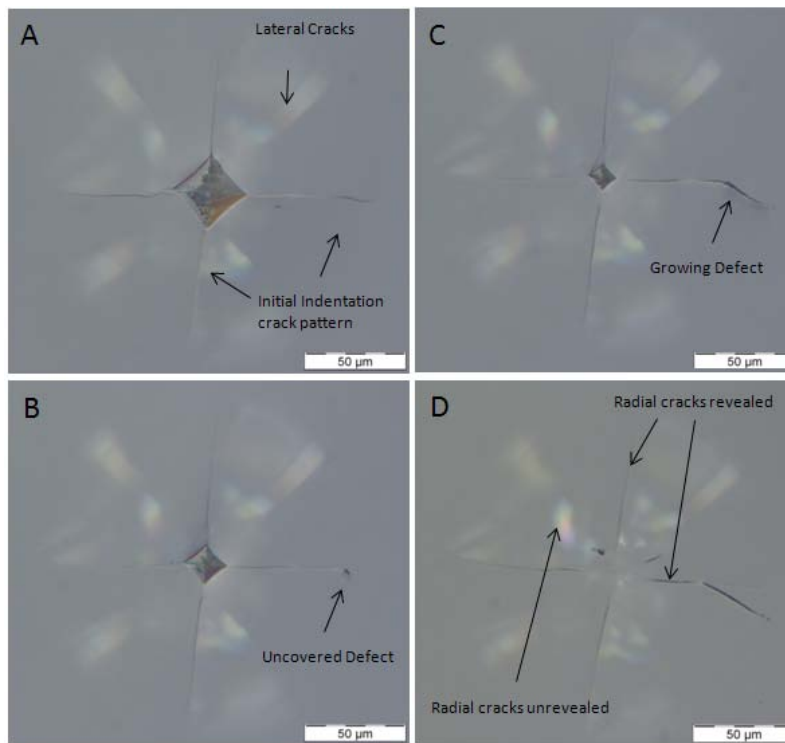


Figure 3-14. Optical images of induced indentation crack patterns after successive polishing steps revealing radial cracks

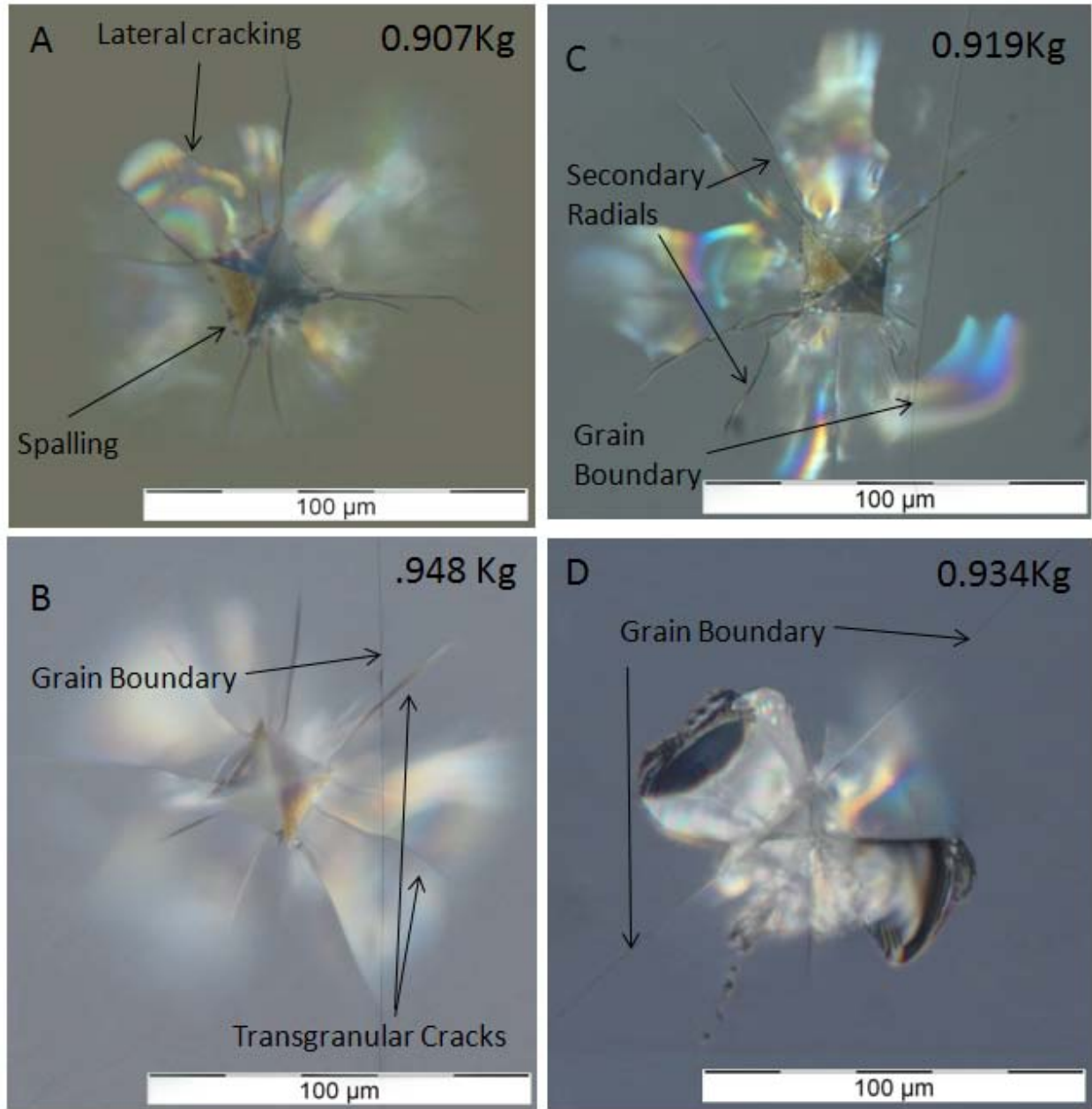


Figure 3-15. Optical images of induced crack patterns due to dynamic indentations on spinel. in A) interior of the grain, B) and C) in the vicinity of a grain boundary and D) along the grain boundary

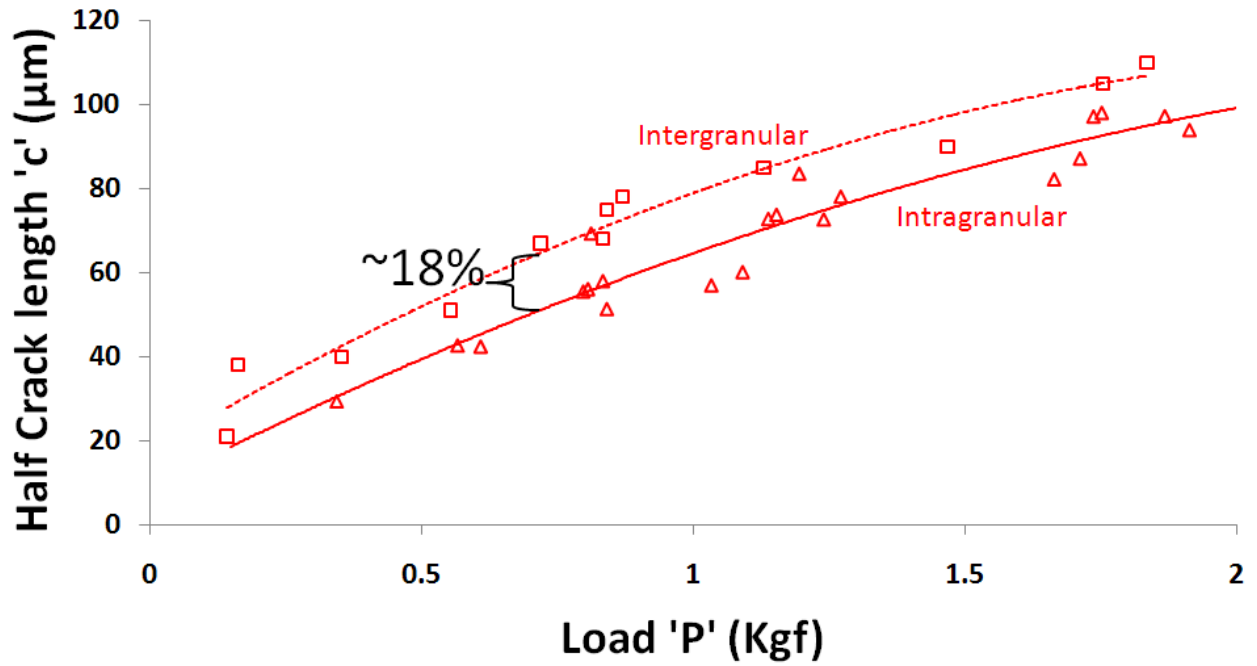


Figure 3-16. Plot of half crack length 'c' versus load 'P' for dynamic indentations revealing a relationship of the type $c \propto P^{2/3}$ for both crack types

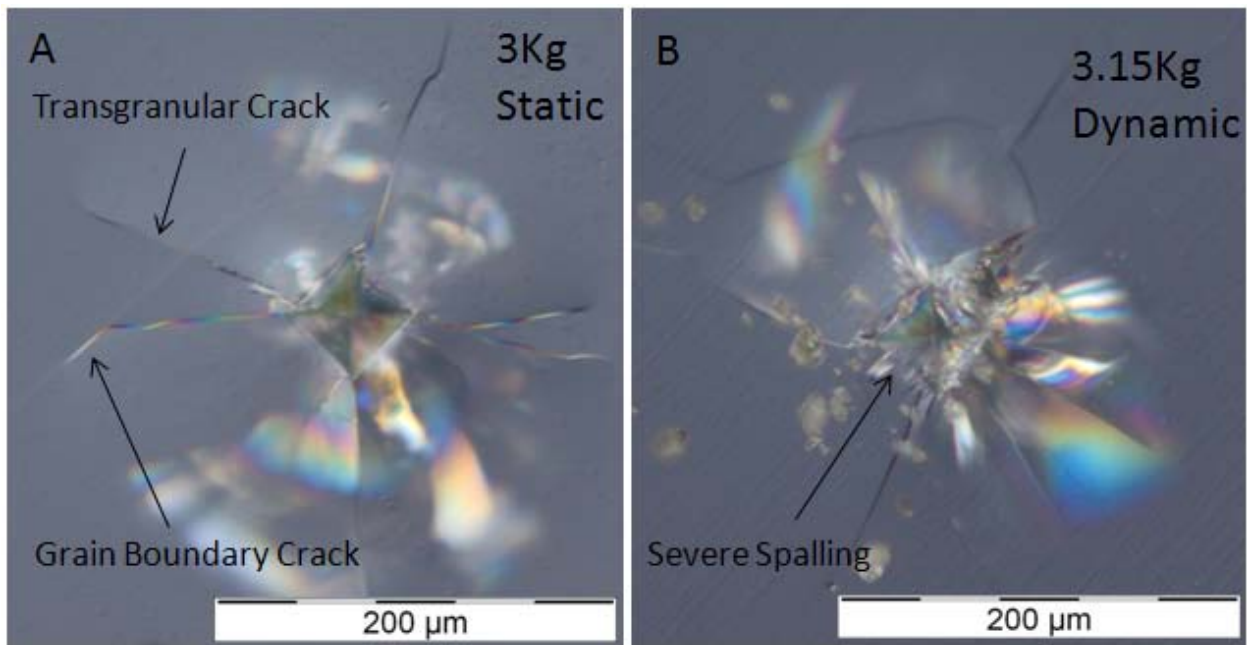


Figure 3-17. Optical images of 3Kg A) static and B) dynamic indentations

CHAPTER 4 CRACK INTERACTION RESPONSE DUE TO SEQUENTIAL INDENTATIONS

Introductory Remarks

Although static and dynamic testing may provide insights into the expected behavior during single-impact events, it is understood that further knowledge of a material's response to multiple and sequentially occurring damage events is paramount. Damage events such as high-velocity impact (e.g. ballistic impact), low to mid velocity impact (e.g. rock or bird strikes) and particle impact erosion (e.g. sand blast, rain erosion) commonly occur in sequences rather than as single events. As such an understanding of the mechanics during these sequential damage events is essential for development of guidelines for multiple-hit resistance [32, 139] and erosion damage testing of transparent materials [140].

Multiple-hit resistance refers to the capability of a material to withstand multiple ballistic impacts, whereas solid and liquid particle erosion resistance is a measure of the expected damage due to high-speed impacts of sand or rain particles. These two measures of resistance are the principal requirements for transparent armor materials, which are prone to loss of transparency upon impact due to extensive damage. Assessment of the "multi-hit capability" of armor materials has generally required precise placement of multiple projectiles onto a test specimen using live fire techniques [141, 142]. Testing of liquid and solid impact erosion has been accomplished using whirling arm [143], single and multiple impact jets [144], and pressurized sandblast methods [145]. The growing importance of testing rock strike damage is demonstrated by a recent issue by the US Army of a tender for rock strike testing of transparent armor systems [146, 147], where it was specified that 24 ceramic ball impacts must be placed

on 6 in. square coupons of various transparent materials. In each case the testing measures are both difficult and expensive. Additionally, these types of tests typically have not focused on the mechanics of failure but rather the symptoms and thresholds of failure.

Easier and less expensive techniques are continually sought to provide insight into the fundamental mechanics of failure during these events. Several studies utilizing different static indentation techniques have been conducted to assess plasticity, deformation and fracture behaviors on various sapphire orientations [45-48, 51, 130-133, 148]. Notable contributions include Hockey [131], who performed Vickers indentation tests on *r*- and *m*-plane sapphire and noticed the appearance of basal and rhombohedral microtwins as well as evidence of activation of several slip systems. Chan and Lawn [133] performed indentations on *a*-plane sapphire and reported evidence of rhombohedral twinning and pyramidal slip, while Kollenberg [132] reported basal twins during indentation of *m*-plane sapphire. Nowak et al. [45-48] performed several indentations on *c*-, *a*- and *m*-plane sapphire, leading to the development of an effective resolved shear stress (ERSS) model predicting the arrangement of surface features around indentation sites. More recent work on *c*- and *m*-plane [148] as well as *a*-plane [51] sapphire has provided considerable insight into the expected surface features and fracture patterns surrounding indentation sites. Perhaps the most comprehensive study on indentation plasticity of sapphire was conducted by Tymiak and Gerberich [49], who developed a resolved shear stress (RSS) model predicting the onset of plasticity and the expected surface feature orientations due to indentation on *a*-, *c*-, *m*- and *r*-plane sapphire. Although these techniques have provided valuable

information regarding the onset of plasticity, anticipated deformation systems, resultant surface feature orientations and incipient fracture patterns, they do not take into account strain-rate effects.

Studies utilizing flyer plate [69, 70, 149] and dynamic indentation techniques [48, 56] have begun to reveal the characteristic behavior of sapphire during dynamic events. While these efforts are instrumental in understanding the strain rate sensitivity of sapphire, none of these techniques provide an assessment of sapphire fracture during sequential damage events. To this end, closely spaced sequential indentations can be a useful technique to develop an understanding of damage zone interaction. Sequential indentation techniques have been successfully conducted to unearth fundamental modes of fragmentation and the interactive nature of neighboring damage zones in several glasses and ceramics [150-154].

Investigation of damage evolution due to sequential indentations on sapphire is of particular interest due to the highly anisotropic and complex rhombohedral–hexagonal crystal structure of this material. Single-crystal sapphire has been shown to develop unique and intricate indentation fracture patterns that are uncharacteristic of glasses and other transparent polycrystalline ceramics [135]. For example, in a typical glass or transparent ceramic, cracks generally appear along the corners of a Vickers indentation [155] due to stress concentration caused by the sharp indenter geometry [156]. In the case of single-crystal sapphire, Vickers indentation does not induce cracks along these corners but rather along well-defined crystallographic orientations irrespective of Vickers orientation. This type of crystal orientation dependence of crack systems has been reported in other studies of single-crystal materials [157]. Additionally, it has been

shown that some crack orientation correlates well with previous predictions of surface traces of twinning [49]. A typical *a*-plane indentation has been shown to produce three distinct sets of surface features and incipient cracks (Figure 4-1A). The first set consists of a series of opposing cracks oriented perpendicular to the *c*-axis. This surface feature is referred to by the authors as “B-cracks” due to their orientation parallel to the (0001) basal plane. The second and third set of cracks have been named “R1-cracks” and “R2-cracks” due to their orientation parallel to the rhombohedral (0112) and (1102) planes, respectively. Also indicated in Figure 4-1A is a reference polar coordinate system with its *c*-axis at $\theta = 0^\circ$ and its max is at $\theta = 90^\circ$. This nomenclature will be used later when discussing crack interaction during sequential indentations at various orientations.

Although the patterns of these surface features have been well documented in the literature, to this authors’ knowledge, none of these studies have revealed their interactive behavior due to sequential indentations and the complex three-dimensionality associated with these crack orientations within the crystal structure. Such an understanding is vital to unraveling the fundamental damage mechanisms associated with development of fracture and fragmentation modes characteristic of sapphire under multi-hit and erosion damage conditions. Due to the complex crystal structure of sapphire, it is crucial to understand the crack plane orientation with respect to the crystal planes. Figure 4-1B illustrates three-dimensional orientations of various crack systems with respect to the *a*-plane of the sapphire crystal. The relative orientations of the crystallographic planes are shown in Figure 4-1C. While the B and the R2 cracks grow perpendicular to the *a*-plane, the R1 cracks propagate along a plane inclined at 43° relative to the *a*-plane. This is due to the oblique orientation of the (0112)

r-plane relative to the *a*-plane (1102) surface. It is this inclination of R1 as well as its interaction with the other two crack systems which play a crucial role in fragmentation of sapphire under multiple indentations as described in the following sections.

The objective of Chapter 4 is to assess the interaction behavior of cracks on the *a*-plane of sapphire when two Vickers indents are placed in close proximity at various orientations. More specifically, the sensitivities and modes of crack interactions to various spatial alignments of the Vickers indentations are investigated. In addition, the source of a newly discovered bulk material separation mechanism due to the interaction of two sequential indentation damage sites on *a*-plane sapphire is also presented. For the purposes of completeness the findings of crack interactivity will be compared to similar sequential indentation patterns on magnesium spinel.

Experimental Methods

Square tiles of dimensions 76.2 mm x 76.2 mm x 7.62 mm of edge-defined film-fed growth (EFG) *a*-plane sapphire were obtained from Saint Gobain Crystals, Milford, NH. First, a series of single Vickers indentations is placed on the *a*-plane of the tile using a Wilson®109 Instruments Tukon® 2100B indenter. A 900g load was chosen for all indentations as this was found to be just sufficient to activate all relevant crack systems without excessive lateral cracking and significant distortion of surrounding areas as such damage limits visual observation of cracks under an optical microscope. The indenter diagonals for all indentations were oriented along the *m*- and *c*-axes and ample spacing between each indentation was allowed in order to insure that no interaction between initial indentations would occur. After the initial indentations were placed, the resulting crack lengths were measured and photographed. A series of secondary

indentations at the same load and Vickers axes orientation were then placed at predetermined distances from each initial indentation at varied angular orientations.

The spatial relations of the sequential indentations were varied in terms of both radial separation distance (r) and angular position (h) from a fixed geometric axis (i.e. polar coordinates) as indicated in Figure 4-1A. As a convention, the reference axis is chosen to be the c -axis (i.e. $\theta = 0^\circ$). The separation distance (r) between two sequential indents was measured from the center of the first indent to the center of the neighboring indent. The separation distance (r) of the second indentation at which the cracks induced by the first indentation either extend or deflect from their original direction was considered to be the start of interaction and defined as the 'interaction limit' (I_L). The distance between the first and second indentations that resulted in joining of the cracks is defined as the "unification limit" (U_L). Due to limitations of equipment it was found to be extremely difficult to accurately and repeatedly place indentations at angle increments of less than 45° . Although it is expected due to crystal symmetry conditions that test orientations of $\theta = 0^\circ, 45^\circ, 90^\circ$ and 135° would produce equivalent results to that of $\theta = 180^\circ, 225^\circ, 270^\circ$ and 315° , respectively, all orientations were tested to confirm this and to generate more data for statistical significance. Hence, the aforementioned procedure was repeated at selected angles of $0^\circ, 45^\circ, 90^\circ, 135^\circ, 180^\circ, 225^\circ, 270^\circ$ and 315° from the m -axis.

Results

Fracture Plane Geometry

The intensity of cracking and the mode of crack interactions on a -plane sapphire were found to be highly sensitive to the spatial relation of the sequential indentations

relative to the orientation of the crystal axes. Furthermore, it was found that crack appearance and interaction sensitivities were unaffected by varying the orientation of the Vickers diagonals relative to the crystal axes. This is because the crack systems have been shown to propagate along preferred crystal planes [49, 51] irrespective of the relative orientation of indentation diagonals, i.e. cracks do not initiate from indentation corners as in typical isotropic polycrystalline brittle materials [150, 151], but rather follow crystallographic planes. It needs to be recognized that any two crack systems (among B, R1 and R2) emerging from the two sequential indentations can interact during the experiments depending on their spatial orientation with respect to each other. Due to symmetry considerations, analysis of the crack plane interactions can be simplified into half indentation models. Recall that due to crystallographic symmetry, analysis of 0° , 45° , 90° and 135° orientations is equivalent to the 180° , 225° , 270° and 315° orientations, respectively. Hence, analysis of the first four orientations will be presented in detail, but the data generated in all the above orientations will be plotted while defining the limits of interaction and unification. The interaction of various crack planes can be readily observed by the diffused light in the enclosed regions by the cracks when viewed under an optical microscope at high magnification.

Figure 4-2A illustrates the interaction of cracks when the second indentation is performed at $\theta = 0^\circ$ (along the *c*-axis) with respect to the first indentation. This orientation leads to an intersection of the R1 and R2 cracks from each indentation. The appearance of a color change between the R1 and R2 surface cracks is due to subsurface light reflection captured by the optical microscope, providing evidence of crack surface formation beneath the original surface at an angle that is not

perpendicular to the viewing axis. As will be seen in the subsequent discussions, unlike the interaction of cracks at other orientations, a unique material removal mechanism can be identified in this specific orientation. Due to their relative orientation and the divergent nature, the R1 and R2 cracks intersect, forming a large fragment in the shape of an inverted triangular prism, as schematically illustrated by the cross-hatched surfaces in Figure 4-2B. This fragment was observed to eventually separate entirely from the parent material as indentations were made in closer proximity in this orientation. This mode of bulk material separation has never previously been reported in the literature.

Crack interaction at the 45° orientation is shown in Figure 4-3. Compared to the previous case of $\theta = 0^\circ$, the intensity of crack interaction at this orientation is significantly less severe at equivalent radial separation distances. Thus the separation distance between the indentations must be significantly reduced so as to induce crack interactions. The effect of separation distance will be discussed in a separate section below. As the second indentation is made closer to the first, the R2 cracks start to get closer but they do not influence each other immediately. Rather, they tend to demonstrate a “pass-by” behavior, and follow their original crystallographic planes without sensing the presence of the other as illustrated in Figure 4-3B. This behavior can also be confirmed by the lack of discoloration (no diffused light) between the two cracks. Eventually, when the distances between the two indents are sufficiently close, the applied stress field is sufficient to bridge the two R2 cracks. Thus, there is significantly lower sensitivity to crack interaction in this orientation compared to the 0° orientation. This “pass-by” behavior is schematically depicted in Figure 4-3C.

Indentations aligned along the c -axis (90° orientation) again result in significantly reduced interaction sensitivity. The crack interaction limits in this configuration are dictated primarily by the interaction of basal (B) cracks as shown in Figure 4-4. The cracks that propagate along the rhombohedral planes (R1 and R2) do not intersect in the same manner as the 0° orientation due to the divergent angle of the R1 cracks beneath the surface as depicted schematically in Figure 4-4B. The lack of crack intersection does not allow for bulk material separation as in the 0° orientation. Thus the interaction limit is dictated rather by the interaction of the shorter basal plane (B) cracks.

Finally, the crack interactions due to sequential indentations along the 135° orientation are shown in Figure 4-5. This orientation presents a surface crack pattern that is very similar to the 45° orientation—only a subtle difference is evident. The “pass-by” behavior is evident at the surface but a discoloration between the cracks provides evidence that subsurface crack interaction does occur (Figure 4-5B). This is rationalized by the fact that the R1 crack planes are inclined towards each other rather than parallel to each other as in the previous case of the R2 plane interaction in the 45° orientation shown in Figure 4-3. This relative orientation of crack planes leads to a subsurface intersection as graphically depicted in Figure 4-5C. This yields a slightly higher crack interaction sensitivity than the 45° orientation.

Crack Interaction Sensitivity

Clearly, the interaction sensitivity is highly dependent on the separation distance and spatial orientation of the second indentation with respect to the first indentation. Indentations along the c -axis (i.e. $\theta = 0^\circ$) result in the greatest crack interaction sensitivity (i.e. cracks start to interact at the farthest distance compared to any other

orientation), and the cracks along the 45° orientations reveal the lowest sensitivity. Although only selected micrographs that reveal the fundamental modes of crack interactions are shown in Figures 4-2 to 4-5, numerous indentations at various distances in each orientation were conducted. Moreover, only the crack interaction modes between $\theta = 0^\circ$ and $\theta = 135^\circ$ were discussed previously although numerous indentations at $\theta = 180\text{--}270^\circ$ were also performed for completeness. However, due to symmetry, the interaction modes are the same and are not discussed further for the latter set of angles. The crack interaction sensitivity in terms of the distance at which two cracks interact, modes of interaction (i.e. extension, deflections and unification), and the type of crack systems that interact at various relative orientations are summarized as a function of angular position in Figure 4-6. The green diamond data points identify individual test conditions where no visibly apparent crack interactions were noted. The yellow circle data points identify tests which resulted in crack extension or deflection. Finally the red triangle data points indicate tests that resulted in complete unification of crack systems. Data located at 360° is identical to that of 0° and is repeated in Figure 4-6 for completeness.

The plot indicates a twofold symmetric pattern in which the greatest crack interaction sensitivity (i.e. the farthest distance between the two indents where the cracks begin to interact) is seen when the second indentation is located along the *c*-axis in relation to the first indentation (i.e. 0° or 180° orientation), while the sensitivity is significantly lower in all other orientations. All orientations except for indentations placed along the *m*-axis (i.e. 90° or 270° orientation) resulted in interactions of the rhombohedral (R1 and R2) crack systems, whereas the indentations along the *m*-axis

(90° and 270°) orientation caused interaction of the basal plane (B) cracks at significantly smaller distances. The specific crack system(s) that interacted for each tested orientation is also provided in Figure 4-6.

Based on the above discussions and the results presented in Figure 4-6, two limits of crack interaction are defined: the “interaction limit”, I_L , and the “unification limit”, U_L . The “interaction limit” is defined as the maximum separation distance between the two indents where the first indentation cracks are affected by the appearance of the second indentation cracks and respond either by further growth (i.e. cracks lengthen) or change in direction (cracks deflect) and is represented as a dotted blue line. All indentations separated by distances above this limit would be expected to produce no crack interaction with the preexisting cracks due to the first indentation at that orientation. On the other hand, the “unification limit” is defined as the maximum radial distance between the two indents where the indentation cracks are first witnessed to coalesce, and is represented by a solid red line in Figure 4-6. Not all indentations above this limit would result in complete crack unification. Due to variability in the behavior at equivalent orientations, the individual data points are not exactly symmetric around 180°; however, due to the symmetry known to exist, the I_L and U_L curves are presented as limits with symmetry around 180°. As such, the I_L and U_L curves in Figure 4-6 are drawn as per the maximum separation distance which resulted in crack unification or interaction that was witnessed within each set of equivalent orientations (e.g. $\theta = 0^\circ$ and $\theta = 180^\circ$).

The results of this analysis can be used in the design of impact-resistant transparent armor materials as well as for setting guidelines for the multi-hit resistance of sapphire. Unlike other transparent isotropic armor materials, the multi-hit resistance

of sapphire single crystal is expected to vary depending on the placement of the second shot relative to the first and the crystallographic orientation of the armor surface. Two consecutive impacts on *a*-plane sapphire along the *c*-axis ($\theta = 0^\circ$ or 180°) would be expected to yield a significantly larger damage zone for a given shot placement separation as compared to sequential impacts in any other orientation. A comprehensive understanding of the sensitivity to neighboring cracks and the severity of crack interactions allows one to take advantage of the crystallographic orientations while designing transparent armor materials for specific threats. The results also offer insights into the micromechanics that occur during the erosion process. Damage severity and rate of accumulation of damage can be estimated based on the size of impact media and the areal density of impacts. The fundamental mechanics responsible for visibility loss due to rock strikes can also be rationalized based on the insight gained from the type of investigation and results presented in this paper.

Crack Interaction in Spinel

In order to fairly compare the nature and extent of crack interactivity between sapphire and spinel sequential indentations on spinel were made following the same patterns described in the previous sections. As expected the crack patterns were not influenced by crystal axes orientation as evident in the sapphire testing. Figure 4-7 depicts sequential indentations made on spinel at various orientations. Clearly evident is that no orientation results in a visibly weakened zone as evident in indentations on *a*-plane sapphire. Also evident is the appearance of a “protective” behavior of the grain boundaries. Instead of complete unification of cracks from adjacent indentations, the cracks easily deflect along grain boundaries and often move away from each other. This is an important mechanism that promotes the continuance of structural integrity.

Closing Remarks

A multiple static indentation technique was employed to derive indentation crack interaction sensitivities on the *a*-plane of sapphire. Sequential indentations on *a*-plane sapphire revealed a crack interaction sensitivity that is highly dependent on the spatial orientation as well as on the separation distance between the indentations. The highest crack interaction sensitivity occurs when the indentations are placed along the *c*-axis. This placement also results in the intersection of R1 and R2 crack planes, resulting in a unique bulk material separation mode. This behavior is not evident when indentations are placed along the *m*-axis (90° orientation) due to the divergent angles of the crack planes. The interaction of the shorter basal plane (B) cracks set the interaction limit in the 90° orientation, resulting in significantly lower interaction sensitivity. The 45° orientation resulted in a sensitivity to crack interaction that is similar to the 90° orientation with the interaction limit set by interaction of the R2 rhombohedral cracks. The reduction in sensitivity in this orientation is explained by a pass-by behavior between the parallel R2 rhombohedral crack planes. The 135° orientation had slightly increased sensitivity compared to the 45° and 90° orientations. This was explained on the basis of subsurface interaction of R1 crack planes which are favorably inclined towards each other. Based on a large number of sequential indentations at various separation distances, two terms were defined to describe interaction behavior. The maximum radial distance where the initial indentation cracks are affected by the presence of the nearby crack (through crack lengthening or crack deflection) defines the interaction limit, I_L . The maximum radial distance where the indentation cracks first coalesce defines the unification limit, U_L . The understanding developed here can be

used to take advantage of these crack sensitivities to design or to set guidelines for multi-hit resistance in sapphire windows.

The resultant crack interactivity of sapphire was much less sensitive to crystal axes orientation. The appearance of a weakened zone seen clearly in sapphire was not evident in spinel. Additionally, the grain boundaries seem to offer an element of deterrence from crack coalescence promoting greater structural cohesiveness.

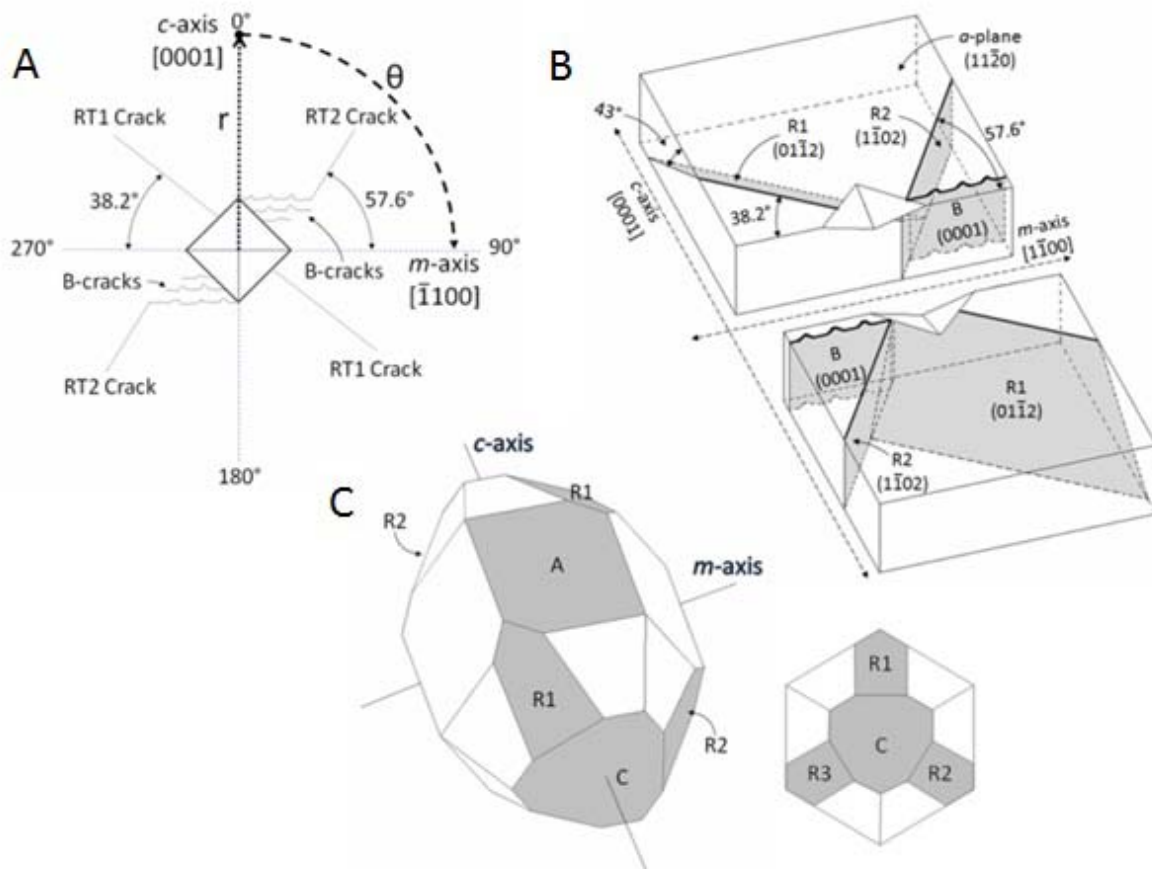


Figure 4-1. Schematics depicting sapphire crack plane geometry. Schematics include A) surface crack patterns due to a Vickers indentation on a-plane sapphire; B) crack plane orientations with respect to the a-plane; and C) sapphire crystal geometry showing the relevant nomenclature of the crystal planes.

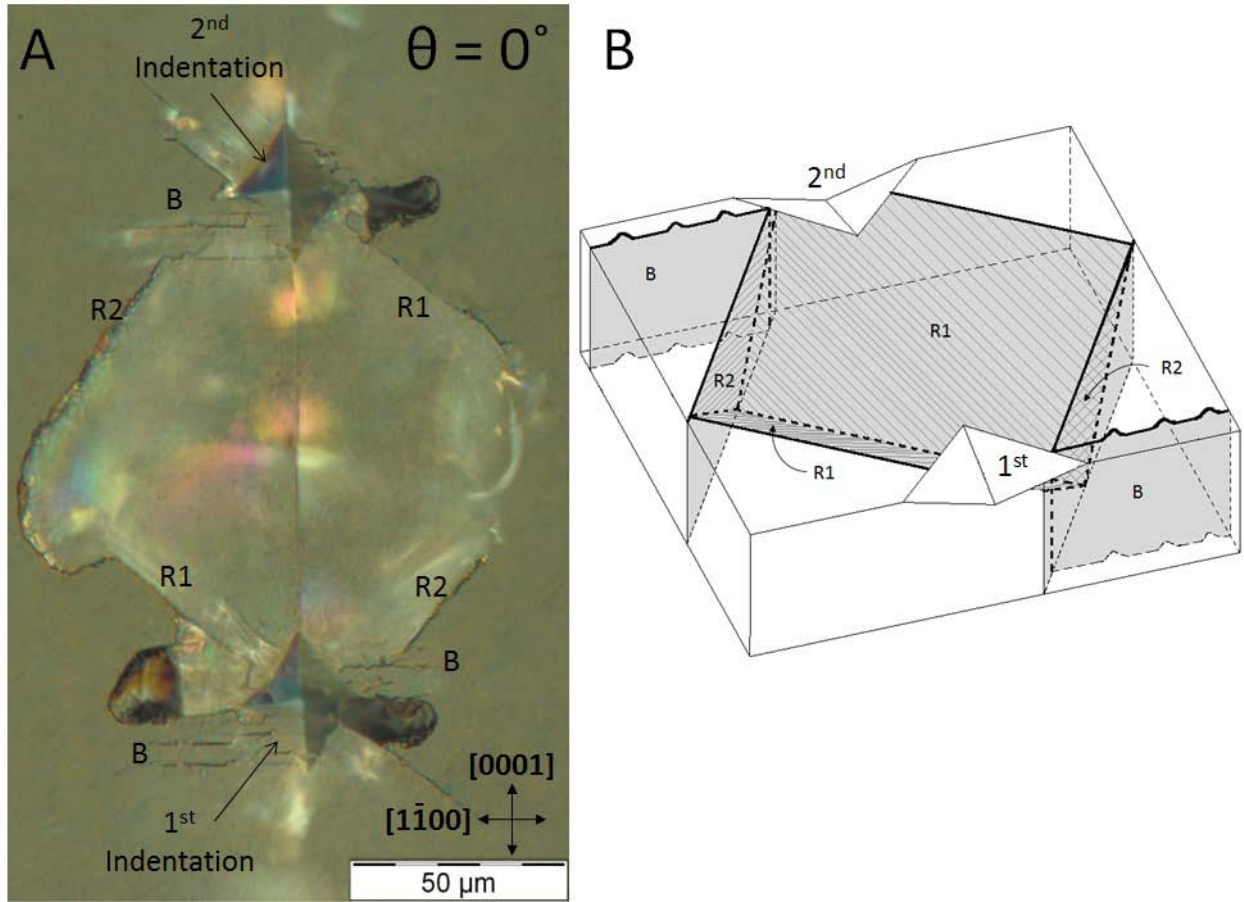


Figure 4-2. A) Optical image and B) schematic of cracks induced by the sequential indentations along the 0° orientation.

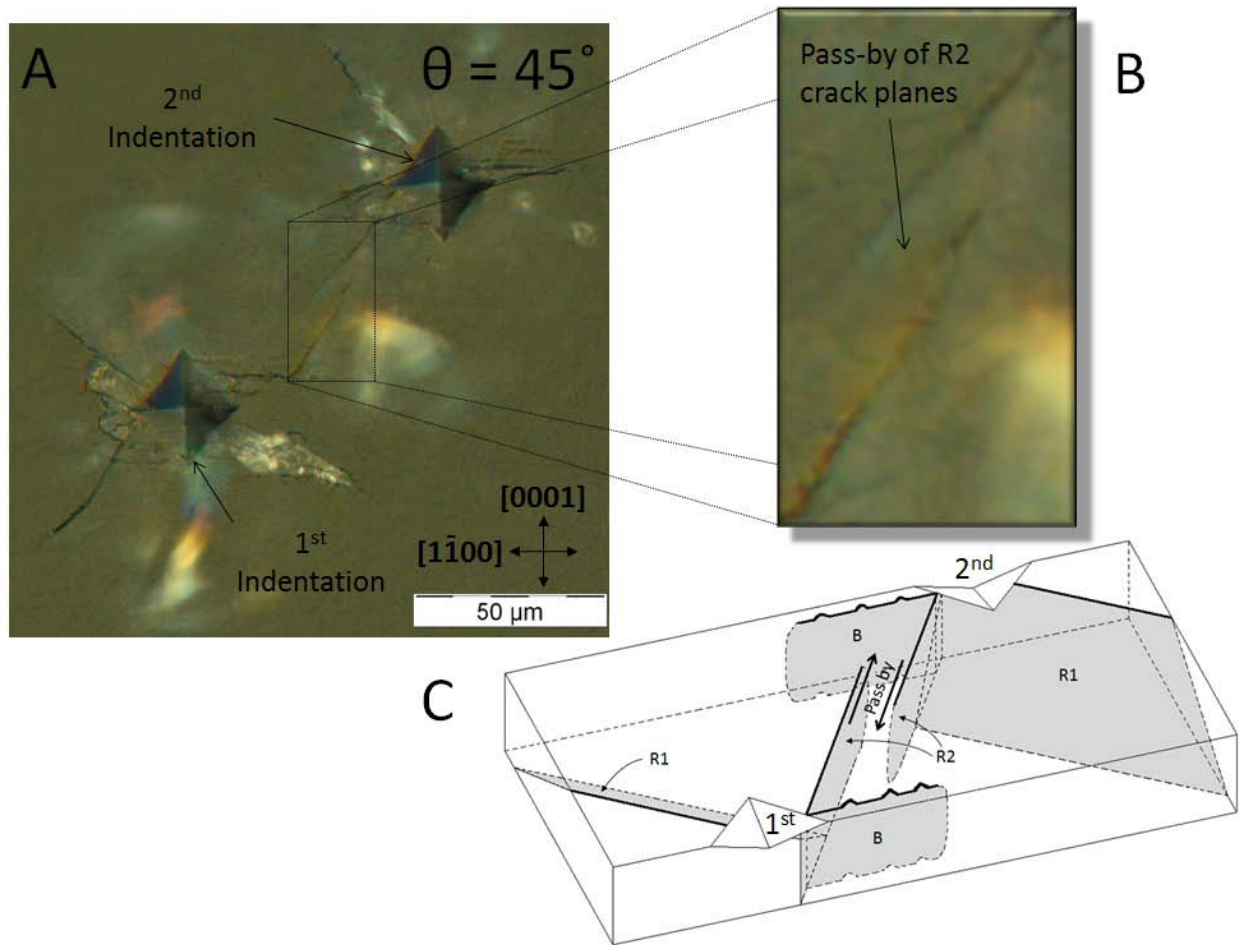


Figure 4-3. Optical images and schematic of the cracks induced by the sequential indentations along the 45° orientation. Images include A) an image of the overall indentation site, B) a magnified image of the region near the crack tip and C) schematic illustrating the “pass-by” behavior of two R2 cracks along their parallel crystallographic planes.

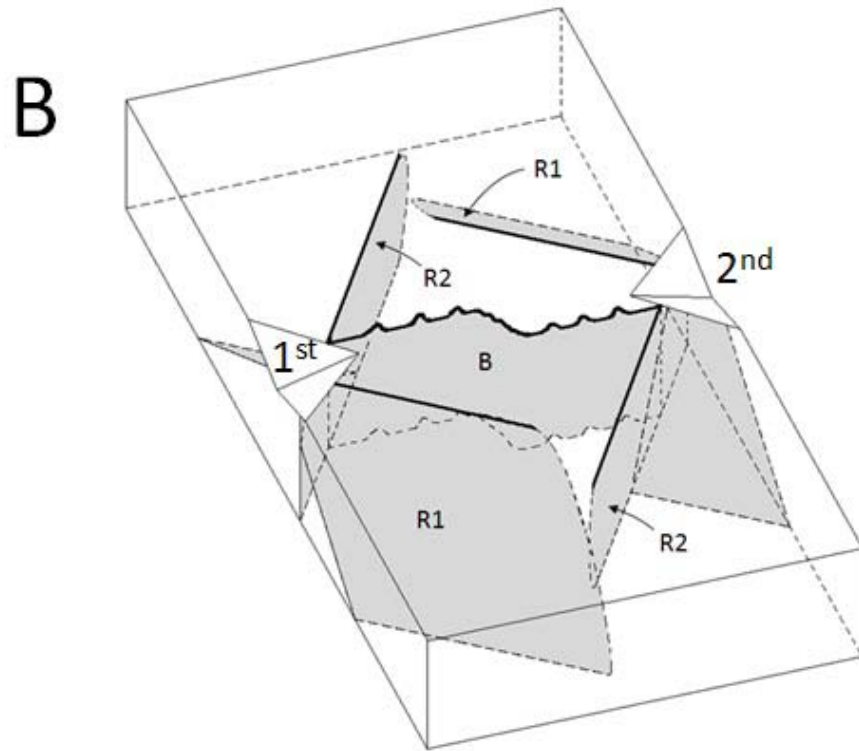
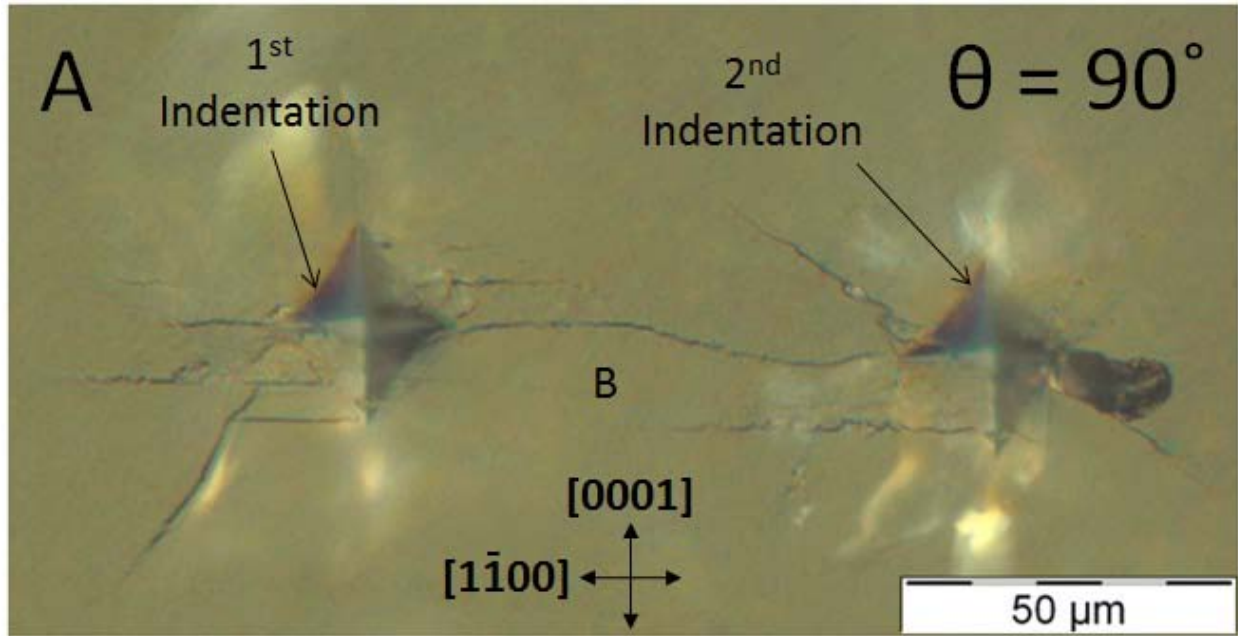


Figure 4-4. A) Optical images and B) schematic of the cracks induced by the sequential indentations along the 90° orientation.

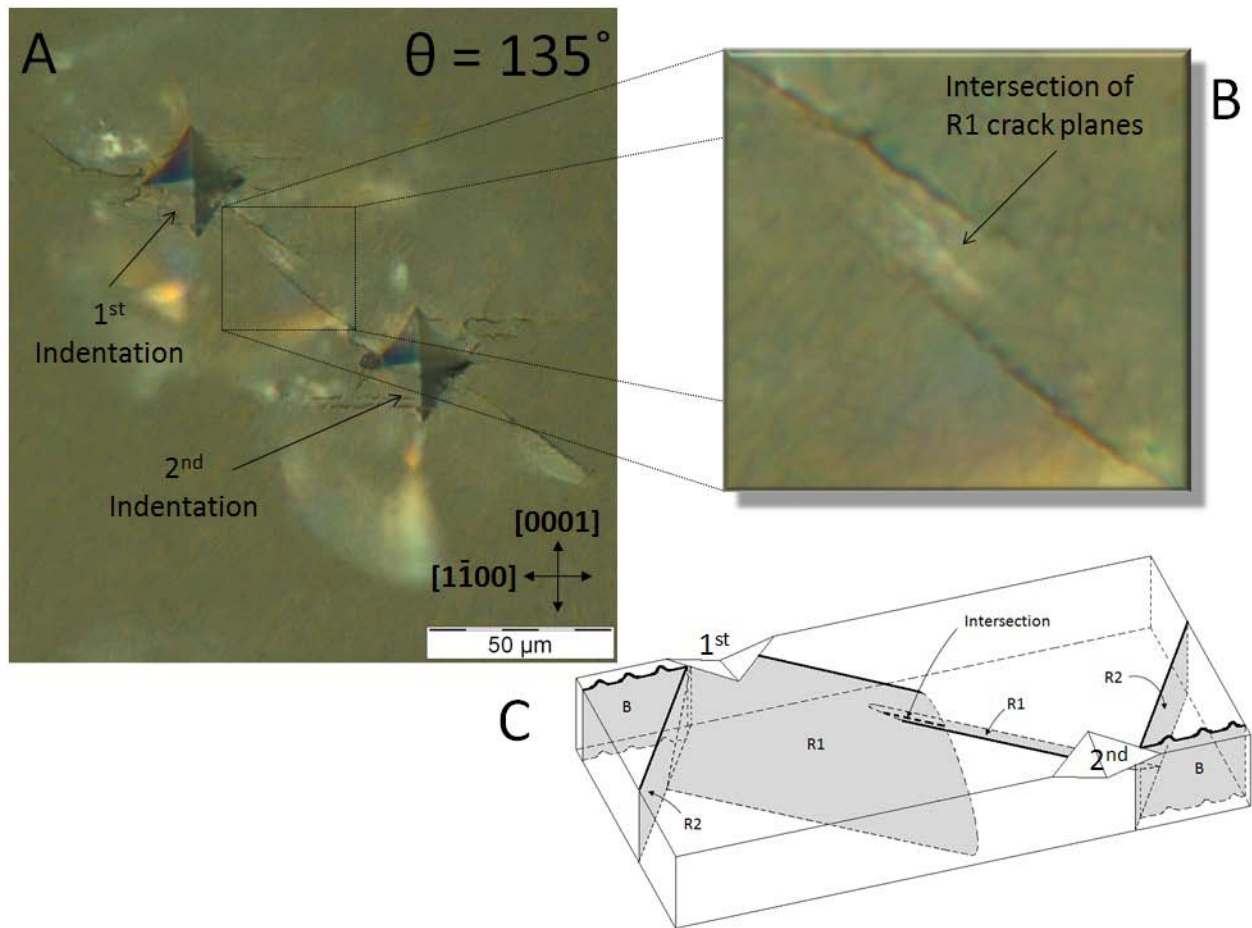


Figure 4-5. Optical image and schematic of cracks induced by the sequential indentations along the 135° orientation. Images include A) an optical image of the overall indentation site, B) a magnified image of R1 crack tips revealing potential interaction beneath the surface and C) schematic illustrating the crack interaction mode due to R1 crack plane interactions.

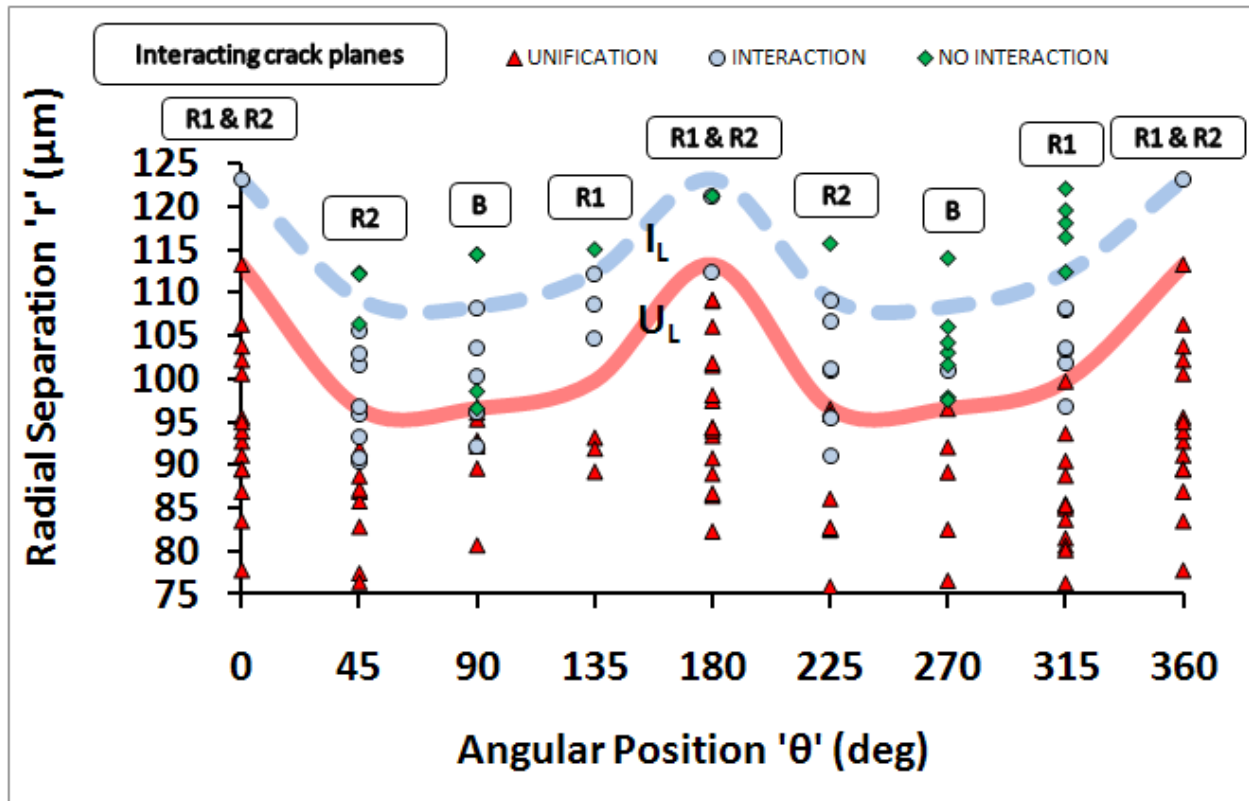


Figure 4-6. Experimental data revealing damage sensitivity of *a*-plane sapphire due to sequential indentations at various orientations and radial separations. The “interaction limit” (where cracks during sequential indentations tend to deflect or extend) and “unification limit”(where surface cracks merge) as well as the crack planes that interact are indicated.

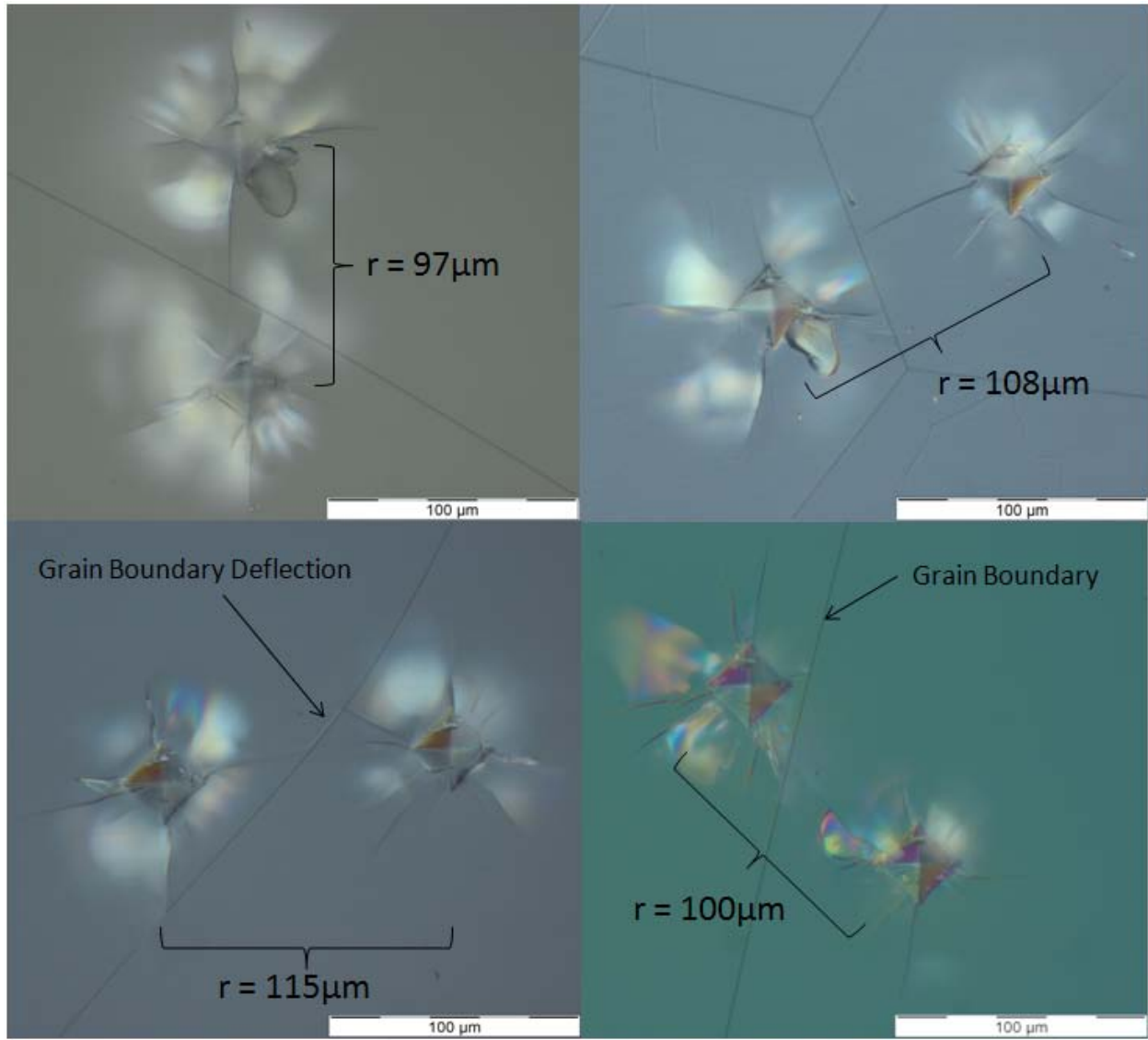


Figure 4-7. Optical image of cracks induced by the sequential indentations on spinel at various orientations.

CHAPTER 5 BALL IMPACT RESPONSE

Introductory Remarks

Understanding the fundamental behavior of ceramic materials during ballistic impact events is central to the efficient design of armor systems. Currently, the most accepted methods used to assess the ballistic performance of materials involve full scale ballistic impacts using live fire tests [31, 32, 139]. Several tests including the V_{50} and depth of penetration (DOP) tests have been developed expressly for this purpose [158, 159]. A good summary of ballistic test methods is presented by Normandia and Gooch [160]. Full scale tests, however effective, are expensive and difficult. As a result scaled down test methods are continually sought in order to assess ballistic performances of materials. Since ballistic impact is inherently a highly dynamic event, simple tests which assess static material properties such as static indentation and static bending do not provide adequate insight into the true material behaviors during impact. Other dynamic tests such as flyer plate, split-Hopkinson's pressure bar (SHPB) and dynamic indentation methods provide a look at the strain rate sensitivity of various materials yet they do not provide a conclusive look at the damage morphology germane to the understanding of ballistic resistance. Planar impact experiments using long rod penetrators have also been devised [161, 162]. While these tests provide critical insight into ceramic behavior they are not suited to provide damage evolution during and after impact due to the configuration of the test plates.

Edge-on-Impact (EOI) tests coupled with high speed photography techniques, on the other hand, have been shown to provide insight into damage phenomenology. In this method a projectile, usually a planar cylindrical rod impacts the edge of a target. A

high speed camera positioned orthogonal to the impact plane then captures the damage evolution.

The origin of EOI testing can be traced back to a German researcher, Schardin, who conducted similar tests in the 1930's on glass [163]. Schardin later founded the Ernst Mach Institute (EMI) where several materials have been analyzed using this technique. To date, varieties of glasses, glass ceramics and ceramics have been analyzed using this technique [164-181]. Other than an investigation on sapphire by Senf and Winkler [168] and aluminum oxynitride (ALON) by Straßburger et al. [177-181], this technique has not been utilized on advanced transparent ceramics. As newer transparent ceramics are developed, this technique can prove to be a useful test in generating a knowledge-base on damage evolution during impact events.

While some significant efforts have been made to characterize the strain rate sensitivity of magnesium spinel, published efforts characterizing the damage evolution during impact are still unavailable. The intent of Chapter 5 is to report the results of EOI tests on coarse grained magnesium spinel and a prism plane sapphire rods utilizing steel alloy balls as projectiles. The damage front evolution upon impact is captured using high speed digital camera while further insight into fracture behavior will be provided by post mortem analysis of recovered fragments for each material investigated. Finally, energy balance equations are used to account for the fractional energy absorbed by various deformation and fracture modes during ball impact based on the observed phenomena.

Experimental Methods

Magnesium spinel rods (12.5mm x 12.5mm x 76mm) were supplied by Technology Assessment and Transfer, Annapolis, MD. The material was supplied in a polished

condition requiring no further surface preparation. The spinel rods were confirmed to have the same grain size (~250 μm) as the samples described in Chapter 3. Sapphire rods (16.7mm x 7.62mm x 76.2mm) were cut from tiles supplied by Saint Gobain Crystals, Milford, NH. Assessment of the damage phenomenology of the tiles impacted on the a -plane is ultimately the objective but bars of sufficient length could not be cut with the impact axis oriented along the a -axis. As such the bars were cut such that the impact axis is the m -axis. The m -axis results should provide some look at the behavior of sapphire impacted on a prism plane.

Edge-On-Impact (EOI) tests were conducted using a pneumatic pressure gun able to launch foam sabots preloaded with 4.76mm (.1875 inch) diameter S2 steel alloy balls. A slight variation to the original EOI test is evident in that the use of a spherical ball yields a Hertzian contact rather than a planar impact. Once launched from the pressure gun, the loaded sabot flight is obstructed by a rigid steel block. A clearance hole in the block allows the ball to separate from the sabot and propel toward the test sample at approximately 280 m/s. The impact event and ensuing damage evolution is recorded at 250,000 frames per second using a high speed camera (Vision Research® Phantom v710®). The full test assembly is schematically depicted in Figure 5-1. Post mortem analysis of the fragments and projectile were conducted using a high magnification optical microscope in order to identify the level and type of damage. Two separate impact tests were conducted on each material in order to verify the repeatability and consistency of the observed phenomena.

Results

Impact Damage Evolution

The damage evolution for each material was distinctly different in appearance. This is not surprising given the prominent differences between the materials. Sequences of photographs capture a time scale history of damage evolution upon impact.

Figure 5-2 shows a sequence of photographs taken during initial impact of a steel alloy ball onto a spinel bar. Time 'T=0' is taken as the last frame before initial impact and is approximated to be 2 μs before impact. Each successive frame then represents 4 μs of elapsed time. The speed of the ball directly preceding impact was calculated by tracking the motion of the ball (i.e. distance and time between two successive frames) and determined to be approximately 280 m/s. Immediately upon impact the ball is observed to dwell at the contact surface for 15-20 μs . For the first 8 μs of the dwell period the ball center approaches the impact surface presumably creating the comminuted zone of material. From 8 to ~20 μs the ball remains stationary at the impact surface while fragments are witnessed to be ejected from the impact site at a velocity approaching 235 m/s. Also witnessed during the initial moments of impact is a rapidly expanding damage front propagating from the impact surface traveling at approximately the shear wave speed of spinel (5620 m/s [103]).

During the dwell phase it is conjectured that severe plastic deformation and erosion of the projectile (ball) occurs. Figure 5-3 provides high resolution pictures of the recovered ball. Figure 5-3A shows the ball with the fragments in place while Figure 5-3B shows the fragments apart. Depicted in Figure 5-3A is a circular contact surface with a measured contact radius 'a' of 1.71 mm. Figure 5-3C reveals the contact surface

under high magnification. Evident from this image is the presence of pits and fissures as well as partially embedded spinel fragments that are magnitudes of scale smaller than the grain size of the spinel material. These features confirm the creation of a comminuted zone consisting of sub grain size fragments. The presence of these fissures verifies that significant erosion of the ball by the comminuted material is occurring during the dwell period. Beyond the dwell period and timed with the reflected tensile wave, the ball elastically unloads and is deflected backward in two fragments at an approximate rebound velocity of 45 m/s.

As mentioned briefly above, a rapidly expanding network of fractures originating from the impact site are seen to propagate into the spinel rod. In Figure 5-2, two distinct damage zones can be seen to emerge from the impact site. The first zone, or zone 1, extends from the impact surface into the material approximately 18 mm. Analysis of recovered fragments from zone 1 confirms that the majority of damage is mixed mode (transgranular and intergranular) fracture with the average recovered fragment size approximately half that of the average grain size of this spinel sample. Examples of the fracture surfaces created in zone 1 are shown in Figures 5-4A and B. Eventual complete dissociation of the grain network in zone 1 is observed as the entire damage zone dilates in all directions after impact. The second zone, or zone 2, extends an additional 18mm into the material beyond zone 1. The fracture mode in this zone shifts from transgranular to predominantly intergranular cracking and retains its structural cohesion. An example of the intergranular cracking typical of zone 2 is shown in Figure 5-4C while the surface between zone 1 and zone 2 is shown in Figure 5-4C where a mixed mode fracture shown to dominate. The transition from zone 1 and zone 2 is

taken as the point where dilation of the spinel bar is zero indicating the point where structural cohesion is maintained. The depth of zone 1 is also evidenced by a slight color contrast from zone 2. Zone 1 is visibly brighter perhaps due to a greater amount of reflected light due to dilation occurring as a consequence of extensive cracking. To better illustrate the different damage zones and their locations relative to the impact site a magnified image is provided in Figure 5-5A. The ejecta emanating from beneath the ball as well as significant dilation of zone 1 are clearly evident. The comminuted zone immediately ahead of the ball is not to be confused with zone 1. Although zone 1 is shown to contain predominately transgranular fracture, the comminuted zone is an area of material pulverization and fragmentation. As such, Figure 5-5B is provided as a schematic showing the locations of each separate damage zone. The energy dissipation associated with the creation of these zones as well as other energy dissipation mechanisms will be discussed in the next section. It is acknowledged that the relative size of each zone is likely to be impact velocity dependant. However, due to the limited number of test samples available, experiments at varied impact speed could not be performed. Future tests could confirm the relation of the size of each zone to impact speed.

The rate of damage front evolution upon impact is shown in terms of the depth of penetration of the damage front 'S' as a function of time 't' is plotted in Figure 5-6A. Overlaid on the same plot is the estimated damage velocity ' V_D '. The velocity is estimated by measured damage front movement over successive segments of time. It is evident from this plot that the damage velocity V_D varies as the damage front propagates into the material. The damage front initiates a high velocity close to 5700

m/s but rapidly falls to 3200 m/s and remains at that level for another 3 μ s. The damage front then linearly decays to zero approximately 11 μ s after impact. The first abrupt velocity shift occurs at the time that the damage front reaches the limit of zone 1 and transitions to zone 2. The damage velocity of zone 1 (5700 m/s) correlates well with the reported shear wave velocity of spinel (5620 m/s) [103] while the damage front velocity of zone 2 slows to approximately 60% of the shear wave velocity. This observed behavior can be rationalized as further evidence of a shift from transgranular to intergranular fracture from zone 1 to zone 2 as described in the following.

In order to simplify the network of grains in the material, each individual grain is assumed to take the shape of an equal edge length (l) tetrakaidecahedron (truncated octahedron) with six square and six hexagonal faces. A schematic of this shape is shown in Figure 5-6B. Although in reality the grain structure contains a distribution of complex polyhedral, this simplified shape has been used previously to simulate grain structure [182, 183]. Analyzing the proposed shape, Mendelson [182] discovered that the distance across flats ' D ' was approximately equal to three times the edge length ' l '. The transgranular fracture path is assumed to travel the cross section of each of these tetrakaidecahedron grains (distance D) depicted by the short dashed arrow in Figure 5-6C. It is proposed that as the crack mode shifts to intergranular fracture, the crack path alters its course and follows along the grain boundary (assumed to be the half perimeter of a grain) depicted by the long dashed arrow in Figure 5-6C. Since the half perimeter length of the octagon is roughly 1.57 D or ~60% longer than the cross sectional distance it is logical that the damage front velocity would reduce proportionally concurrent with the shift to intergranular fracture. Thus, during the early phase of impact where the ball

velocity is high, the available energy is quickly dissipated by creation of extensive fragmentation (or pulverization) in the form of transgranular fracture. This forms zone 1 as described earlier. Once the available energy is diminished to below certain level, intergranular fracture dominates as it is the preferred mode of cracking in spinel. Furthermore the abrupt transition in damage velocity in Figure 5-6A can be rationalized as an indication of a shift occurring from transgranular to intergranular fracture. This would signify that the energy imparted onto the material has declined to a level insufficient to create transgranular fractures yet still high enough to continue creating intergranular fractures. This transition of damage mode is consistent with the fracture patterns observed during indentation discussed in Chapter 3. When indentations were performed close to the grain boundary, the crack prefers to travel along the grain boundary rather than the grain interior. However, when the energy imparted is high enough as in the case of dynamic indentations (or static indentations at large loads), even an indentation placed close to the grain boundary causes both intergranular and transgranular cracking. Thus there is a direct correlation to the fracture patterns observed during the indentation and impact experiments. Once the energy level diminished below a critical level a visible damage front ceases to advance. Yet the stress wave continues to travel to the end of the rod and reflect back as a tensile wave. Because ceramics are weaker in tension than in compression, tensile cracking perpendicular to the tensile wave are witnessed.

The impact response of *m*-axis sapphire is distinctly different than that of spinel. Due to the single crystal structure of sapphire, grain boundaries do not exist and hence all fracture occurring is intragranular. Similar to the fracture response due to single and

sequential indentations (Chapters 3 and 4), which has been shown to be heavily influenced by crystal orientation, the fracture response of sapphire due to impact is equally dependant on crystal orientation. This leads to the development of distinct crystallographically oriented fracture planes as the damage front propagates into the target.

Figure 5-7 shows a sequence of photographs taken during initial impact of a steel alloy ball onto a *m*-axis sapphire bar. Time 'T=0' is taken as the last frame before initial impact and is approximated to be 1 μ s before impact. Each successive frame then represents 3.56 μ s of elapsed time. The speed of the ball directly preceding impact was calculated by tracking the motion of the ball (i.e. distance and time between two successive frames) and determined to be approximately 268 m/s. Immediately upon impact the ball is observed to dwell at the contact surface. For the first 7 μ s following impact the ball center approaches the impact. The ball remains intact and stationary at the impact surface for up to ~18 μ s until a ball fragment is noticed to be ejected at approximately 105m/s. Timed with the ejected ball fragment the ball is witnessed to drop vertically at the impact plane with no appreciable rebound velocity. Figure 5-8 provides a high resolution picture of the recovered ball. Notice in Figure 5-8 is a circular contact surface with a measured contact radius 'a' of 1.34 mm. It is interesting to note that the ball contact surface lacks the same amount of pits and fissures that were clearly present on the recovered ball from spinel impact tests. This could be explained by the lack of ejecta surrounding the ball during impact which was a distinctly different response than that seen during impact on spinel. This combined evidence would

suggest that the same amount of erosion between the ball and the target is not occurring during sapphire impacts as that of spinel.

As mentioned the crack response in sapphire due to impact seems to follow known crystallographic planes. Immediately upon impact a zone of microcracking can be witnessed expanding from the impact plane at approximately the shear wave speed of sapphire. At first look, the crack formation seems to be forming cone cracks which have been widely reported to occur during impact onto ceramic. However with closer inspection, the cracks follow angles that are consistent with the orientation of R1 and R2 cracks reported to exist during indentation of *a*-plane sapphire and discussed in Chapter 3. Also noticed is the emergence of a crack propagating outward away from the impact site and orthogonal to the impact plane. This crack system is consistent in orientation with the reported B-cracks from the Chapters 3 and 4. While the B-crack continues to propagate orthogonal to the impact plane for nearly 14 μ s, the R1 and R2 cracks form a criss-cross pattern of intersecting cracks. After this time the B-crack transitions to an R2 crack which was consistent with earlier findings of crack transition in indentation of sapphire presented in Chapter 3. It is also evident that while the R2 crack plane is orthogonal to the viewing plane resulting in a relatively thin crack feature the R1 crack is seen as a wide band. This is due to the fact that the R2 crack plane is inclined 43° to the viewing plane consistent with the indentation behaviors discussed in Chapters 3 and 4. Another consistency with the findings of indentation experiments on sapphire is the indication of heavy damage accumulating between the R1 and R2 cracks only when aligned along the *c*-axis. This was explained to occur due to the divergent R1 and R2 crack planes. This unique crack behavior supports the observations of increased

damage along the *c*-axis for sequential indentations described in Chapter 4. This oriented damage results in a sequence of equally spaced *c*-axis aligned damage bands that contain higher levels of damage with areas of less damage oriented between the damage bands. A high magnification image depicting the oriented damage bands is provided in Figure 5-9A while a schematic depicting the criss-crossing R1 and R2 cracks is given in Figure 5-9B. The area containing the first two damage bands is found to dilate similar to the reported zone 1 in spinel. Rather than fracturing and discharging in micron sized grain fragments as was evident with spinel, the sapphire fragments were one the order of several millimeters in size. Figure 5-10 shows the recovered sapphire rod illustrating the size of ejected fragments. This size discrepancy would indicate that the amount of cracking per unit volume of material is lower with sapphire than spinel resulting in less fracture energy dissipation during impact events. During later stages of impact response the orthogonally extended B-crack effectively splits the spinel bar in two halves. These halves are found to separate at approximately 600 μ s after impact resulting in a larger amount of material separation from the parent material. Whereas the spinel sample retained structural cohesion beyond 18mm from the impact site, sapphire retained cohesion only beginning at 34 mm from the impact site. This could lead to an understanding as to the rationale for improved second hit performance of spinel.

The depth of penetration of the damage front '*S*' as a function of time '*t*' is plotted for the sapphire impact in Figure 5-11. Overlaid on the same plot is the estimated damage velocity '*V_D*' for sapphire. The velocity is estimated by measured damage front movement over successive segments of time. It is evident from this plot that the

damage velocity V_D varies as the damage front propagates into the material. The damage front initiates a high velocity close to 6950 m/s but rapidly falls to 2500 m/s and remains at that level for another 12 μ s. The damage front then linearly decays to zero approximately 20 μ s after impact. The initial damage velocity (6950 m/s) correlates well with the reported shear wave velocity of sapphire (7000 m/s) [184]. The reduced damage velocity is consistent with earlier reports of EOI experiments on sapphire by Senf and Winkler [168]. While they reported similar damage front velocities, they provided no explanation as to the origin of the reduced velocity. It is postulated that the reduced velocity is resultant to cracks propagating along the angled rhombohedral planes rather than perpendicular to the impact plane thereby significantly slowing the damage front motion.

Once the energy level diminished below a critical level a visible damage front ceases to advance. Yet the stress wave continues to travel to the end of the rod and reflect back as a tensile wave. Because sapphire like many ceramic is weaker in tension than in compression, additional R1 and R2 cracks are seen to develop due to the reflected tensile wave.

Impact Energy Balance

Another step at characterizing the behavior of these materials during dynamic impact is to estimate the energy dissipated through each mechanism discussed so far. Upon impact of the ball on to the test samples, the kinetic energy (KE) of the ball is proportioned between the target and the ball. The energy imparted onto each body is both elastic and inelastic. Elastic wave energy (U_{EW}) is proportioned through the propagation of pressure or longitudinal waves, shear waves and surface or Rayleigh waves [185]. Work of fracture (WOF) is a major component of inelastic energy

dissipation that occurs as new fracture surfaces are created by either intergranular or transgranular fracture modes as well as spalling/fragmentation/comminution [116, 186]. Energy dissipation due to kinetic energy of the debris fragments (U_{KE-F}) also occurs as the fragments are dislodged and ejected upon impact. Frictional energy (U_{FE}) is also considered as fragments of the target come in contact with and pass by the ball during impact. Energy is also dissipated through deformation and fracture of the ball i.e. work of deformation of the ball (WOD_B) as well as the kinetic energy of the ball (U_{KE-B}) as it is deflected away from the impact surface.

Thus, an energy balance equation is proposed as,

$$KE_I = U_{EW} + WOF + U_{KE-F} + U_{KE-B} + WOD_B + U_{FE} , \quad (8)$$

where KE_I is the kinetic energy of the ball immediately preceding impact. Other energy loss mechanisms such as sound and heat energy are considered negligible and will not be considered. All material properties for both materials and the ball that were used in the following calculations are provided in Table 5-1.

For both impact tests (spinel and sapphire) the speed of the ball was estimated by motion tracking of the ball over successive frames. In the case of the spinel impact test the speed was estimated to be ~280 m/s delivering an estimated 17.4 J of impact energy, while the sapphire impact ball speed was estimated at 268 m/s delivering 15.9 J of impact energy. The fractional energy absorbed in the form of elastic waves is given by the following equation presented by Reed [187]:

$$\lambda = 7.267 \frac{\delta}{\rho_2 C_0^3} (1 - \nu_2) \left(\frac{1 - \nu_2^2}{1 - 2\nu_2} \right) \rho_1^{-1/5} K^{6/5} \nu^{3/5} \quad (9)$$

where ρ_1 , ν_1 , ρ_2 and ν_2 are the densities and Poisson's ratio of the ball and target respectively, δ is a dimensionless quantity dependant only on Poisson's ratio [188]. C_0

is the longitudinal elastic wave speed in the target and K is a constant given, respectively, by the following equations.

$$C_o = \left(\frac{E_2}{\rho_2} \right)^{0.5} \quad (10)$$

$$K = \frac{4}{3} \left(\frac{1-\nu_1^2}{E_1} - \frac{1-\nu_2^2}{E_2} \right)^{-1} \quad (11)$$

Using published material data for spinel, sapphire and S2 steel alloy (Provided in Table 5-1) the fractional energy due to elastic waves was found to be 0.43 for spinel and 0.36 for sapphire. Multiplying the fractional energy with the impact energy yields an approximation for the energy consumed by elastic wave motion (U_{EW}) of 7.4 J for spinel and 5.7J for sapphire. It is clear that sapphire does not consume as much elastic energy as spinel due to the much higher modulus. The remaining sources of energy dissipation are rationalized to be through kinetic energy associated with penetrator and fragment motion as well as inelastic mechanisms such as fracture surface creation and frictional effects.

The fracture surface energy (γ_f) is directly related to the fracture toughness, Young's modulus and the Poisson's ratio of the material [116] as per,

$$\gamma_f = \frac{K_{IC}^2 (1-\nu^2)}{2E} \quad (12)$$

For spinel we will assume that the zone 1 described above consists of entirely mixed mode fracture where all grains are fractured into halves and all available grain boundaries are fractured, while zone 2 consists of purely intergranular fracture where no grain fracture occurs. This assumption is based on observations of fracture modes

present in recovered fragments in Figure 5-4. As mentioned in the preceding section, a simplification is made by representing the grain structure as a network of equal sized tetrakaidecahedrons rather than complex irregular polyhedrons (Figures 5-6B and 5-6C). The volume (V), surface area (A_s) and cross sectional area (A_c) of the assumed grain shape is given by the following equations [182].

$$V = 8\sqrt{2}\left(\frac{D}{3}\right)^3 \quad (13)$$

$$A_s = (1 + 2\sqrt{3})\left(\frac{D}{3}\right)^2 \quad (14)$$

$$A_c = (1 + \sqrt{2})\left(\frac{D}{3}\right)^2 \quad (15)$$

where D is the average grain size as described in Figures 5-6B and 5-6C.

An approximation for the number of grains contained within each zone is then given by the total estimated volume of each zone divided by the grain volume given in Equation 13. The total intergranular fracture surface area would then be estimated by the surface area of each grain (Equation 14) multiplied by the estimated number of grains in zones 1 and 2 while the total intragranular surface area would be approximated by the average cross sectional area of each grain (Equation 15) multiplied by the number of grains estimated to reside in zone 1.

The assessment of fracture energy for sapphire is distinctly different. Since sapphire is a single crystal all fracture surfaces created are intragranular. However fractures are found to preferentially follow defined crystallographic planes during indentation tests described in Chapter 3. This behavior was also noticed during impact tests on sapphire. Estimating the amount of fracture surface created in the sapphire rod

upon impact was attempted by visually identifying and measuring developed cracks. As described above, three distinct crack systems were seen to develop. A long B-crack parallel to the basal plane extended 24mm from the impact site. Additionally a criss-crossing pattern of rhombohedral (R1 and R2) cracks were witnessed totaling a length of 23.6mm.

Using reported fracture toughness values for sapphire and spinel, (given in Table 5-1) the energy due to intergranular and intragranular fracture surface creation in spinel is found to be 2.8 J (16%) and 0.8 J (5%) respectively. The energy for fracture surface creation in sapphire along specified crystal planes is 0.67J (4%).

During dynamic impact it has been established that a comminuted region consisting of finely fragmented material is created just ahead of the penetrator tip [189]. Furthermore, it has been asserted that the comminuted zone extends from the point of maximum elastic shear stress and grows towards the loaded surface following the deviatoric elastic stress distribution [190, 191]. Applying Hertzian contact mechanics theory [192], the depth of maximum elastic shear stress was estimated to be on the order of 1 mm. The shape of comminuted material zone beneath a ball impact site has been described as a circular or tear-drop shape following the shape of contact stress contours [193-195]. Yet it is observed that the comminuted zone extends to the edges of the contact region allowing material flow. For this reason, the comminuted region is idealized as an elliptical cone originating at the point of maximum shear stress and extending to the contact surface. Thus, the volume of the comminuted region is then given by,

$$V_{COMM} = \left(\frac{\pi d^2 Z_o}{6} \right) \quad (16)$$

where Z_o is the depth of maximum shear stress due to Hertzian contact and is approximated by its relation to the contact radius 'a' by [192],

$$Z_o = 0.78a \quad (17)$$

An assumption for the radius of the contact region 'a' is taken as the radius of the flattened surface of the recovered ball shown in Figure 5-3A for spinel and Figure 5-8 for sapphire. This yields an estimated comminuted material zone volume of 12 mm³ and 9 mm³ for spinel and sapphire respectively.

In order to assess the energy consumed by fracture surface creation within comminuted zones, Grady [186] proposed a fracture surface energy per unit volume (γ_f) due to dynamic fracture given by,

$$\gamma_f = \frac{3K_{IC}^2}{\rho C_o^2 s} \quad (18)$$

where 's' is the average fragment size estimated by the following equation [186].

$$s = 2 \left(\frac{\sqrt{3} K_{IC}}{\rho C_o \dot{\epsilon}} \right)^{2/3} \quad (19)$$

Depending on the strain rates assumed ($\dot{\epsilon}=10^4$ - 10^6 s⁻¹) the fragment sizes will vary. Based on the sizes of erosion pits seen in Figure 5-3A an assumption of fragment size is on the order of 50 μm. However due to the small volume of fully comminuted material that is actually created in spinel the fracture energy due to dynamic fracture and comminution of material is miniscule. Therefore this recognized fragmentation mode is neglected in the following energy balance study. Assuming the same level of

fragmentation of sapphire an equally miniscule amount of energy is estimated to be consumed through comminution of sapphire in the zone below the ball. Sapphire however exhibits highly damaged and fragmented zones due to fracture between the criss-crossing R1 and R2 cracks. These fragmented zones show up as damage bands (Figure 5-9A) with a width of approximately 4mm oriented along the *c*-axis. The formation of the *c*-axis oriented damage zones were described in detail in Chapter 4. Using the measured width of these damage bands and the cross sectional geometry of the sapphire rod a damage volume of 1022 mm³. Assuming the same fragment size as described above and employing equation 18 yields an estimate of the energy due to damage band creation of 1.04 J or 7% fractional energy.

Kinetic energy due to grain ejection and frictional effects associated with the movement of the fragments along the surface of the ball are also modes of energy dissipation associated with the dynamic fragmentation and comminution process that must also be considered. Tracking the motion of comminuted spinel fragments over successive frames yielded an estimated velocity of the ejected fragments of 235 m/s, almost the same as the ball impact velocity!

Using the calculating volume of comminuted material (Equation 16) and multiplying with the density of spinel yields an estimation of the mass of comminuted material. Using the approximations for mass and velocity of the fragments yields a KE of ejected fragments at 1.2 J or nearly a 7% fractional energy.

Sapphire however resulted in a much slower ejection of fragments (~50 m/s). This combined with the smaller comminuted zone estimated above yielded 0.05J of energy

related to the ejecta. This proves to be significantly less of a factor in dissipation of energy than in the case of spinel.

As previously discussed, Figure 5-3C provides conclusive evidence of pitting and erosion mechanisms occurring during the impact event. This erosion can only occur due to extreme frictional contact between the ball and the comminuted materials. Energy associated with friction between the ball and the ejecta is difficult to accurately predict as an estimate of the normal load between the ball and the fragments as well as the relative coefficient of friction would be needed for such an estimate; both of which are unable to be directly measured using this experimental technique. The impact load, however, can be estimated by the mass of the ball multiplied by the observed rate of deceleration.

For the spinel tests it was observed that the ball was decelerated from its velocity just prior to impact of 280 m/s to 0 m/s during the first 8 μ s following impact. This results in a peak normal force (F_N) of 8300N. In the case of the sapphire test, the ball decelerated from 268 m/s to 0 m/s in approximately 5 μ s. This results in an estimated peak normal force (F_N) of 7945N. Although the exact coefficient of friction between steel and spinel or sapphire is unavailable, the sliding coefficient of friction between several ceramics and steel was studied by Miller [196]. In this study most oxide ceramics including alumina yielded a sliding coefficient of friction against steel of 0.1 providing our only reasonable assumption for coefficient of friction between the ball and target materials. Assuming that the material is flowing from the point of greatest stress outward, thus traveling the distance of the contact radius 'a', the energy dissipated due to friction can then be estimated by,

$$FE = \mu F_N a \quad (20)$$

where 'a' is the radius of contact measured from the recovered ball and F_N is the estimated impact load. With these assumptions the energy dissipated by friction between the ball and comminuted spinel fragments is estimated to be 1.5 J or 9% fractional energy. Sapphire resulted in a similar amount of energy dissipated through frictional mechanisms. Using similar calculations the energy due to friction between sapphire fragments and the ball resulted in 1.4 J (9%).

In the case of spinel, the kinetic energy due to the dilation of zone 1 is another possible mechanism for energy dissipation. As shown in Figure 5-5 the outer perimeter of zone 1 visibly dilates upon impact, indicating dissociation and motion of the grain network. Tracking the amount of dilation between successive image frames provides an estimate of the velocity of dilation. The fragments at the impact surface were estimated to be ejected at approximately 25 m/s with a linear decay of velocity to 0 m/s at the boundary between zone 1 and zone 2 also indicated in Figure 5-5. The kinetic energy due to grain ejection is then found according to the following equation.

$$KE_{\text{grain ejection}} = \frac{1}{2} \rho xy \int_0^{0.018} V^2 dz \quad (21)$$

where ρ is the material density (given in Table 5-1), x and y are cross sectional dimensions of the material, z is the depth into zone 1 and V is the velocity of grain ejection approximated by the following linear relation.

$$V = \left(25 - \frac{25}{0.018} z \right) \quad (22)$$

Substituting equation (22) into equation (21) and integrating gives an estimate of the kinetic energy due to dilation of zone 1 of 1.1 J or a fractional energy of 6%.

Sapphire also exhibits a zone ahead of the penetrator that loses structural adhesion. Evidence from the sapphire rod after impact (Figure 5-10) suggests that the zone that loses structural cohesion and is ejected as fragments is two opposing triangular sections. The leg lengths of the triangular zones are measured to be 12mm x 6.8mm. Through motion tracking of the ejected fragments from these zones the velocity of fragment motion is estimated to be 50 m/s. Taking into account the mass of the triangular zones and the velocity of ejection an approximation of the energy dissipated through fragmentation is derived to be 4.3J or 27% of the fractional energy. This seems to be a significant mechanism for energy dissipation. However effective in dissipating energy it leads to massive structural degradation possibly indicating a rationale for reduced multiple hit capacity.

The portion of energy dissipated by the ball is consumed through plastic deformation and fracture processes as well as through the KE associated with the rebound velocity of the ball away from the impact surface. In the case of spinel, the ball rebound velocity was estimated to be 45 m/s corresponding to a KE of 0.6 J (3%). The rebound velocity of the ball due to impact on sapphire was witnessed to be negligible. However a large fragment of nearly a third of the total mass of the ball was seen to be ejected from the ball. This fragment velocity was estimated to be approximately 105 m/s resulting in a kinetic energy of 0.82J (5%). Additionally the energy to deform and ultimately fracture the ball is estimated by the following equations:

$$WOD_{Ball} = F_N \delta \quad (23)$$

$$WOF_{Ball} = \gamma \pi r^2 \quad (24)$$

where F_N is the normal load, γ is the fracture surface energy of steel, r is the ball radius and δ is the approach of the two bodies approximated by the following equation.

$$\delta = r - \sqrt{(r^2 - a^2)} \quad (25)$$

Combining both the plastic and brittle deformation modes provides an estimate for the energy due to deformation and fracture of the ball. The ball deformation energy due to impact on spinel was approximately 1.4 J (8%) while the deformation energy of the ball due to impact on sapphire was 1.2 J (8%). The remaining fractional energy (0.6 J (3 %) and 0.7J (4%) for spinel and sapphire, respectively) is estimated to be consumed by heat generation and other mechanisms that were unaccounted for in this study.

Figure 5-12 illustrates a pie chart with the summary of the contributions of energy dissipation for each mechanism considered in the analysis of spinel while Figure 5-13 depicts the same summary for *m*-axis sapphire. It is interesting to note the much higher influence of intergranular fracture (16%) than that of transgranular fracture (8%) on the dissipation of impact energy as well as the negligible amount of energy consumed in the creation of a comminuted zone directly beneath the indenter. Both the transgranular fracture of zone 1 and the creation of a comminuted region however are critical processes for energy dissipation as it is these mechanisms that allow for dissipation by KE of fragments (7%) and dilation of the grain network (6%). Additionally the creation of comminuted fragments facilitates energy loss through frictional mechanisms (9%).

Closing Remarks

Ball impact tests were conducted on a course grained magnesium spinel rod and an *m*-axis sapphire rod in order to observe fracture morphology following impact. The impact on spinel resulted in the formation of two distinct damage zones beneath the

impact surface. Zone 1 extends from the impact plane into the target a distance of 18mm and consists of mixed mode fracture. Zone 2 extends an additional 18mm into the bar and was found to primarily contain intergranular fractures but remains intact. This shift in fracture mode was also evidenced by a transition in damage velocity during damage penetration. Upon impact the damage initiates at a velocity close to the shear wave velocity of the target material but quickly drops to approximately 60% of the shear wave speed indicating a shift to a longer fracture path consistent with a shift from transgranular to intergranular fracture. The energy consumed by various deformation and fracture mechanisms was calculated to quantify the contributions of each observed mechanism to the dissipation of total impact energy. Elastic wave propagation, fracture surface creation, kinetic energy of ejected fragments as well as frictional effects was shown to be the most dominant mechanisms of energy dissipation. Creation of comminuted material had a marginal direct effect on the dissipation of impact energy through fracture energy, however the kinetic energy associated with ejected fragments and friction between the fragments and the ball were found to be significant dissipation mechanisms.

The impact on sapphire resulted in a network of criss-crossing cracks confirmed to be oriented with the rhombohedral planes. Additionally a long basal plane crack was witnessed to extend perpendicular from the impact site into the rod. The first 22 mm of the sapphire rod lost structural cohesion and fragmented into large chunks while the b-crack split the rod in halves resulting loss of cohesion for 34mm. This level of structural cohesion loss is much more catastrophic than that witness in spinel. Additionally c-axis oriented damage bands were witnessed which was consistent with observations of

crack patterns due to sequential indentations. The damage front velocity witnessed in spinel originated at approximately the shear wave speed of sapphire yet quickly slowed to 35% of the shear wave velocity. The most dominant energy dissipation mechanisms in sapphire are elastic wave propagation and kinetic energy associated with large fragment ejection, friction and fragmentation associated with the damage bands.

Table 5-1. Material properties used for energy calculations

Material	ρ (Kg/m ³)	E (GPa)	K_{IC} (MPa-m ^{1/2})	ν
S2 Steel Alloy	7870	213	50	0.3
Mg-spinel	3580	277	2.0 ^[85]	0.26
<i>m</i> -axis sapphire	3970	386	2.4 ^[106]	0.275

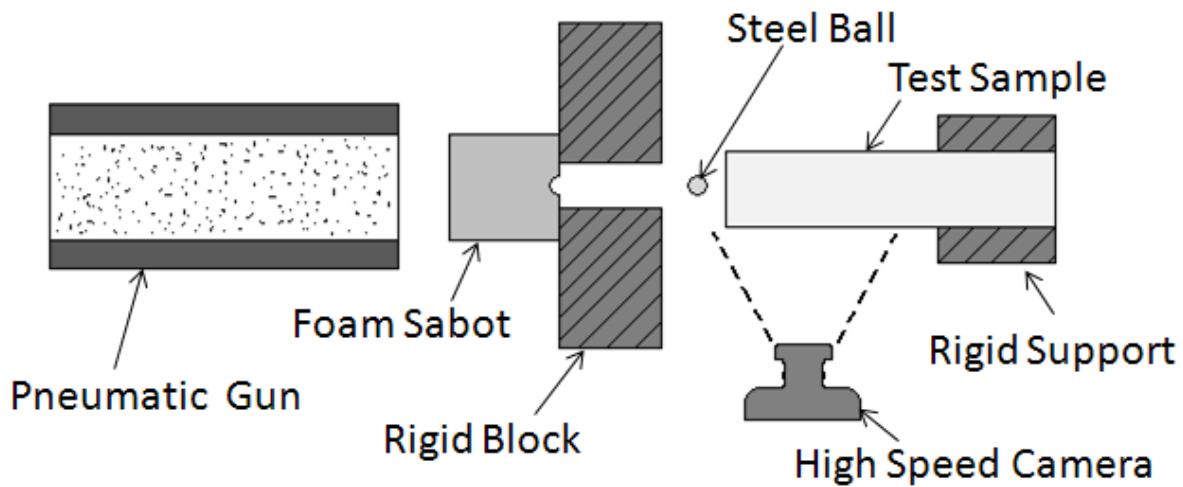


Figure 5-1. Schematic of the Edge-On-Impact test setup.

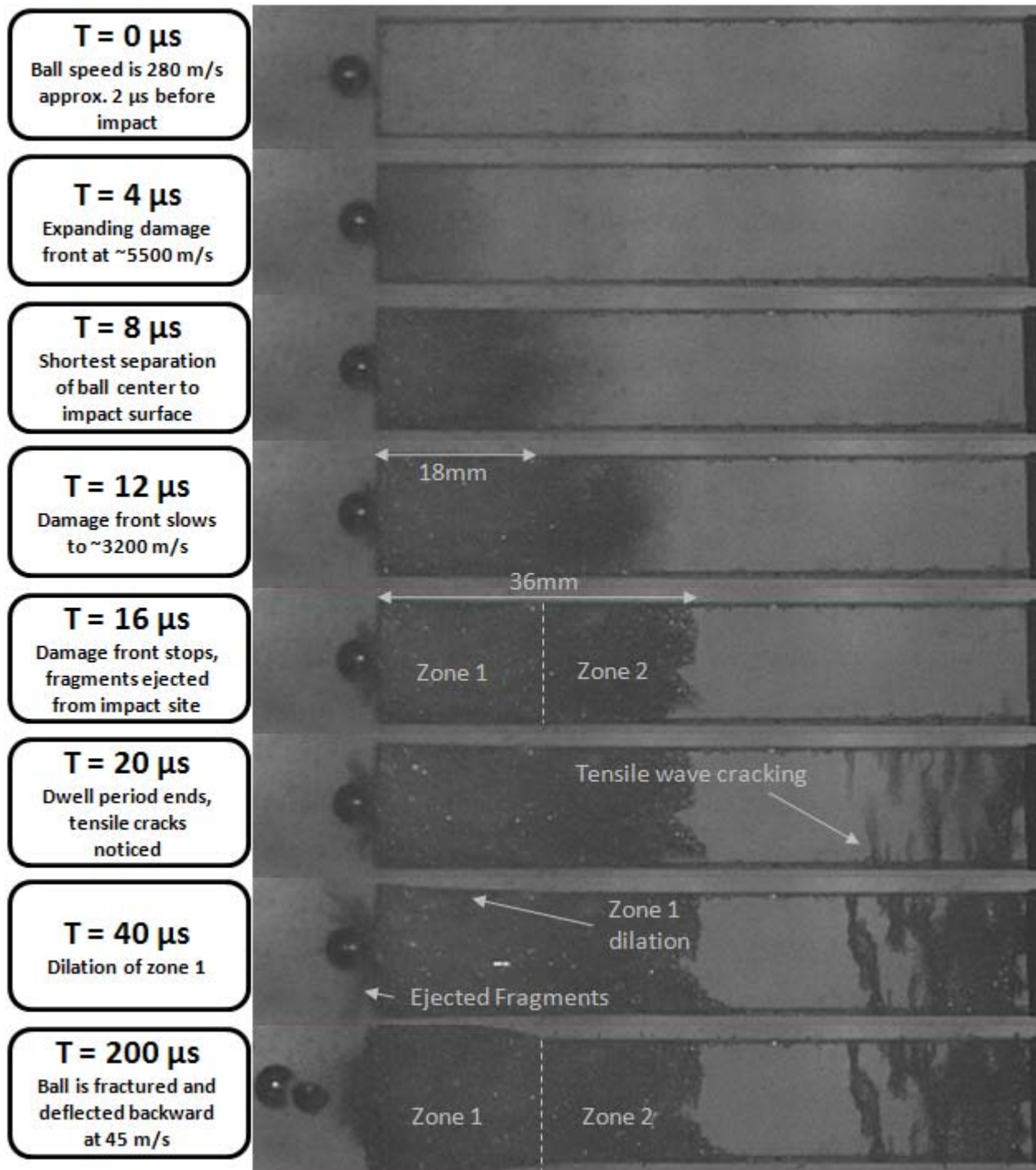


Figure 5-2. Sequence of high speed photographs revealing damage evolution in spinel due to a steel ball impact at 280 m/s.

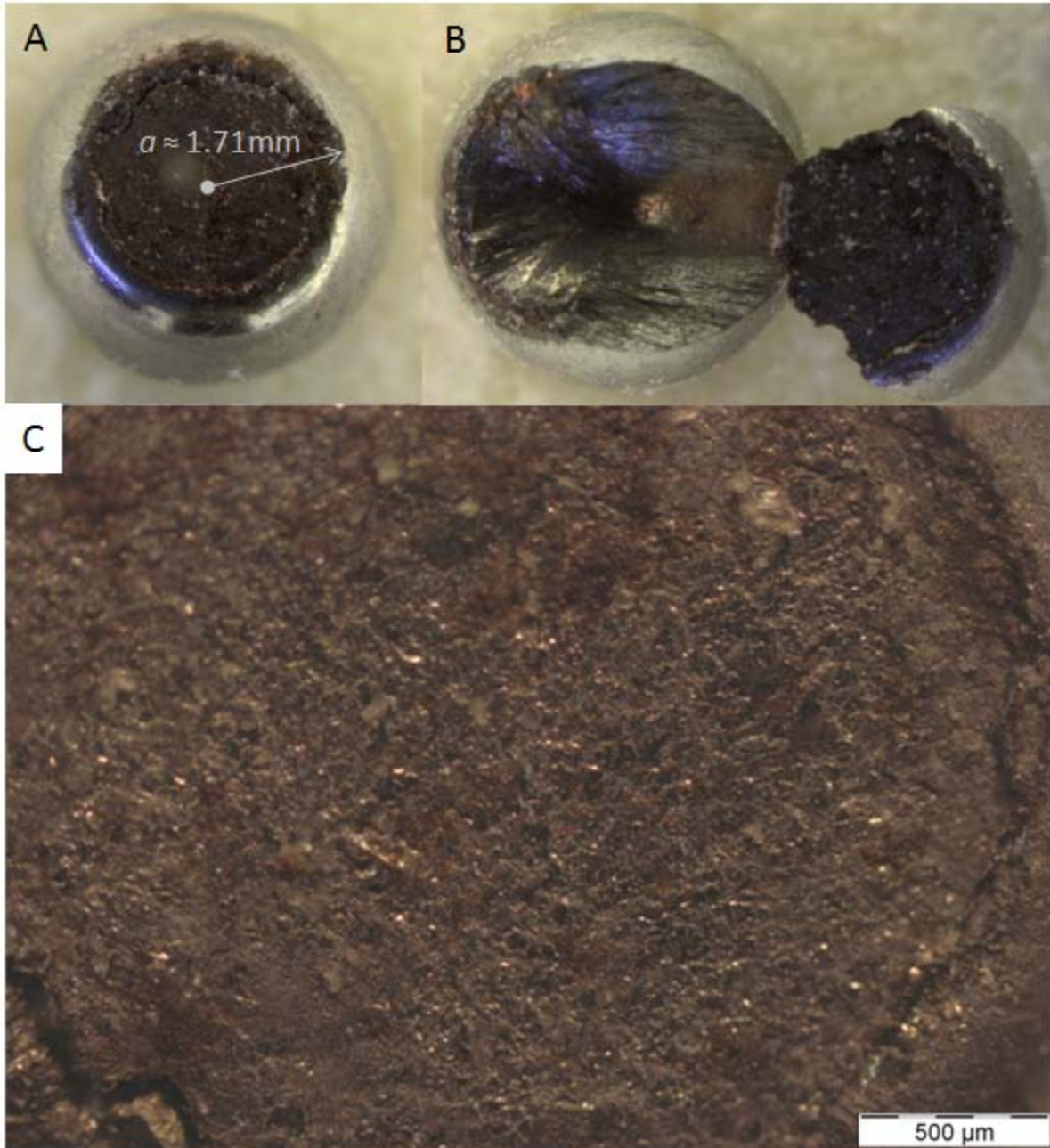


Figure 5-3. Images of recovered ball fragments from the spinel impact tests. Images depict A) fragments in situ, B) fragments separated and C) high magnification image of erosion damage on contact surface.

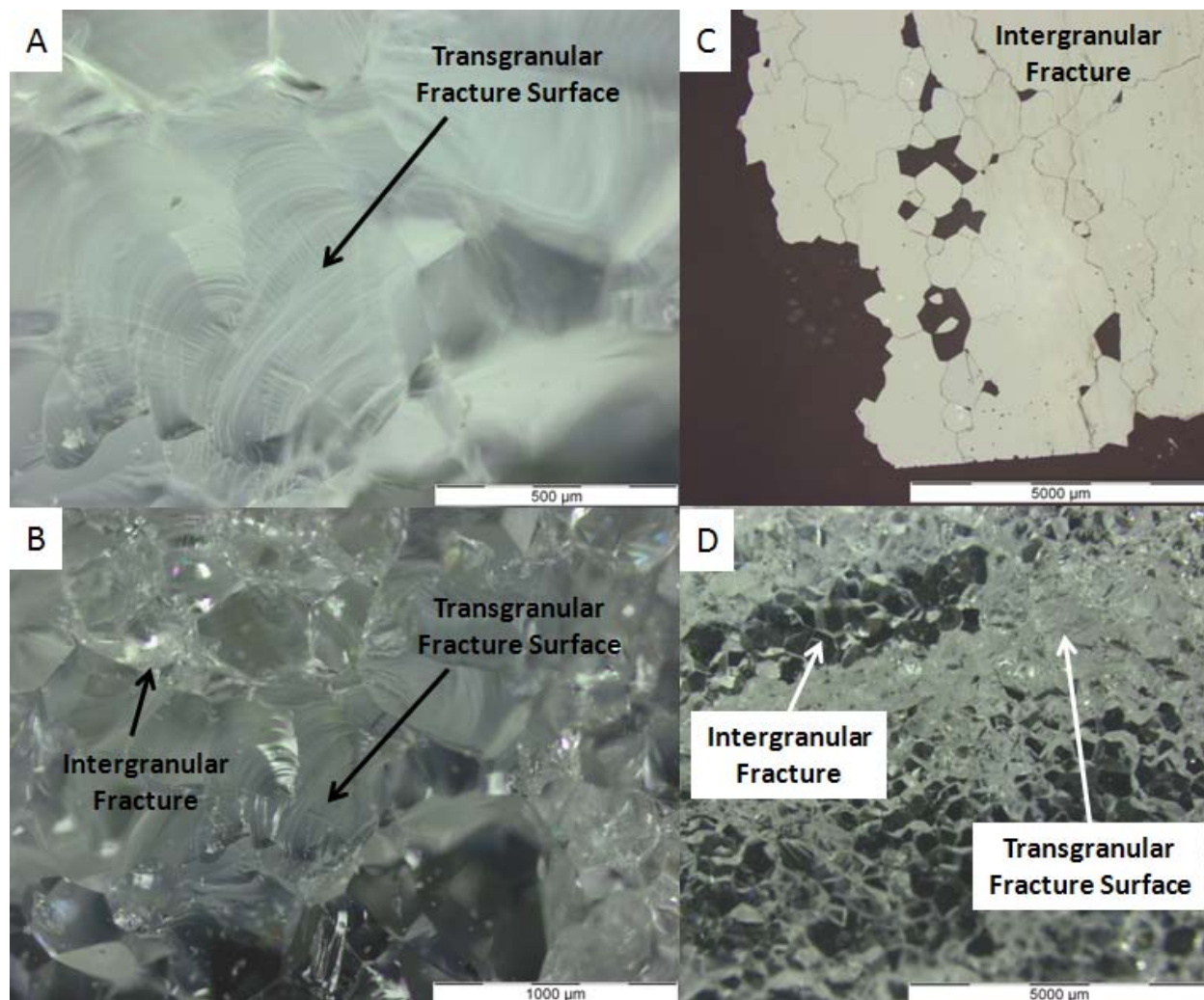


Figure 5-4. Images of fracture within recovered spinel after impact test. Images depict A) and B) extensive transgranular cracking in zone 1 debris and C) and D) dominant intergranular cracking in zone 2.

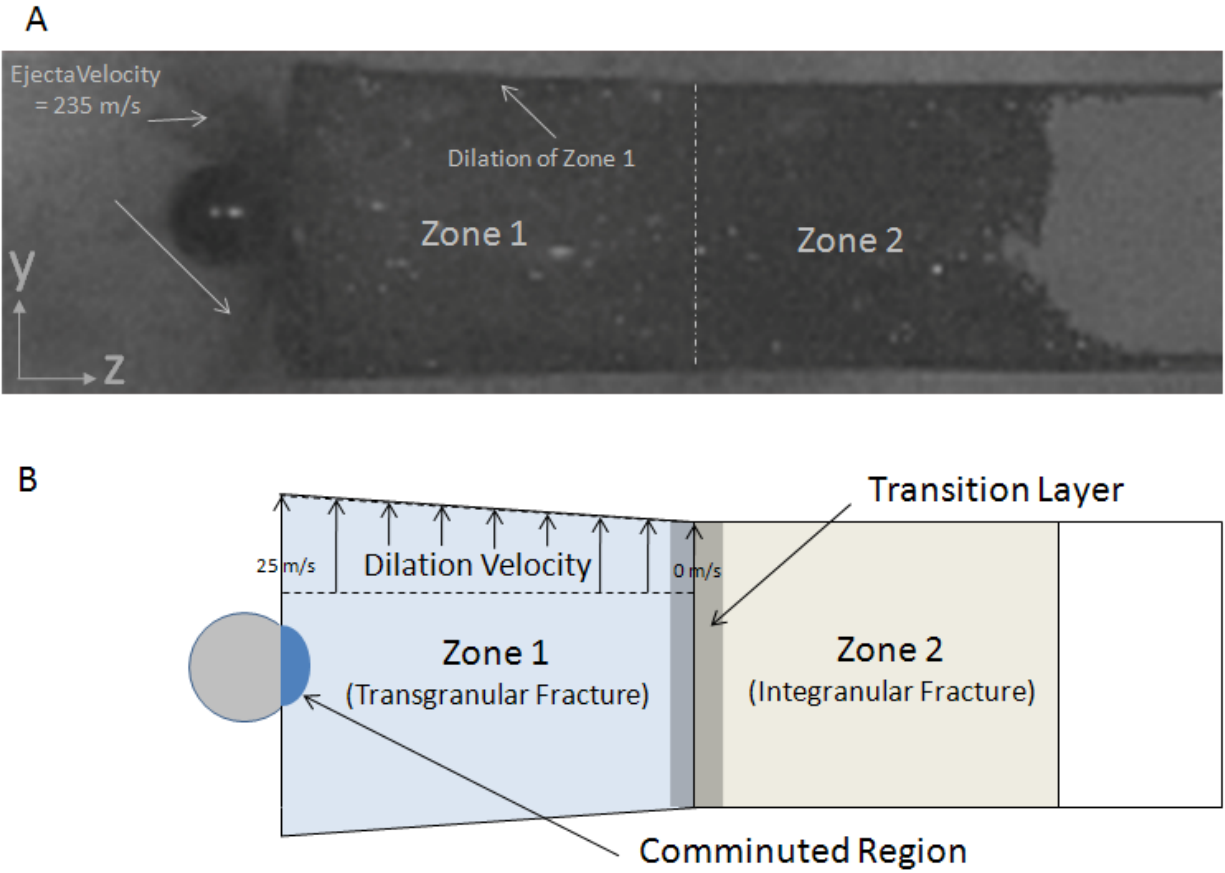


Figure 5-5. A) High magnification image of the spinel bar upon impact showing ejecta and zone 1 dilation and B) schematic depicting various damage zones.

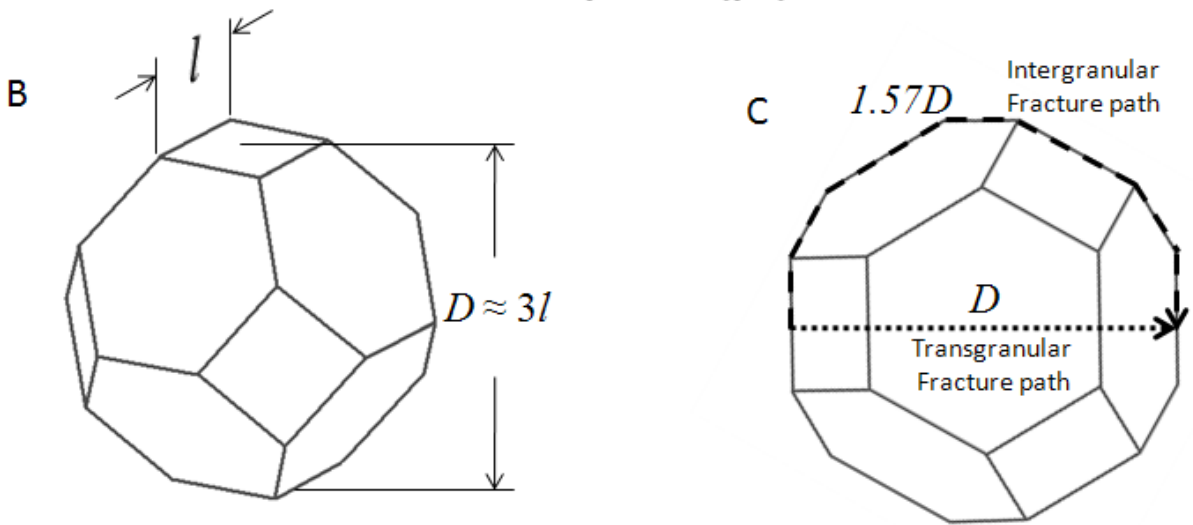
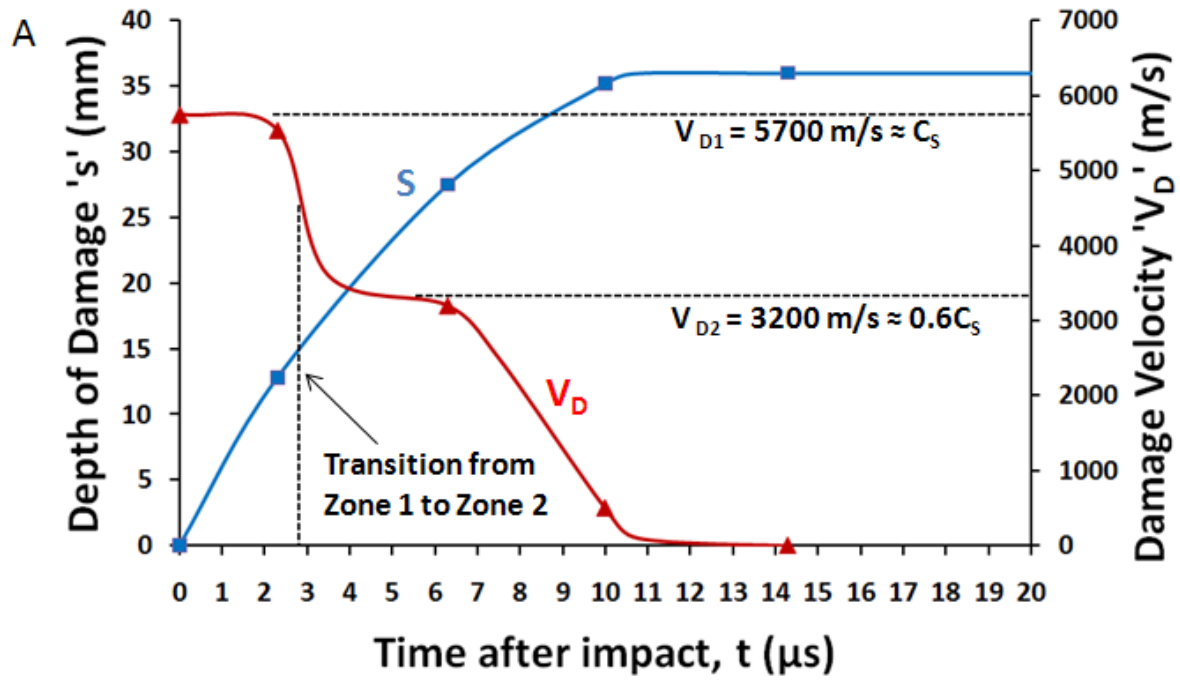


Figure 5-6. A) Plot of damage front depth vs. time for spinel and B) schematics of assumed grain shape showing fracture paths.

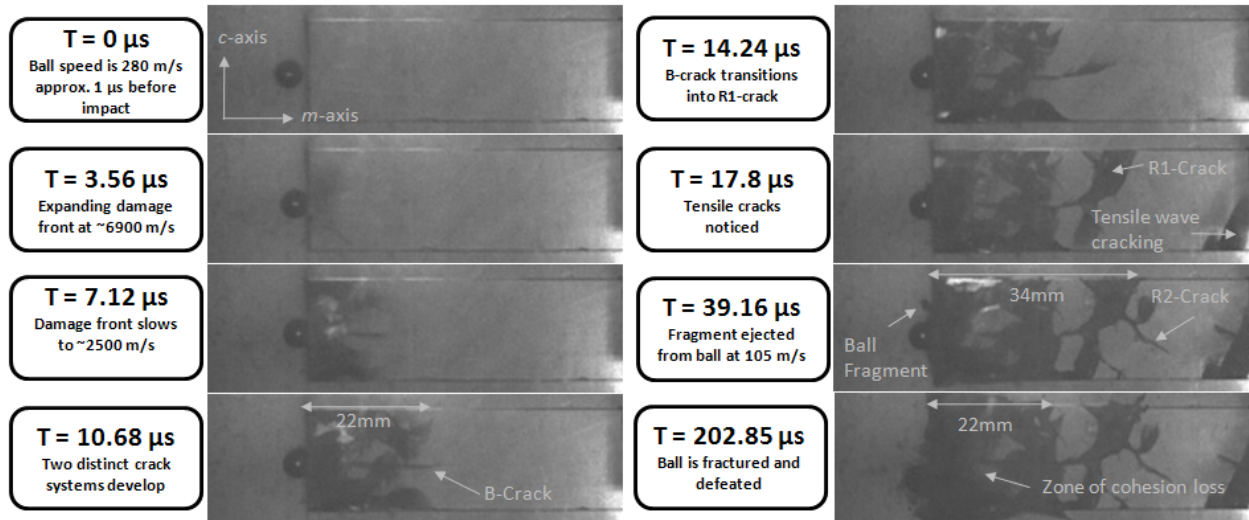


Figure 5-7. Sequence of high speed photographs revealing damage evolution in sapphire due to a steel ball impact at 268 m/s.

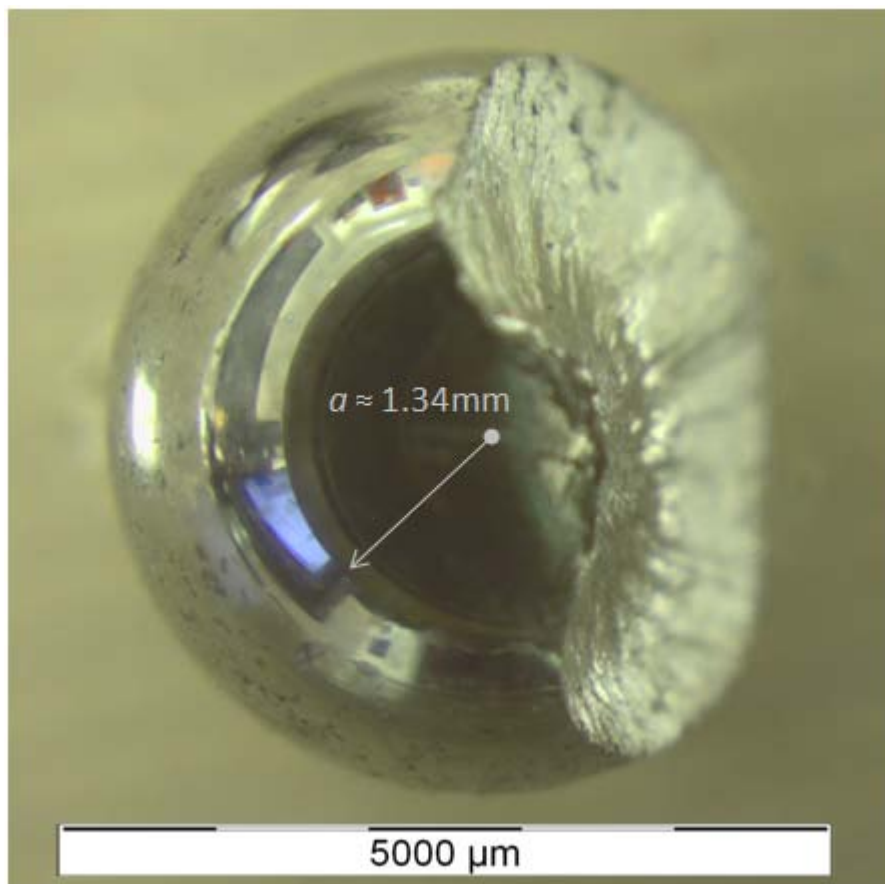


Figure 5-8. Images of recovered ball fragments from the sapphire impact tests showing a fractured surface and a smoothly deformed contact surface

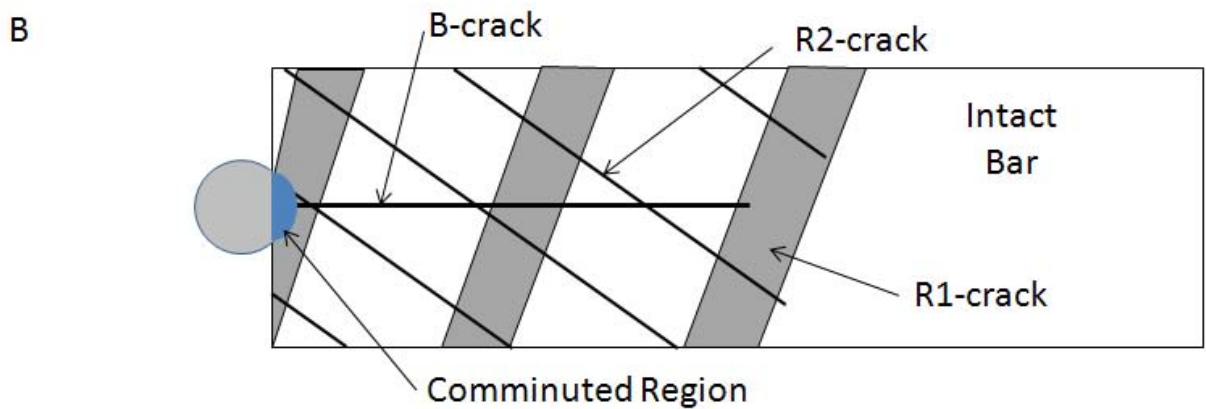
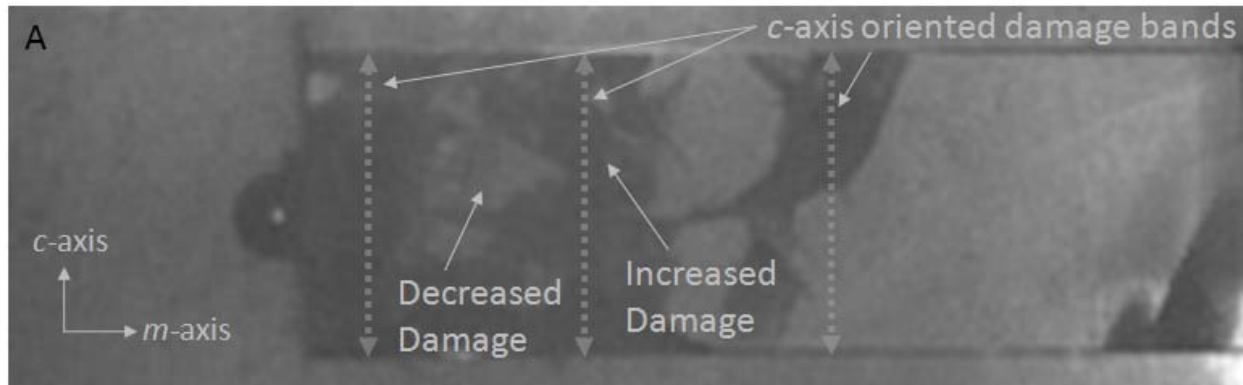


Figure 5-9. A) Magnified image of sapphire rod during impact showing c-axis oriented damage bands and B) a schematic of the criss-crossing B, R1 and R2 cracks



Figure 5-10. Photograph of recovered sapphire rod showing large fragments and triangular shaped zones of dilation and fragmentation.

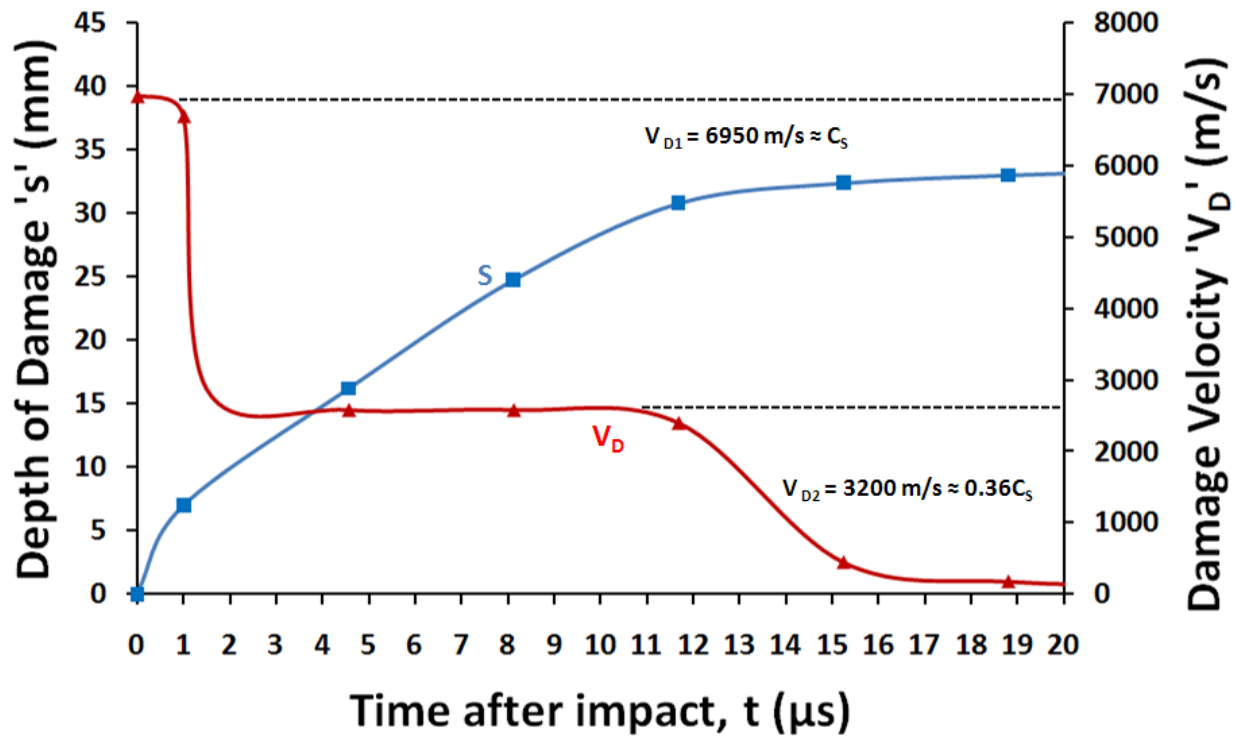


Figure 5-11. Plot of damage front depth vs. time for sapphire.

Energy Dissipation Mechanisms for Impact on Spinel

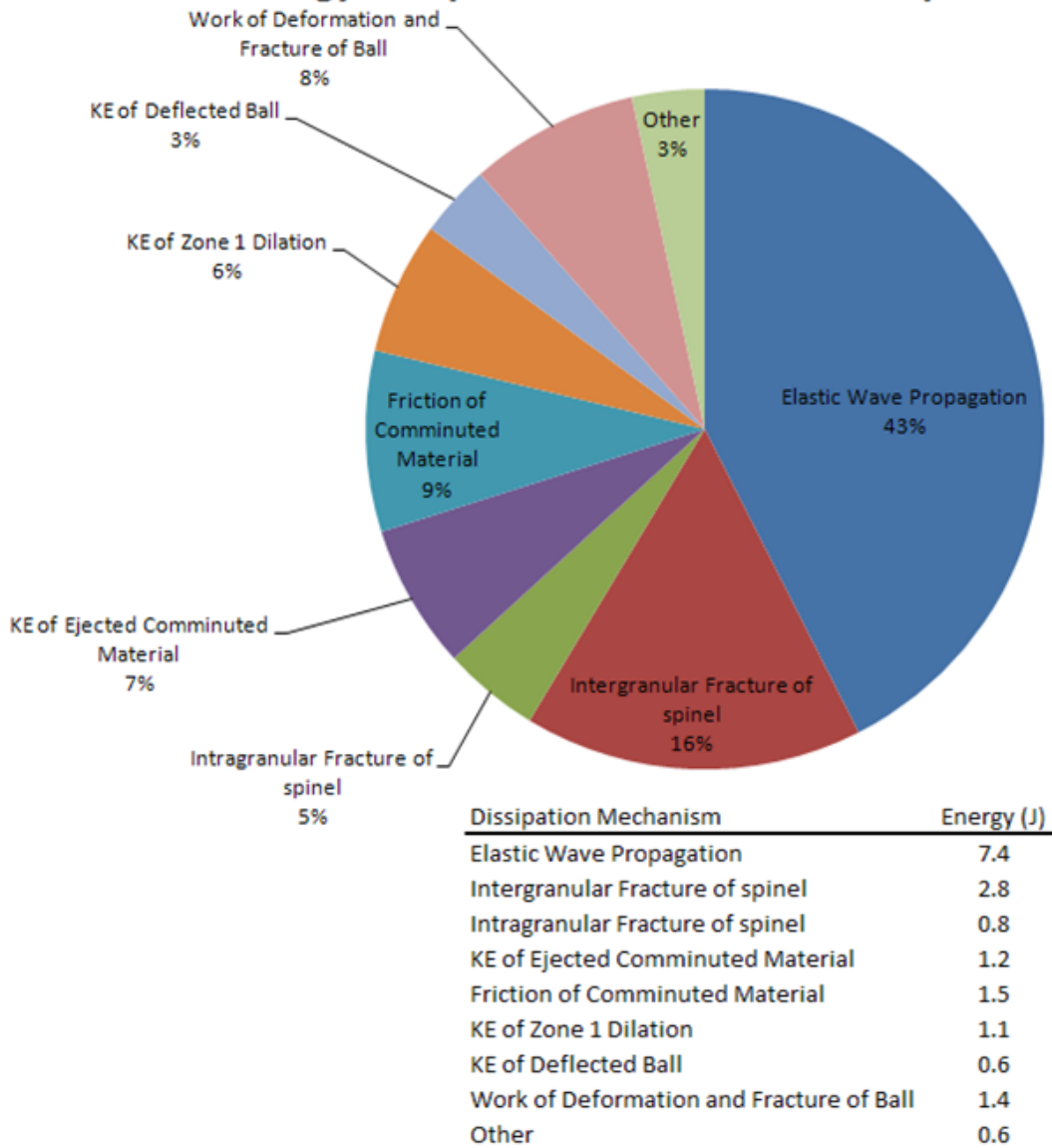


Figure 5-12. Summary of the fractional amount of impact energy dissipated by various deformation and fracture mechanisms in spinel.

Energy Dissipation Mechanisms for Impact on *m*-axis sapphire

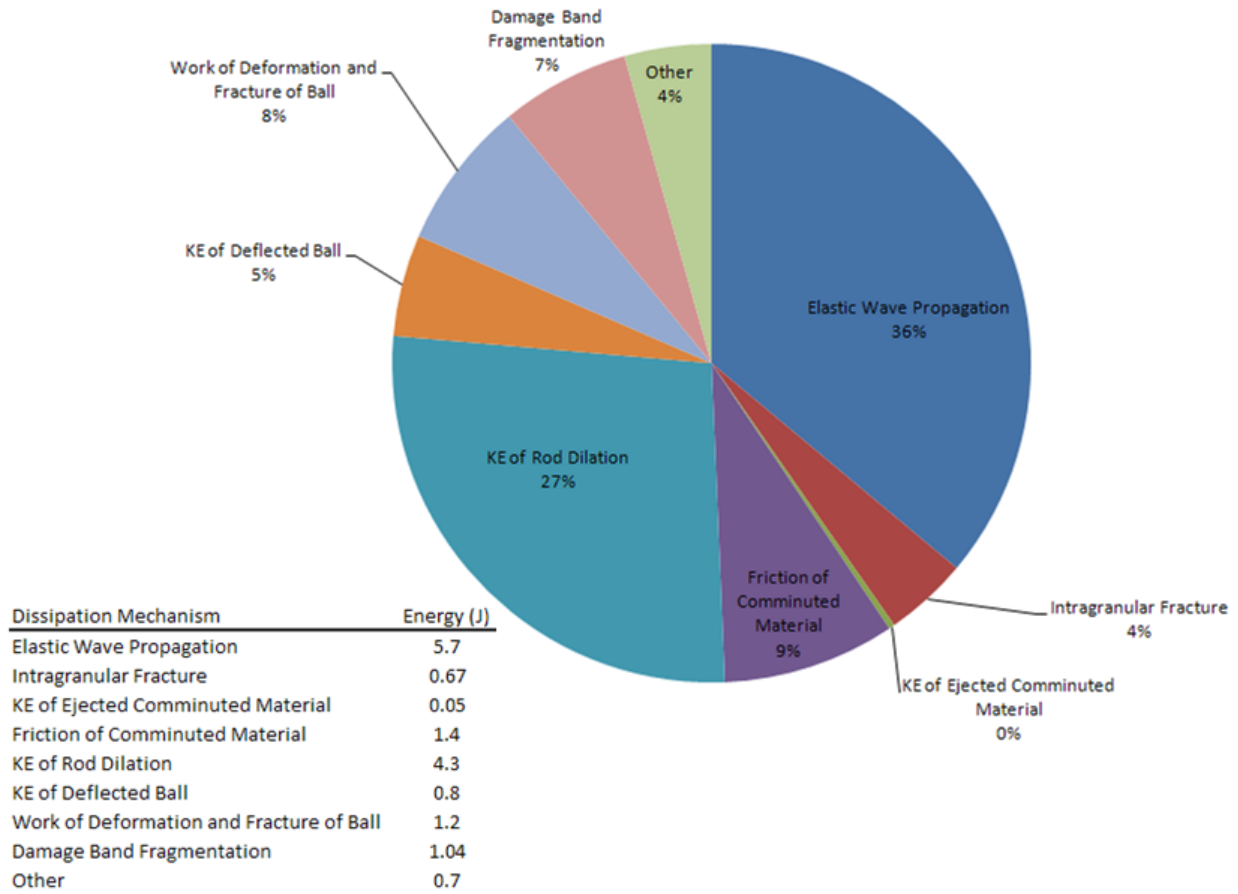


Figure 5-13. Summary of the fractional amount of impact energy dissipated by various deformation and fracture mechanisms in *m*-axis sapphire.

CHAPTER 6 SUMMARY

Research Conclusions

The intent of this research as mentioned in Chapter 1 is to provide a better explanation as to the rationale of the superior ballistic performance of spinel compared to sapphire (Figure 1-1). Comparison of properties such as static hardness and strength do not explain the behavior adequately since sapphire properties are superior to spinel. Additionally, dynamic properties such as HEL and wave velocities are also superior for sapphire compared to spinel; consequentially even dynamic properties are insufficient to explain the difference in ballistic behaviors between the two materials. Table 6-1 provides a comparison of previously published static and dynamic properties for Mg-spinel and *a*-plane sapphire. Novel techniques are being utilized to develop a better understanding of each material during dynamic events in hopes of uncovering rationale as to the origins of the discrepancy.

Dynamic indentation techniques were employed in order to compare the rate sensitivity of indentation hardness, brittleness and fracture character for both sapphire and Mg-spinel. Sapphire demonstrated a greater level of hardness than spinel for both static and dynamic hardness. Sapphire also demonstrated a greater rate sensitivity resulting in more hardness as the indentation loading rate increased. This information, although interesting, is similarly inadequate in explaining the reason for superior ballistic performance of spinel as other dynamic measures such as HEL. The ineffectiveness of hardness as a complete predictor of ballistic performance is also consistent with a growing knowledge that factors beyond hardness are governing ballistic performance of ceramics. Additionally the calculated brittleness was calculated based on the static and

dynamic indentation hardness and fracture toughness. It was discovered that sapphire brittleness was significantly higher (15% static and 26% dynamic) than spinel. This indicates a higher propensity for sapphire to undergo fragmentation, spall and catastrophic failure when dynamically loaded. Table 6-2 provides a direct comparison of spinel and sapphire static and dynamic hardness and brittleness. This study also provided a look at the crack behavior of sapphire and spinel due to static and dynamic indentations [197]. While sapphire indentation cracking was found to propagate along defined crystallographic plane independent of indentation orientation, indentation of spinel resulted in more typical corner cracks. Also interesting with spinel is the shift from predominantly intergranular fracture during static indentations to a more transgranular fracture behavior due to dynamic indentations. It is unknown if this is typical of all polycrystalline materials or unique to spinel. It is also unknown if the grain size is a factor determining the propensity for this behavior. Further research beyond the scope of this study is needed to answer these questions. Although the crack behavior between the two materials is starkly different, an attempt to present the half crack length vs. indentation load for the two materials is presented in Figure 6-1. As can be seen, spinel consistently produces longer indentation cracks than sapphire. At first glance this could be interpreted as another inconsistency between material behavior and ballistic performance, however it is relevant to mention that the shortened long cracks captured during dynamic indentation of sapphire was also accompanied by a much greater amount of lateral cracking and spalling. Knowing that the longer cracks present in spinel can be rationalized as an indication that spinel is dissipating more

energy in long cracks over a larger area. This is important as it allows more broad damage accumulation rather than localized catastrophic damage.

Resultant from the observed unique fracture patterns witnessed in *a*-plane sapphire, an attempt at analyzing the crack interactions due to closely spaced indentations was made. This test provided the first real suggestion as to the origin of sapphire failure due to crack interactivity. This study revealed a unique failure mode that was dependant on the crystal orientation. Heightened levels of damage were witnessed along the *c*-axis that ultimately leads to fragmentation not seen in indentation of spinel. This observation can provide an additional mechanistic theory as to the superior performance of spinel as crack systems develop and interact due to a ballistic impact as follows. As a ballistic projectile impacts a material, a network of crack systems develop and undoubtedly interact with each other. Given the understanding that sapphire demonstrates a propensity for greater damage due to interacting cracks, a theory as to the rationale for increased damage in sapphire as compared to spinel can be formulated.

The final stage of fully characterizing these two materials involved small scale impact tests. This test provided conclusive phenomenological rationale for the improved ballistic performance of spinel. A significant finding was the verification that spinel maintained a greater amount of structural cohesion while allowing crack systems to develop and dissipate energy. Spinel underwent a shift from transgranular to intergranular fracture at a depth of 18mm into the rod. Concurrent with this transition was the preservation of structural cohesion beyond the 18mm deep transition boundary. Sapphire however is found to fracture along defined crystal planes. Fracturing in this

manner resulted in a criss-cross pattern of cracks that ultimately lead to fragmentation, loss of structure integrity and catastrophic failure. Additionally, damage bands oriented with the *c*-axis were noted confirming the importance of the findings from the sequential indentation tests. These damage bands resulted in further fragmentation and loss of structure. In all, the sapphire sample only maintained structural cohesion after a depth of 34mm from the impact plane. This is very interesting since the amount of impact energy delivered to the sapphire (15.9 J) was 91% of that delivered to the spinel sample (17.4 J). Comparing the energy dissipation mechanisms between the two materials reveals further rationale for the inferior ballistic performance of sapphire. Table 6-3 provides a comparison of energy dissipation mechanisms between the two materials. Initially it can be seen that sapphire dissipates a smaller fraction of energy due to elastic wave motion. This dissipation is due to a greater speed of sound inherent with a stiffer material. Also of interest is the high amount of energy dissipated by intergranular fracture of spinel. Sapphire, being a single crystal, does not have this fracture mode available; hence cannot dissipate energy in this fashion. Spinel also demonstrates a greater amount of ejecta emanating from beneath the ball. This ejecta is very important due to the energy it dissipates through kinetic energy of expulsion as well as the erosion damage it imparts onto the ball. Lastly of note is the relatively small amount of energy due to dilation and loss of cohesion of the spinel rod as compared to the sapphire rod. While the spinel rod only dilated for the first 18mm resulting in a energy dissipation of 1.1 J (6%), sapphire dilation continued into the rod for 22mm and resulted in an energy dissipation of 4.3 J (27%). While this mode is effective in energy dissipation, it is also the mode of dissipation that is most catastrophic in nature.

In conclusion, the following findings can be drawn from this thesis:

1. hardness under dynamic impact is not sufficient in predicting ballistic behavior
2. Increased brittleness of sapphire, especially under dynamic loading can provide some indication of increased fragmentation failure ultimately leading to loss of structural cohesion
3. The discovery of a unique failure mode in sapphire due to sequential indentions aligned with the *c*-axis is consistent with observations of damage evolution during ball impact tests confirming that this failure mode is instrumental the loss of structural integrity during ballistic impacts
4. Edge-on-impact tests have proven to be a useful test in analyzing fracture and damage evolution of various materials.
5. Indentation tests on spinel confirm that intergranular cracking is the preferred crack mode in this spinel. As such the availability of grain boundaries for the development of intergranular fracture while maintaining structural cohesion is a major advantage for magnesium spinel in the defeat of ballistic projectiles.

Future Research Plans

As mentioned in the introduction, the applications for these new materials are not limited to transparent armor. Applications such as optical lenses and cell phone windows can also be improved through the use of these materials (Figure 6-3). Rather than ballistic performance, applications such as these require superior fracture resistance and scratch resistance. Additionally optical performance is of heightened concern for these types of applications. As such, characterization of scratch behavior

and loss of optical clarity as scratch damage accumulates is of extreme interest.

Techniques able to systematically add quantifiable amounts of scratch damage to a material and assess loss in optical clarity are needed.

Additionally, as the abrasion resistance of the substrate materials improve, the concern for abrasion of optical thin film coatings (e.g., anti-reflective coatings) emerges. Nanoscratch testing of materials that have thin film coatings would provide evidence of any abrasion resistance concerns surrounding these coatings commonly used in the optics industry.

Table 6-1. Various static and dynamic material Properties for a-plane sapphire and Mg-spinel

	Sapphire	Mg-Spinel
Density (g/cm ³)	3.97	3.58
Young's Modulus (GPa)	386	277
Shear Modulus (GPa)	145	192
Poisson's Ratio	.275	.26
Biaxial Flexural Strength (MPa)	760	172
Compressive Strength (GPa)	2	2.69
Tensile Strength (GPa)	.302	.110
Vickers Hardness (GPa)	18	14.1
K _{IC} (MPa-m ^{1/2})	2.43	2
Hugoniot Elastic Limit (GPa)	23	11.3
Longitudinal Wave Speed (m/s)	11390	9820
Shear Wave Speed (m/s)	7000	5620

Table 6-2. Comparison of static and dynamic hardness and brittleness for spinel and sapphire

	Mg-Spinel	Sapphire	% Difference
Static Hardness (GPa)	14.1	18.0	28%
Dynamic Hardness (GPa)	14.7	20.6	40%
Static Brittleness (μm ⁻¹)	1027	1177	15%
Dynamic Brittleness (μm ⁻¹)	1071	1347	26%

Table 6-3. Comparison of energy dissipation mechanisms for sapphire and spinel

	Sapphire		Mg-spinel	
	Energy (J)	Fractional Energy	Energy (J)	Fractional Energy
Elastic Wave Energy	7.4	43%	5.7	36%
Intergranular fracture	2.8	16%	0	0%
Intragranular fracture	0.8	5%	0.67	4%
Fragmentation	0	0%	1.04	7%
KE of Ejecta	1.2	7%	.05	0%
Friction	1.5	9%	1.4	9%
KE of rod dilation	1.1	6%	4.3	27%
KE of deflected ball	0.6	3%	.8	5%
Ball deformation	1.4	8%	1.2	8%
Other	0.6	3%	.7	4%

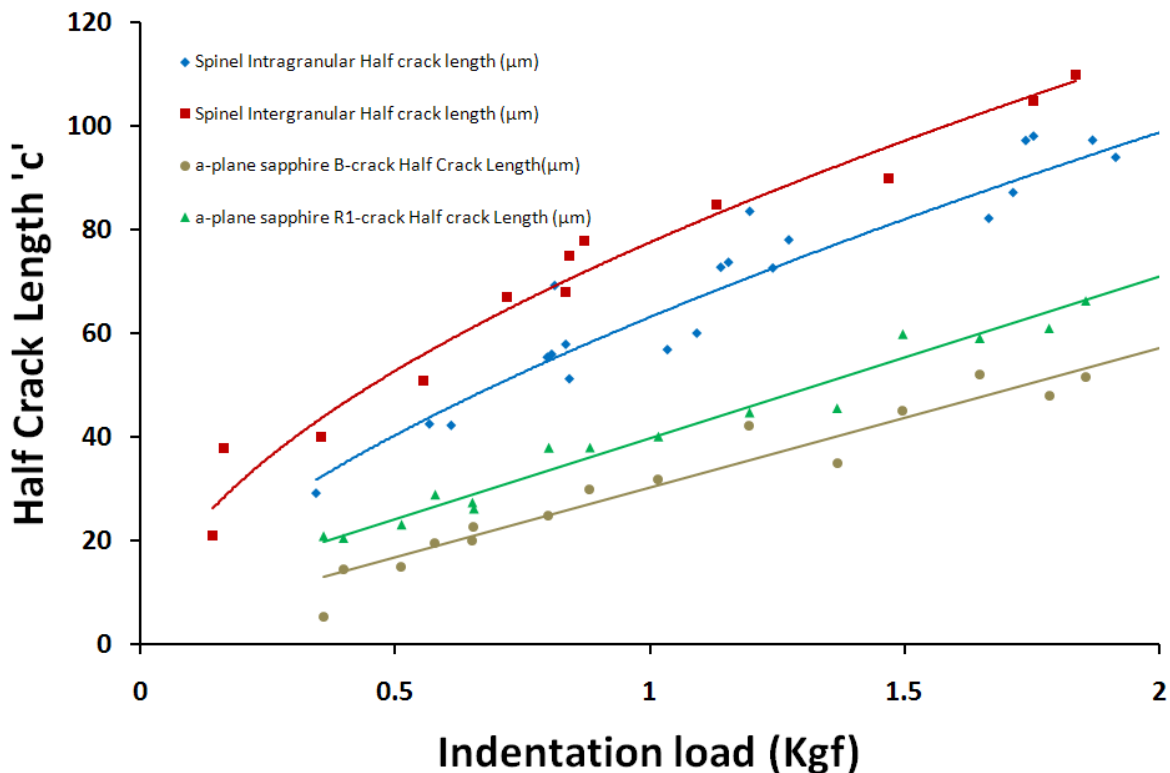


Figure 6-1. Comparison of half crack lengths for spinel and sapphire due to dynamic indentation.



Figure 6-2. Examples of other uses for spinel and sapphire.

LIST OF REFERENCES

- [1] M. Wilkins, C. Honodel and D. Sawle, "An Approach to the Study of Light Armor", *Lawrence Radiation Laboratory Report # UCRL-50284* (1967).
- [2] M. Wilkins et. al., "Second Progress Report of the Light Armor Program", *Lawrence Radiation Laboratory Report # UCRL-50349* (1967).
- [3] M. Wilkins et. al., "Third Progress Report of the Light Armor Program", *Lawrence Radiation Laboratory Report # UCRL-50460* (1968).
- [4] M. Wilkins, C. Cline and C. Honodel, "Fourth Progress Report of the Light Armor Program", *Lawrence Radiation Laboratory Report # UCRL-50694* (1969).
- [5] M. Wilkins, R. Landingham and C. Honodel, "Fifth Progress Report of the Light Armor Program", *Lawrence Radiation Laboratory Report # UCRL-50980* (1971).
- [6] M. Wilkins, R. Landingham and C. Honodel, "Light Armor", *Lawrence Radiation Laboratory Report # UCRL-71817* (1969).
- [7] M. Wilkins, "Mechanics of Penetration and Perforation", *Int. J. Engng. Sci.*, 16, 793-807 (1978).
- [8] R. L. Woodward, "A Simple One Dimensional Approach to Modeling Ceramic Composite Armour Defeat," *Int. J. Imp. Eng.*, 9[4], 455-474 (1990).
- [9] Z. Rozenberg and Y. Yeshurun, "The Relation between Ballistic efficiency and Compressive Strength of Ceramic Tiles," *Int. J. Impact Eng.*, 7[3], 357-362 (1988).
- [10] J. Sternberg, "Material Properties Determining the Resistance of Ceramics to High Velocity Penetration," *J. Appl. Phys.*, 65[9], 3417-3424 (1988).
- [11] Z. Rozenberg and Y. Yeshurun, "On the Influence of the Loss of Shear Strength on the Ballistic Performance of Brittle Solids", *Int. J. Imp. Eng.*, 9[1], 45-49 (1990).
- [12] D. E. Grady, "Shock properties of high-strength ceramics. Constitutive Laws: Experiment and Numerical Implementation", *CIMNE, Barcelona*, pp. 35-45 (1995).
- [13] C. Kaufmann, D. Cronin, M. Worswick, G. Pageau and A. Beth, "Influence of material properties on the ballistic performance of ceramics for personal body armor," *Shock and Vibration*, 10[1], 51-58 (2003).
- [14] P. C. den Reijer, "Impact of Ceramic Faced Armor", Ph.D. Thesis, Delft University of Technology, The Netherlands (1991).
- [15] J. C. LaSalvia, "A Physically-Based Model for the Effect of Microstructure and Mechanical Properties on Ballistic Performance," *Ceram. Eng. and Sci. Proc.*, 23[3], 213-220 (2002).

- [16] A. Krell and E. Straßburger, "Hierarchy of Key Influences on the Ballistic Strength of Opaque and Transparent Armor," *Advances in Ceramic Armor III: Ceram. Eng. and Sci. Proc.*, 28[5], 45-55 (2008).
- [17] R. W. Klopp and D. A. Shockey, "Tests for Determining Failure Criteria of Ceramics Under Ballistic Impact", *Final Report # AD-A256 652, U.S Army Research Office* (1992).
- [18] G. E. Hauver, P. H. Netherwood, R. F. Benck and E. J. Rapacki, Ballistic performance of ceramic targets, In: *Proceedings of the 13th Army Symposium on Solid Mechanics*, Plymouth, MA, (1993).
- [19] G. E. Hauver, P. H. Netherwood, R. F. Benck and L. J. Kecskes, Enhanced ballistic performance of ceramic targets. In: *Proceedings of the 19th Army Science Conference*, Orlando, FL (1994).
- [20] A. G. Evans and T. R. Wilshaw, "Dynamic solid particle damage in brittle materials: an appraisal", *J. Mat. Sci.*, 12[1]. 97-116, (1977).
- [21] G. H. Jilbert and J. E. Field, "Synergistic effects of rain and sand erosion," *Wear*, 243, 6-17 (2000).
- [22] E. J. Coad, C. S. J. Pickles, C. R. Seward, G. H. Jilbert and J. E. Field, "The erosion resistance of infrared transparent materials," *Proc. R. Soc. Lond. A*, 454, 213-238 (1998).
- [23] I. Muruges, S. Srinivasan and R. O. Scattergood, "Models and Material Properties for Erosion of Ceramics," *J. Mat. Res.*, 13[1], 55-61 (1991).
- [24] D. R. Andrews, "An analysis of solid particle erosion mechanisms," *J. Phys. D: Appl. Phys.*, 14, 1979-91 (1981).
- [25] S. Srinivasan and R. O. Scattergood, "R curve effects in solid particle erosion of ceramics," *Wear*, 142, 115-33 (1991).
- [26] C. R. Seward, C. S. J. Pickles, E. J. Coad, M. Watt and J. E. Field, "Studies of Rain erosion Mechanisms in a range of IR Transmitting Ceramics – Including Coated Samples," *Final Report – Contract # SPC-92-4032 PCS Fracture Group*, 246 pp. (1994).
- [27] L. P. Franks, D. Holm and R. Kleinberg, "Transparent Materials for Armor – A Cost Study," *US Army RDECOM-TARDEC Report # 20473RC*, (2010).
- [28] P. Rivers, "Through the Armored Glass", *Ground Combat Technology*, 1[2], (2010).
- [29] D. D. Silva and A. R. Boccaccini, "Industrial Development in the Field of Optically Transparent Inorganic Materials: A Survey of Recent Patents", *Rec. Pat. Mat. Sci.*, [1], 56-73 (2008).

- [30] P. J. Patel and G. A. Gilde, "Transparent Armor Materials: Needs and Requirements"; pp. 573-86 in *Ceramic Armor Materials by Design*, Vol. 134 , Edited by J.W. McCauley, A. Crowson, W. A. Gooch Jr., A. M. Rajendran, S. J. Bless, K. V. Logan, M. Normandia, and S. Wax. Ceramic Transactions, Wiley, Hoboken, NJ, (2002).
- [31] Performance Specification Armor: Transparent, *MIL-PRF-46108C*, US ARMY (1999).
- [32] Purchase Specification Transparent Armor. *ATPD-2352*, US ARMY TACOM (2008).
- [33] D. C. Harris, "Multi-Spectral Transparent Materials Technologies", presented at *Ceramic Leadership Summit*, Baltimore, MD, (2010).
- [34] M. C. L. Patterson, A. DiGiovanni, D. W. Roy and G. Gilde, "Spinel Armor – Clearly the Way to Go", *Ceram. Eng. and Sci. Pro.*, 24[3], 441-46 (2003).
- [35] M. C. L. Patterson, D. W. Roy and G. Gilde, "An Investigation of the Transmission Properties and Ballistic Performance of Hot Pressed Spinel", in *Ceramic Armor Materials by Design*, *Ceramic Transactions*, Vol. 134 , Edited by J.W. McCauley, A. Crowson, W. A. Gooch Jr., A. M. Rajendran, S. J. Bless, K. V. Logan, M. Normandia, and S. Wax. Ceramic Transactions, Wiley, Hoboken, NJ, 2002.
- [36] J. J. Swab, G. A. Gilde, P. J. Patel, A. A. Wereszczak and J. W. McCauley, "Fracture Analysis of Transparent Armor Ceramics", in *Fractography of Glasses and Ceramics IV*, Vol. 122, Edited by: J. R. Varner, G. D. Quinn, The American Ceramic Soc. (2001).
- [37] D. C. Harris, A century of sapphire crystal growth: origin of the EFG method. In: *Proc SPIE*, Vol. 7425, p. 12. (2009)
- [38] P. J. Patel, G. A. Gilde, P. G. Dehmer and J. W. McCauley, "Transparent armor", *AMPTIAC Q.*, 4[3], 1–17 (2000).
- [39] M. J. Normandia, J. C. Lasalvia, W. A. Gooch, J. W. McCauley and A. M. Rajendran, "Protecting the future force: ceramics research leads to improved armor performance", *AMPTIAC Q.*, 8[4], 21–7 (2004).
- [40] Saint Gobain crystals product literature,
<http://www.photonic.saint448gobain.com/uploadedFiles/SGphotonic/Documents/sapphire-materialproducts-properties.pdf> [Last Accessed 1-12-11].
- [41] E. R. Dobrovinskaya, L. A. Lytvynov and V. Piskchik, *Sapphire: material, manufacturing, applications*, New York: Springer; 2009.
- [42] V. N. Vetrov and B. A. Ignatenkov, "Birefringence in synthetic sapphire lenses", *J. Opt. Technol.*, 73[5], 349–51 (2006).

- [43] J. D. Clayton, "Finite Deformation by Elasticity, Slip and Twinning: Atomistic Considerations, Continuum Modeling, and Application to Ceramic Crystals", *ARL Report # ARL-RP-244* (2009).
- [44] F. Schmid and D. C. Harris, "Effects of Crystal Orientation and Temperature on the Strength of Sapphire," *J. Am. Ceram. Soc.*, 81[4] 885-93 (1998).
- [45] R. Nowak and M. Sakai, "The anisotropy of surface deformation of sapphire: continuous indentation of triangular indenter", *Acta. Metall. Mater.*, 42[8], 2879-91 (1994).
- [46] R. Nowak, T. Sekino and K. Niihara, "Surface Deformation of Sapphire Crystal", *Phil. Mag. A*, 74[1], 171-94 (1996).
- [47] R. Nowak, T. Sekino, S. Maruno and K. Niihara, "Deformation of sapphire induced by a spherical indentation on the (1010) plane", *Appl. Phys. Lett.*, 68[8], 1063-65 (1996).
- [48] R. Nowak, T. Sekino and K. Niihara, "Non-Linear Surface Deformation of the (1010) Plane of Sapphire: Identification of the Linear Features around Spherical Impressions", *Acta. Mater.*, 47[17], 4329-38 (1999).
- [49] N. I. Tymiak and W. W. Gerberich, "Initial stages of contact induced plasticity in sapphire. I. Surface traces of slip and twinning", *Phil. Mag.*, 87[33], 5143-68 (2007).
- [50] T. F. Page, W. C. Oliver and C. J. McHargue, "The deformation behavior of ceramic crystals subjected to very low load (nano)indentations", *Mater. Res.*, 7, (1992).
- [51] Y. G. Kim and D. K. Kim, "In situ observation of fracture sequence of physical vapor deposited TiN film on (1120) sapphire", *J. Mat. Res.*, 20[6] 1389-95 (2005).
- [52] N. I. Tymiak, A. Daugela, T. J. Wyrobek and O. L. Warren, "Highly localized acoustic emission monitoring of nanoscale indentation contacts", *J. Mat. Res.*, 18[4] 784-96 (2003).
- [53] W. W. Gerberich, J. C. Nelson, E. T. Lilleodden, P. Anderson and J. T. Wyrobek, "Indentation Induced Dislocation Nucleation: The Initial Yield Point", *Acta. Mater.*, 44[9], 3585-98 (1996).
- [54] A. Gouldstone, H. J. Koh, K. Y. Zeng, A. E. Giannakopoulos and S. Suresh, "Discrete and Continuous Deformation During Nanoindentation of Thin Films", *Acta. Mater.*, 48[9], 2277-95 (2000).
- [55] M. V. Swain and M. Wittling, "Comparison of acoustic emission from pointed and spherical indentation of TiN films on silicon and sapphire", *Surf. Coat. Tech.*, 76-77, 528-33 (1995).

- [56] N. I. Tymiak, A. Daugela, T. J. Wyrobek and O. L. Warren, "Acoustic emission monitoring of the earliest stages of contact-induced plasticity in sapphire", *Acta Mater.*, 52, 553-63 (2004).
- [57] W. D. Scott and K. K. Orr, "Rhombohedral twinning in sapphire", *J. Am. Ceram. Soc.*, 66[1], 27-32 (1983).
- [58] D. C. Harris, F. Schmid, J. J. Mecholsky Jr. and Y. L. Tsai, "Mechanism of Mechanical Failure of Sapphire at High Temperature," *Proc. SPIE—Int. Soc. Opt. Eng.*, Vol. 2286, 16-25 (1994).
- [59] L. F. Johnson and M. B. Moran, "Compressive coatings for strengthened sapphire," *Proc. SPIE Window and Dome Technologies and Materials VI*, Vol. 3705 (1999).
- [60] F. Schmid, C. P. Khattak, K. A. Schmid, S. G. Ivanova and D. C. Harris, "Increase of high temperature strength of sapphire by polishing, heat treatments and doping," *Proc. SPIE Optical Materials II*, Vol. 4102 (2000).
- [61] E. Savrun, C. Toy, W. D. Scott and D. C. Harris, "The Effect of Titanium Doping on the Rhombohedral Twinning of Sapphire," *Proc. SPIE Window and Dome Technologies and Materials VI*, Vol. 3705 (1999).
- [62] E. Savrun, W. D. Scott and D. C. Harris, "Effect of Titanium Doping on the High-Temperature Rhombohedral Twinning of Sapphire," *J. Mater. Sci.*, 36, 2295 (2001).
- [63] A. Kirkpatrick and D. C. Harris, L. F. Johnson, "Effect of Ion Implantation on the Strength of Sapphire at 300-600°C," *J. Mater. Sci.*, 36, 2195, (2001).
- [64] F. Schmid, K. Schmid, C. P. Khattak, P. R. Duggan and D. C. Harris, "Increasing the Strength of Sapphire by Heat Treatments," *Proc. SPIE*, Vol. 3705, 36 (1999).
- [65] T. M. Regan, D. C. Harris, R. M. Stroud and J. R. White, "Neutron Irradiation for Sapphire Compressive Strengthening. I. Processing Conditions and Compressive Strength," *J. Nucl. Mater.*, 300, 39 (2002).
- [66] T. M. Regan, D. C. Harris, D. W. Blodgett, K. C. Baldwin, J. A. Miragliotta, M. E. Thomas, M. J. Linevsky, J. W. Giles, T. A. Kennedy, M. Fatemi, D. R. Black and K. P. D. Lagerlöf, "Neutron Irradiation for Sapphire Compressive Strengthening. II. Physical Property Changes," *J. Nucl. Mater.*, 300, 47 (2002).
- [67] F. Schmid, C. P. Khattak, S. G. Ivanova, D. M. Felt and D. C. Harris, "Influence of Polishing on the Biaxial Flexure Strength of Sapphire at 600°C," *Proc. 8th DoD Electromagnetic Windows Symposium*, Boulder, Colorado, (2000).
- [68] D. C. Harris, "Overview of Progress in Strengthening Sapphire at Elevated Temperature," *Proc. SPIE*, Vol. 3705, 2 (1999).

- [69] G. I. Kanel, W. J. Nellis, A. S. Savinykh, S. V. Raorenov and A. M. Rajendran "Effect of Crystalline Anisotropy on Shock Propagation in Sapphire", *AIP Conf. Proc.*, 1195, pp. 851-854 (2009).
- [70] G. I. Kanel, W. J. Nellis, A. S. Savinykh, S. V. Raorenov and A. M. Rajendran, "Response of seven crystallographic orientations of sapphire crystals to shock stresses of 16-86 Gpa", *J. App. Phy.*, 106[4] (2009).
- [71] G. J. Gleiser, L. C. Chhabildas and W. D. Reinhart, "Shock Loading of Polycrystalline Alumina and Sapphire," *AIP Conf. Proc.; Shock. Comp. Cond. Matter.*, 981-84 (2009).
- [72] J. M. Winey and D. E. Hare, "r-axis sound speed and elastic properties of sapphire single crystals," *J. App. Phys.*, 90[6], 3109-11 (2001).
- [73] R. A. Graham and W. P. Brooks, "Shock-wave compression of sapphire from 15 to 420 kbar. The effects of large anisotropic compressions", *J. Phys. Chem. Solids.*, 32, 2311–2330 (1971).
- [74] K. E. Sickafus, N. W. Wills and N. W. Grimes, "Structure of Spinel", *J. Am. Ceram. Soc.*, 82[12], 3279-92 (1999).
- [75] T. J. Mroz, T. M. Hartnett, J. M. Wahl and L. M. Goldman, "Recent Advances in Spinel Optical Ceramic," *Proc. SPIE*, Vol. 5786, 64–70 (2005).
- [76] S. M. Sweeney, M. K. Brun, T. J. Yosenick, A. Kebbede and M. Manoharan, "High strength transparent spinel with fine, unimodal grain size", *Proc. SPIE*, Vol. 7302 (2009).
- [77] M. Patterson, G. Gilde and D. Roy, "Fabrication of Large Thick Panels of Transparent Spinel", in *Organic Optical Materials III*, Ed. By A. J. Marker III, M. J. Davis, SPIE, Orlando, FL, 2001.
- [78] J. J. Swab, J. C. LaSalvia, G. A. Gilde, P. J. Patel and M. J. Motyka, " Transparent Armor Ceramics: ALON and Spinel", pp. 79-84 in *Advances in Ceramic Armor V*, *Ceram. Eng. Sci. Proc.*, 30[5] (2009).
- [79] G. Gilde, P. Patel, P. Patterson, D. Blodgett, D. Duncan and D. Hahn, "Evaluation of Hot Pressing and Hot Isostatic Pressing Parameters on the Optical Properties of Spinel," *J. Am. Ceram. Soc.*, 88 [10], 2747–51 (2005).
- [80] D. C. Harris, "History of development of polycrystalline optical spinel in the U. S.," *Proc. SPIE Window and Dome Technologies and Materials IX*, Vol. 5786 (2005).
- [81] D. C. Harris, "Transparent Spinel Development," *Proc. SPIE Inorganic Optical Materials II*, Vol. 4102 (2000).

- [82] D. M. Chay, H. Palmour III and W. W. Kreigel, "Microstructure and Room Temperature Mechanical Properties of Hot-Pressed Magnesium Aluminate as Described by Quadratic Multivariable Analysis," *J. Am. Ceram. Soc.*, 51, 10-16 (1968).
- [83] D. H. Chung, G. R. Terwilliger, W. B. Crandall and W. G. Lawrence, "ELASTIC PROPERTIES OF MAGNESIA AND MAGNESIUM ALUMINATE SPINEL", *Final Report, Contract Number DA31124AROD23, STATE UNIV. OF NEW YORK ALFRED COLL. OF CERAMICS*, (1964).
- [84] Y. Akimune and R. C. Bradt, "Knoop Microhardness Anisotropy of Single Crystal Stoichiometric $MgAl_2O_4$ ", *J. Am. Ceram. Soc.*, 70[4] C-84-C-86 (1987).
- [85] R. L. Stewart, M. Iwasa and R. C. Bradt, "Room-Temperature KIC Values for Single-Crystal and Polycrystalline $MgAl_2O_4$," *J. Am. Ceram. Soc.*, 64 [2] C-22–C-23 (1981).
- [86] K. Morita, B-N Kim, K. Hiraga and H. Yoshida, "Fabrication of high-strength transparent $MgAl_2O_4$ spinel polycrystals by optimizing spark-plasma-sintering conditions", *J. Mat. Res.*, 24, 2863-72 (2009).
- [87] T. M. Hartnett and R. L. Gentilman, "Optical and mechanical properties of highly transparent spinel and ALON domes", *Proceedings of the SPIE Conference on Advances in Optical Materials*, Vol. 505, 15-22 (1984).
- [88] K. A. Wickersheim and R. A. Lefever, "Optical Properties of Synthetic Spinel," *J. Opt. Soc. Am.*, 50, 831-832 (1960).
- [89] W. J. Tropf and M. E. Thomas, "Magnesium Aluminum Spinel ($MgAl_2O_4$), in E. D. Palik (ed.), *Handbook of Optical Constants of Solids II*, Academic Press, Orlando, 881–895 (1991).
- [90] T.E. Mitchell, L. Hwang and A. H. Heuer, "Deformation in Spinel", *J. Mat. Sci.*, 11[2], 264-72 (1976).
- [91] T. E. Mitchell, "Dislocations and Mechanical Properties of $MgO-Al_2O_3$ Spinel Single Crystals," *J. Am. Ceram. Soc.*, 82[12], 3305-16 (1999)
- [92] R. L. Stewart, "Fracture of Magnesium Aluminate Spinel", *Ph.D. Dissertation, The Pennsylvania State University*, (1981).
- [93] R. L. Stewart and R. C. Bradt, "Fracture of Polycrystalline $MgAl_2O_4$ ", *J. Am. Ceram. Soc.*, 63[11-12], 619-23 (1980).
- [94] A. Ghosh, K. W. White, M. G. Jenkins, A. S. Kobayashi and R. C. Bradt, "Fracture Resistance of a Transparent Magnesium Aluminate Spinel", *J. Am. Ceram. Soc.*, 74[7], 1624-30 (1991).

- [95] K. W. White and G. P. Kelkar, "Fracture Mechanisms of a Coarse-Grained, Transparent MgAl_2O_4 at Elevated Temperatures", *J. Am. Ceram. Soc.*, 75[12], 3440-44 (1992).
- [96] C. Baudín, R. Martínez and P. Pena, "High-Temperature Mechanical Behavior of Stoichiometric Magnesium Spinel", *J. Am. Ceram. Soc.*, 78[7], 1857-62 (1995).
- [97] R. L. Stewart and R. C. Bradt, "Fracture of single crystal MgAl_2O_4 ", *J. Mat. Sci.*, 15, 67-72 (1980).
- [98] M. Sakai, R. C. Bradt and A. S. Kobayashi, "The Toughness of Polycrystalline MgAl_2O_4 ", *Nippon-SeramikkUSlRkyokai-Gakujutsu-Ronbunshi*, 96[5], 525-31 (1988).
- [99] C. Baudín and P. Pena, "Influence of Stoichiometry on Fracture Behavior of Magnesium Aluminate Spinel at 1200°C ", *J. Eur. Ceram. Soc.*, 17[12], 1501-11 (1997).
- [100] J. Salem and L. Ghosn, "Measuring Crack Length in Course Grain Ceramics", *Int. J. Fract.*, 164, 319-23 (2010).
- [101] P. J. Patel, J. J. Swab and G. Gilde, "Fracture properties and behavior of transparent ceramics," *Proc. SPIE Inorganic Optical Materials II*, Vol. 4102 (2000).
- [102] X. Nie, J. C. Wright, W. W. Chen, L. Fehrenbacher and I. Vesnovsky, "Rate Effects on the Mechanical Response of Magnesium Aluminate Spinel", *Mat. Sci. Eng. A*, (2011).
- [103] V. Paris, S. Hayun, M. P. Dariel, N. Frage and E. Zaretsky, "On the Compressive and Tensile Strength of Magnesium Aluminate Spinel," *AIP Conf. Proc.: Shock Compression of Condensed Matter*, pp. 1003-06 (2009).
- [104] S. P. Marsh, *LASL Shock Hugoniot Data*, University of California Press, p. 420 (1980).
- [105] Y. Ashuach, Z. Rosenberg and E. Dekel, "On the Spall Strengths and Hugoniot Elastic Limits of Some Strong Ceramics", *AIP Conf. Proc.: Shock Compression of Condensed Matter*, pp. 473-76 (2007).
- [106] J.A. Salem, "Slow Crack Growth and Fracture Toughness of Sapphire for the International Space Station Fluids and Combustion Facility," *NASA/TM Report # 2006-214023* (2006).
- [107] R. J. Anton and G. Subhash, "Dynamic Vickers indentation of brittle materials", *Wear*, 239, 27-35 (2000).

- [108] D. Ghosh, G. Subhash, T. S. Sudharshan, R. Radhakrishnan and X. Gao, "Dynamic indentation response of fine-grained boron carbide", *J. Am. Ceram. Soc.*, 90[6], 1850–7 (2007).
- [109] M. Klecka and G. Subhash, "Rate dependant indentation response of structural ceramics", *J. Am. Ceram. Soc.*, 93[10], 2377–83 (2010).
- [110] M. M. Chaudhri, J. K. Wells and A. Stevens. Dynamic hardness, deformation and fracture of simple ionic crystals at very high rates of strain. *Phil. Mag A*, 43[3], 643–64 (1981).
- [111] S. Wang and P. Pirouz, "Mechanical properties of undoped GaAs. III. Indentation experiments", *Acta Mater.*, 55, 5526–37 (2007).
- [112] N. M. Jennett and J. Nunn, "High resolution measurement of dynamic (nano) indentation impact energy: a step towards the determination of indentation fracture resistance", *Phil. Mag*, 21 (2010).
- [113] C. D. Jones, J. B. Rioux, J. W. Locker, H. E. Bates and S. A. Zanella, "Large-area sapphire for transparent armor", *Am. Ceram. Soc. Bull.*, 85[3], 24–6 (2006).
- [114] ASTM E112, 1996, "Standard Test Methods for Determining Average Grain Size", ASTM International, West Conshohoken, PA, 1996, DOI: 10.1520/E0112-10, www.astm.org.
- [115] G. Subhash, Dynamic indentation testing. In: *ASM handbook on mechanical testing and evaluation*, vol. 8. Materials Park, OH: ASM International, p. 519–29 Edited by: H. Kuhn and D. Medlin (2000).
- [116] B. R. Lawn, *Fracture of brittle solids*. Cambridge: Cambridge University Press; 1995.
- [117] S. Nemat-Nasser, J. B. Isaacs and J. E. Starrett, "Hopkinson techniques for dynamic recovery experiments", *Proc. R. Soc. Lond. A*, 435, 371–91 (1999).
- [118] E. Meyer, "Untersuchungen über Härteprüfung und Härte", *Z. VerDtsch. Ing.*, 52[17], 645–54 (1908).
- [119] H. Li and R. C. Bradt, "The microhardness indentation load/size effect in rutile and cassiterite single crystals", *J. Mater. Sci.*, 2[4], 917–26 (1993).
- [120] H. Li, H. Suematsu, T. Iseki and R. C. Bradt, "Microhardness anisotropy and the indentation load/size effect in $\text{MgO} \cdot x\text{Al}_2\text{O}_3$ single crystals", *J. Ceram. Soc. Jpn.*, 99(11), 1079–87 (1991).
- [121] K. Masaki, M. E. Stevenson and R. C. Bradt, "Knoop microhardness anisotropy and the indentation size effect on the basal plane of single-crystal alumina (sapphire)", *J. Am. Ceram. Soc.*, 85[2], 415–22 (2002).

- [122] J. B. Quinn and G. D. Quinn, "Indentation Brittleness of Ceramics: A Fresh Approach", *J. Mater. Sci.*, 32, 4331–4346. (1997).
- [123] W. Zhang and G. Subhash, "An elastic-plastic-cracking model for finite element analysis of indentation cracking in brittle materials", *Int. J. Sol. Str.*, 38, 5893-5913, (2001).
- [124] B. R. Lawn and D. B. Marshall, "Hardness, Toughness, and Brittleness: An Indentation Analysis", *J. Am. Ceram. Soc.*, 62 [7-8] 347–50 (1979).
- [125] H. Horii and S. Nemat-Nasser, "Brittle Failure in Compression: Splitting, Faulting and Brittle-Ductile Transition", *Phil. Trans. R. Soc. Lond.*, A319, 37-74 (1986).
- [126] Z. Rosenberg, "On the shear strength of shock loaded brittle solids", *J. Appl. Phys.*, 76[3], (1994).
- [127] P. J. Patel, J. J. Swab, M. Staley and G. D. Quinn, "Indentation Size Effect (ISE) of Transparent AlON and MgAl₂O₄", ARL Report ARL-TR-3852 (2006).
- [128] F. Zhou, J. Molinari and K. T. Ramesh, "Effects of material parameters on the fragmentation of brittle materials", *Int. J. Fract.*, 139[2], 169-96, (2006).
- [129] G. D. Quinn and R. C. Bradt, "On the Vickers Indentation Fracture Toughness test," *J. Am. Ceram. Soc.*, 90 [3] 673–80 (2008).
- [130] C. Attinger, "Orientation and hardness of synthetic corundum", *Ind. Diam. Rev.*, 12[1], 136–7 (1952).
- [131] B. J. Hockey, "Plastic deformation of aluminum oxide by indentation and abrasion", *J. Am. Ceram. Soc.*, 54[5], 223–31 (1971).
- [132] W. Kollenberg, "Plastic deformation of Al₂O₃ single crystals by indentation at temperatures up to 750°C", *J. Mater. Sci.*, 23, 3321–5 (1988).
- [133] H. M. Chan and B. R. Lawn, "Indentation deformation and fracture of sapphire", *J. Am. Ceram. Soc.*, 71[1], 29–35 (1988).
- [134] B. Y. Farber, S. Y. Yoon, K. P. D. Lagerlöf and A. H. Heuer, "Microplasticity during high temperature indentation and the Peierls potential in sapphire (Al₂O₃) single crystals", *Phys. Status Solidi A*, 137[2], 485–98 (1993).
- [135] R. F. Cook and G. M. Pharr, "Direct observation and analysis of indentation cracking in glasses and ceramics", *J. Am. Ceram. Soc.*, 73[4], 787–817 (1990).
- [136] N. Tymiak, D. Chrobak, W. Gerberich, O. Warren and R. Nowak, "Role of competition between slip and twinning in nanoscale deformation of sapphire", *Phys. Rev. B*, 79, (2006).

- [137] D. K. Shetty, I. G. Wright, P. N. Mincer and A. H. Clauer, "Indentation fracture of WC-Co cermets", *J. Mat. Sci.*, 20[5], 1873-82 (1985).
- [138] D.E. Grady, "Incipient spall, crack branching, and fragmentation statistics in the spall process", *J. de Physique*, Colloque C3, Supplement au no. 9, Tome 49 (1988).
- [139] STANAG 4569. Protection levels for light armoured and logistic vehicles levels. NATO.
- [140] MIL-STD-810E. Department of defense test method standard for environmental engineering considerations and laboratory tests. Washington (DC): US Department of Defense.
- [141] C. D. Jones, J. B. Rioux, J. W. Locker, V. Pluen and M. Mandelartz. "Ballistic Performance of Commercially Available Saint-Gobain Sapphire Transparent Armor Composites, In: *Advances in ceramic armor III: Ceram. Eng. and Sci. Proc.*, 28[5], 113–24 (2008).
- [142] A. M. Dolan, "Ballistic transparent armor testing using a multi-hit rifle pattern", *Kettering University Thesis*; (2007).
- [143] C. Westmark and G. Wm. Lawless, "A discussion of rain erosion testing at the United States Air Force rain erosion facility", *Wear*, 186-187, 384-87 (1995).
- [144] C.R. Seward, C.S.J. Pickles and J. E. Field, "Single- and multiple-impact jet apparatus and results", *Proc. SPIE*, Vol. 1326, pp 280-290 (1990).
- [145] S. M. Walley and J. E. Field, "The contribution of the Cavendish Laboratory to the understanding of solid particle erosion mechanisms", *Wear*, 258, 552-66 (2005).
- [146] E. McKinley, "A—Rock Strike Testing of Transparent Armor", *US Army Solicitation # W56HZV09RA006* (2009).
- [147] D. N. Hansen and A. Wagner, "Rock Strike Testing of Transparent Armor", *US Army TARDEC Report # 21029* (2010).
- [148] S. Kobayashi, S. Masui and S. Miura, "Fracture and deformation on (0001) and (1010) in sapphire single crystals with Vickers indenter", *J. Soc. Mat. Sci. Japan*, 51[7], 780-87 (2002).
- [149] W. D. Reinhart, L. C. Chhabildas and T. J. Vogler, "Investigating phase transitions and strength in single-crystal sapphire using shock-res shock loading techniques", *J. Imp. Eng.*, 33, 655-69 (2006).
- [150] M. Monoharan and G. Muralidharan, "The Dependence of Indentation Cracking in Silicon on Indentation Spacing and Relative Orientation", *Mater. Res. Soc. Sym. Proc.*, (1998).

- [151] S. R. Choi and J. A. Salem, "Interaction of cracks between two adjacent indents in glass", *J. Mater. Sci.*, 28[2], (1993).
- [152] P. C. Twigg, R. W. Davisge, F. L. Riley, A. Franco and S. G. Roberts, "Indentation-induced crack interaction in alumina ceramics", *Phil. Mag. A*, 74[5], (1996).
- [153] W. Zhang and G. Subhash, "Damage zone interaction due to non-oriented Vickers indentations on brittle materials", *J. Mater. Sci.*, 38, 1185-1194 (2003).
- [154] W. Zhang and G. Subhash, "Finite element analysis of interacting Vickers indentations on brittle materials", *Acta Mater.*, 49[15], 2961-2974 (2001).
- [155] B. R. Lawn, A. G. Evans and D. B. Marshall, "Elastic/Plastic Indentation Damage in Ceramics: The Median/Radial Crack System", *J. Am. Ceram. Soc.*, 63[9-10], 574-81 (1980).
- [156] B. R. Lawn and R. Wilshaw, "Indentation fracture: principle and applications", *J. Mater. Sci.*, 10[6], 1049-81 (1975).
- [157] M. Y. Khan, L. M. Brown and M. M. Chaudhri, "The effect of crystal orientation on the indentation cracking and hardness of MgO single crystals", *J. Phys. D Appl. Phys.*, 25[1a] pp. A257-A265 (1992).
- [158] Military Standard MIL-STD-662F; "V50 Ballistic Test for Armor", U.S. Army Research Laboratory: Aberdeen Proving Ground, MD, (1997).
- [159] B. James, Depth of penetration testing. In: *Ceramic Armor Materials by Design, Ceramic Transactions*, Vol.134, p. 165-72, Edited by: J. W. McCauley, A. Crowson, W. A. Gooch Jr., A. M. Rajendran, S. J. Bless, K. V. Logan, M. Normandia and S. Wax, (2002).
- [160] M. J. Normandia and W. A. Gooch, "An overview of ballistic testing methods of ceramic materials", In: *Ceramic Armor Materials by Design, Ceramic Transactions*, Vol.134, Edited by: McCauley JW, Crowson A, Gooch Jr. WA, Rajendran AM, Bless SJ, Logan KV, Normandia M, Wax S, p.113-38 (2002).
- [161] D.A. Shockey, A.H. Skaggs, G.E. Cort, M.W. Burkett and R. Parker, "Failure Phenomenology of Confined Ceramic Targets and Impacting Rods", *Int. J. Impact Engng.*, 9[3] (1990).
- [162] P. Riou, L. Beylat, C. Cottenot and J. L. Derep, "Impact Damage on Silicon Carbide: First Results," *Journal de Physique IV*, Colloque C8, 4, 281-87, (1994).
- [163] H. Schardin, "Physikalische Vorgänge bei hohen Belastungen und Belastungsgeschwindigkeiten" ("Physical Processes at High Loadings and Loading Rates"), *Scripts of the German Academy for Aeronautical Research*, 40, 21-58 (1939).

- [164] S. Winkler, H. Senf and H. Rothenhäusler, "Wave and Fracture Phenomena in Impacted Ceramics", Fraunhofer-Institut für Kurzzeitdynamik, Ernst-Mach-Institut, Weil am Rhein, *EMI Report V 5/89, Final Report Contract DAJA 45-88-C-001 1* (1989).
- [165] H. Senf, E. Straßburger and H. Rothenhäusler, "Stress Wave Induced Damage and Fracture in Impacted Glasses", *Journal Phys. IV, C8, 4*, 741–746 (1994).
- [166] H. Senf, E. Straßburger and H. Rothenhäusler, "Visualization of Fracture Nucleation During Impact in Glass", In: *Metallurgical and Materials Applications of Shock-Wave and High-Strain-Rate Phenomena*, pp. 163–170 (1995).
- [167] H. Senf, E. Straßburger and H. Rothenhäusler, "A Study of Damage During Impact in Zerodur", *J. Phys. IV, 7[3]*, 1015–20 (1997).
- [168] H. Senf and S. Winkler, "Experimental Investigation of Wave and Fracture Phenomena in Impacted Ceramics: Sapphire," *U.S. Army Research Laboratory contractor report # ARL-CR-310*, (1997).
- [169] E. Straßburger, H. Senf and H. Rosenhausler, "Fracture propagation during impact in three types of ceramics", *J. Phys IV, C8*, 653–58 (1994).
- [170] E. Straßburger and H. Senf, "Experimental Investigations of Wave and Fracture Phenomena in Impacted Ceramics and Glasses"; *ARL-CR-214; re-publication of EMI-Report 3/94*; U.S. Army Research Laboratory: Aberdeen Proving Ground, MD, (1995).
- [171] E. Straßburger, H. Senf and H. Rothenhäusler, "Comparison of Failure Behavior During Impact and Ballistic Performance of Different Al₂O₃-Ceramics," *Proc. Lightweight Armour Systems Symposium*, Shrivenham, UK, (1995).
- [172] E. Straßburger, B. Lexow and H. Senf, "Investigation of Fracture Propagation During Impact in Advanced Ceramics," *Final Report, EMI-Report E 6/98*, Weil am Rhein, (1998).
- [173] E. Straßburger and B. Lexow, "Investigation of Fracture Propagation during Impact in Boron Carbide," *Final Report, EMI-Report E 6/02*, Efringen-Kirchen, (2002).
- [174] E. Straßburger, P. Patel, J. W. McCauley and D. W. Templeton, "High-Speed Photographic Study of Wave and Fracture Propagation in Fused Silica", *Proceeding of the 22nd Int. Symposium on Ballistics*, Vancouver, BC, Canada, (2005).
- [175] E. Straßburger, "Visualization of Impact Damage in Ceramics Using the Edge-On Impact Technique", *Int. J. Appl. Ceram. Tech.*, 1 [3], 235-42 (2004).

- [176] E. Straßburger, P. Patel, J. W. McCauley, C. Kovalchick, K. T. Ramesh and D. W. Templeton, "High-speed transmission shadowgraphic and dynamic photoelasticity study of stress wave and impact damage propagation in transparent materials and laminates using the edge-on impact method". In: *Proceedings of the twenty-third international symposium on ballistics*, Spain (2007).
- [177] E. Straßburger, P. Patel, J. W. McCauley and D. W. Templeton, "Visualization of Wave Propagation and Impact Damage in a Polycrystalline Transparent Ceramic – AION", *Proceedings 22nd Int. Symposium on Ballistics*, Vancouver, BC, Canada, (2005).
- [178] E. Straßburger, P. Patel, J. W. McCauley and D. W. Templeton, "High Speed Photographic Study of Wave Propagation and Impact Damage in Fused Silica and ALON using the Edge on Impact (EOI) Method", in *Shock Compression of Condensed Matter*, pp. 892-95 (2006).
- [179] E. Straßburger, "High-Speed Photographic Study of Wave Propagation and Impact Damage in Transparent Aluminum Oxynitride (AION)"; *first interim report, contract no. N62558-04-P-6031, EMI Report E 29/04*, (2004).
- [180] E. Straßburger, "High-Speed Photographic Study of Wave Propagation and Impact Damage in Transparent Aluminum Oxynitride (AION)"; *second interim report, contract no. N62558-04-P-6031, EMI Report E 11/05*, (2005).
- [181] E. Straßburger, "High-Speed Photographic Study of Wave Propagation and Impact Damage in Transparent Aluminum Oxynitride (AION)"; *Final Report, Contract No. N62558-04-P-6031, EMI-Report E 08/06, re-published as ARL-CR-579*; U.S. Army Research Laboratory: Aberdeen Proving Ground, MD, (2006).
- [182] M. I. Mendelson, "Average Grain Size in Polycrystalline Ceramics", *J. Am. Ceram. Soc.*, 52[8], 443-46, (1969).
- [183] Y. Takayama, N. Furushiro, T. Tozawa, H. Kato and S. Hori, "A Significant Method for Estimation of the Grain Size of Polycrystalline Materials", *Mat. Trans.*, 32[3], 214-21, (1991).
- [184] N. K. Bourne, J. C. F. Millett, M. Chen, J. W. McCauley and D. P. Dandekar, "On the Hugoniot elastic limit in polycrystalline alumina", *J. Appl. Phys.*, 102, (2007).
- [185] G. F. Miller and H. Pursey, "On the partition of energy between elastic waves in a semi-infinite solid", *Proc. Roy. Soc. London A*, 233, 55-69 (1955).
- [186] D. E. Grady, "The Spall Strength of Condensed Matter", *J. Mech. Phys. Sol.*, 36[3], 353-84, (1988).
- [187] J. Reed, "Energy losses due to elastic wave propagation during elastic impact", *J. Phys. D: Appl. Phys.*, 18, 2329-37, (1985).

- [188] S. C. Hunter, "Energy Absorbed by Elastic Waves During Impact", *J. Mech. Phys. Sol.*, 5, 162-71, (1957).
- [189] D. Curran, L. Seaman, T. Cooper, and D. Shockey, "Micromechanical Model for Comminution and Granular Flow of Brittle Material under High Strain Rate Application to Penetration of Ceramic Targets", *Int. J. Impact Engng.*, 13[1], 53-83 (1993).
- [190] R. Renström, "Impact of Metallic Projectiles on a Ceramic Target Surface: Transition between Interface Defeat and Penetration", *Int. J. Imp. Eng.*, 24[3]. 259-75 (2000).
- [191] J. C. LaSalvia, E. J. Horwath, E. J. Rapacki, C. J. Shih, and M. A. Meyers, "Microstructural and Micromechanical Aspects of Ceramic/Long-Rod Projectiles Interactions: Dwell/Penetration Transitions"; pp. 437–46 in *Fundamental Issues and Applications of Shock-Wave and High-Strain-Rate Phenomena*, Edited by K. P. Staudhammer, L. E. Murr, and M. A. Meyers. Elsevier Science, New York, 2001.
- [192] K. L. Johnson, *Contact Mechanics*, Cambridge University Press, London, 1985.
- [193] K. A. Iyer, "Relationships Between Multiaxial Stress States and Internal Fracture Patterns in Sphere-Impacted Silicon Carbide," *Int. J. Frac.*, 146 [1–2], 1–18 (2007).
- [194] F. C. Frank and B. R. Lawn, "On the Theory of Hertzian Fracture," *Proc. R. Soc. London*, A299 [1458] 291–306 (1967).
- [195] B. R. Lawn, "Indentation of Ceramics With Spheres: A Century After Hertz," *J. Am. Ceram. Soc.*, 81 [8] 1977–94 (1998).
- [196] D. R. Miller, "Friction and abrasion of hard solids at high sliding speeds", *Proc. Roy. Soc. London A*, 269[1338], 368-84 (1962).
- [197] J. C. LaSalvia, J. Campbell, J. J. Swab, J. W. McCauley, "Beyond hardness: ceramics and ceramic-based composites for protection", *JOM*, 62, 16–23 (2010).

BIOGRAPHICAL SKETCH

Edward Haney was born in Alma, MI, a small city an hour north of the state capital Lansing. He completed his high school education in 1994 at Shepherd High School in nearby Shepherd, MI. After graduation he attended Central Michigan University in Mount Pleasant, MI for 3 years until transferring to Michigan Technological University in Houghton, MI, in 1997. While at Michigan Technological University, he was a member of the Varsity Track and Cross-Country teams. In 1999, he earned his B. S. in mechanical engineering from Michigan Tech. He then moved to the Detroit metro area accepting a position in the Chrysler Institute of Engineering (CIE) program with DaimlerChrysler (Now Chrysler Automotive Group LLC). In 2002 he earned an M.S. in mechanical engineering from Oakland University, Rochester, MI. In that same year he graduated from the CIE program and accepted a full time engineering position in product development and design at Chrysler.

In 2007 he started work towards his PhD at the University of Florida while living and working in Michigan. In 2009 he resigned at Chrysler and accepted a position with Trijicon Inc., Wixom, MI, as a research and development engineer. From 2009 to 2011 time was shared between Florida and Michigan conducting research at UFL and working at Trijicon. In 2011 Mr. Haney completed his PhD dissertation. He now resides in Fenton, MI with his wife, Jill, and children, Caleb and Marissa.